

**DOWN-CONVERTING POLYMER COMPOSITES
AND THEIR WHITE LIGHT APPLICATIONS**

**A Thesis Submitted to
the Graduate School of Engineering and Sciences of
İzmir Institute of Technology
in Partial Fulfillment of the Requirements for the Degree of**

DOCTOR OF PHILOSOPHY

in Materials Science and Engineering

**by
Tuğrul GÜNER**

**December 2018
İZMİR**

We approve the thesis of **Tuğrul GÜNER**

Examining Committee Members:



Prof. Dr. Mustafa M. DEMİR

Department of Materials Science and Engineering, İzmir Institute of Technology



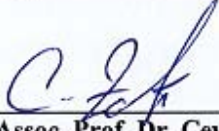
Prof. Dr. Canan VARLIKLI

Department of Photonics, İzmir Institute of Technology



Assist. Prof. Dr. Umut ADEM

Department of Materials Science and Engineering, İzmir Institute of Technology



Assoc. Prof. Dr. Ceylan ZAFER

Solar Energy Institute, Ege University



Assist. Prof. Dr. Nesrin HORZUM POLAT

Department of Engineering Sciences, İzmir Katip Çelebi University



Prof. Dr. Mustafa M. DEMİR

Supervisor, Department of Materials Science and Engineering
İzmir Institute of Technology

03 December 2018



Prof. Dr. Mustafa M. DEMİR

Head of the Department of Materials
Science and Engineering

Prof. Dr. Aysun SOFUOĞLU

Dean of the Graduate School of
Engineering and Sciences

ACKNOWLEDGEMENTS

I would like to express my deepest gratitude to my advisor, Prof. Mustafa M. Demir, for his excellent guidance, caring, patience, confidence, friendship and providing me with an excellent atmosphere for doing this research.

I thank to Gokhan Topcu for his support and collaboration where we have established a deep friendship while we were working for numerous subjects during my PhD. I want to also thank to the members of Demir Research Group including Anil Incel, Tugba Isik, Anilcan Kus, Hurriyet Yuce, Ezgi Inci, Tugce Arica Guvenc, Yenal Yalcinkaya, Emre Karaburun for their friendship, support and patience for my terrible jokes. A special thanks to faculty members of Materials Science and Engineering.

Last but not the least; I would like to thank my lovely wife for her support all during my PhD and my life. Without her, nothing that I have done all during this time would be pleasant as much as I have gained with her. I also thank to my parents and my sister for supporting me spiritually throughout my life in general. This thesis is dedicated to both my wife and them who have given me their unconditional support, both financially and emotionally throughout my PhD.

ABSTRACT

DOWN-CONVERTING POLYMER COMPOSITES AND THEIR WHITE LIGHT APPLICATIONS

Down-converting materials, which are luminescent materials that can emit at lower energies than their excitation energies, have been employed in a broad range of application area including phosphor-converted white LEDs, display technologies, solar cells, etc. In general, they can be obtained in the form powder or in dispersion. Therefore, to use them in an application, various methods such as spin coating can be applied or they can be prepared in the form of ceramic plate or polymer composite. In this thesis, we fabricate polymeric composite of some of these down-converting materials to use them in white light applications. In this sense, we have prepared these down-converting materials together with suitable polymers to form polymer/down-converting material composite in order to obtain free-standing film. Among those, polydimethylsiloxane was used in most of our applications especially the ones that involve *inorganic* down-converting materials. Second, polystyrene was employed to produce electrospun fibers in the case of when *organic* down-converting materials were used. After obtaining these composites in the form of free-standing film, we have focused specifically their use as color conversion layers over blue or UV LED chip to produce white light. The last part of the thesis describes our future prospects. We think that halide perovskites, which have high quantum yield, low cost, ease of synthesis, and wavelength tunability, can be promising materials in order to be employed as color conversion layer in white light applications. The details of these material systems, and their recent use in phosphor-converted white LED applications were summarized.

ÖZET

AŞAĞI-ÇEVİRİCİ POLİMER KOMPOZİTLER VE BUNLARIN BEYAZ IŞIK UYGULAMALARI

Aşağı-çevirici malzemeler, uyarıldıkları enerjiden daha düşük enerjilerde ışımaya yapan ışıldayan malzemelerdir, fosfor-dönüşümlü beyaz LED, ekran teknolojileri, güneş hücreleri gibi geniş bir alanda kullanılmaktadırlar. Bunlar genel olarak toz veya ıslak olarak elde edilirler. Bu sebeple, bir uygulamada kullanmak için döndürmeli kaplama gibi yöntemler uygulanmalı veya seramik plaka ve polimer kompozit şeklinde hazırlanmalıdırlar. Bu tezde, beyaz ışık uygulamaları için kullanmak üzere bazı aşağı-çevirici malzemelerin polimer kompozitlerini ürettik. Bu manada, kendi başına ayakta durabilen film elde etmek amacıyla bu aşağı-çevirici malzemeler uygun polimerler ile birlikte polimer/aşağı-çevirici malzeme kompozit olarak hazırladık. Bunlar içerisinde, ilk olarak, çoğu uygulamamızda özellikle *inorganik* aşağı-çevirici malzeme içerenlerde polydimethylsiloxane kullandık. İkinci olarak, organik aşağı-çevirici malzemelerin kullanıldığı durumlarda elektrospun lifleri üretmek için polistiren kullanılmıştır. Bu kendi başına ayakta duran kompozitleri elde ettikten sonra beyaz ışık üretmek için spesifik olarak bunların mavi ya da UV LED üzerinde renk dönüşüm katmanları olarak kullanımına odaklandık. Tezin son kısmı gelecek çalışma olasılıklarını betimlemektedir. Yüksek kuantum verimliliklerinden, düşük maliyetlerinden, kolay sentezlenmelerinden ve dalgaboyu ayarlanabilirliklerinden ötürü halojenür perovskite'ların beyaz ışık uygulamalarında renk dönüşüm katmanı olarak kullanılmalarının umut vaat ettiğini düşünüyoruz. Bu malzeme sistemlerinin detayları ve bunların son dönemlerde fosfor-dönüşümlü beyaz LED uygulamalarındaki kullanımları özetlendi.

Dedicated to my wife...

TABLE OF CONTENTS

LIST OF FIGURES	vii
LIST OF TABLES	xii
LIST OF ABBREVIATIONS.....	xiii
CHAPTER 1. INTRODUCTION	1
1.1.Motivation.....	1
1.2.Structure and Scope of the Thesis.....	3
1.3.Optical Setup.....	3
1.4.Methods	4
CHAPTER 2. LITERATURE REVIEW	6
CHAPTER 3. WLED USING INORGANIC PIGMENTS: MULTILAYER, OPTICAL ENHANCEMENT, GREEN SYNTHESIS.....	10
3.1. Multilayer design of hybrid phosphor film for application in LEDs	10
3.1.1. Materials and Methods.....	11
3.1.2. Preparing the Phosphor Composite Film	11
3.1.3. Results and Discussion	12
3.1.3.1. YAG:Ce ³⁺ and Red Phosphor Particles.....	12
3.1.3.2. Structural Development of the Composite Coatings	13
3.1.3.3. The Optical Performance of Composite Coatings	18
3.1.3.4. Simulation	22
3.1.4. Conclusion	25
3.2. Optical Enhancement of Phosphor-Converted WLEDs Using Glass Beads.....	25
3.2.1. Materials and Methods.....	26
3.2.2. Preparing the PDMS / (Phosphor - Glass Bead) Composite Films .	26
3.2.3. Optical Measurement.....	26
3.2.4. Results and Discussion	27

3.2.4.1. YAG:Ce ³⁺ and Glass Beads	27
3.2.4.2. The Effect of Glass Beads on the Optical Performance of Phosphor Layer	28
3.2.5. Conclusion	33
3.3. Green Fabrication of Y(OH) ₃ :Eu ³⁺ Red Phosphors for White Light Generation.....	33
3.3.1. Materials and Methods.....	34
3.3.2. Synthesis of Eu-doped Yttrium Hydroxide Crystals	34
3.3.3. Results and Discussion	35
3.3.3.1. Growth Mechanism of Y(OH) ₃ :Eu ³⁺ Crystals	40
3.3.3.2. White Light Application of Y(OH) ₃ :Eu ³⁺	43
3.3.4. Conclusion	45
CHAPTER 4. WLED USING ORGANIC ONE: FIBERS CONTAINNING PERYLENE DYES	46
4.1. Perylene-Embedded Electrospun PS Fibers For White Light Generation.....	46
4.1.1. Materials and Methods.....	47
4.1.2. Preparation of Organic Dye-Embedded PS Fibers	48
4.1.3. Preparation of PDMS/Organic Dye Embedded PS Fiber Composites	48
4.1.4. WLED Studies	49
4.1.5. Results and Discussion	50
4.1.6. Conclusion	57
CHAPTER 5. Future Prospects	58
5.1. Halide Perovskite-based Applications	58
5.2. Preparation of Halide Perovskite Materials	60
5.2.1. Organometallic Halide Perovskites	60
5.2.2. All-Inorganic Halide Perovskites.....	61
5.3. Optical Characteristics of Halide Perovskite Materials	62
5.4. Use of Halide Perovskites In WLED Applications	65
5.4.1. Blue LED + YAG:Ce ³⁺ + Halide Perovskite	65
5.4.2. Blue LED + Halide Perovskite	68

5.4.3. UV LED + Halide Perovskite	71
5.5. Summary	72
CHAPTER 6. CONCLUSION	73
REFERENCES	76
APPENDICES	
APPENDIX A. PYTHON CODES OF THE SIMULATION.....	96

LIST OF FIGURES

<u>Figure</u>	<u>Page</u>
Figure 1.1. Photographic representation of the remote phosphor configuration and optical measurement of the samples via integrating sphere.....	4
Figure 2.1. Emission and excitation spectra of different phosphors with varying host lattice and activation ion. (modified from (Source: George, Denault, and Seshadri 2013))	6
Figure 2.2. Energy level diagram representing the effect of centroid and crystal field splitting due to the host crystal on Ce ion. (adopted from (Source: George, Denault, and Seshadri 2013)).....	7
Figure 3.1. Schematic illustration of the spray coating process. Part a) shows the spray of PDMS / Phosphor solution towards PC substrates that are placed carefully on a plate. Part b), and part c) are the demonstration of coating strategies followed during spraying representing the stacking, and mixture as single layer respectively.	12
Figure 3.2. SEM images of a) YAG:Ce ³⁺ , and b) red phosphor powders. Size distribution of these related phosphors, c) YAG:Ce ³⁺ , and d) red phosphor are also calculated. Panel e is the XRD pattern of phosphor powders, and f) is PL spectrum of the phosphor powders. Excitation spectrum was recorded with emission wavelength at 550nm, and emission spectrum was recorded with the excitation wavelength at 478 nm which is same as the blue LED for YAG:Ce ³⁺ (black line). For the red phosphor (red line), excitation spectrum was recorded at emission wavelength at 610 nm. Emission spectrum details are same with the YAG:Ce ³⁺	14
Figure 3.3. FTIR spectrum of cross-linking process. Panel a) presents the change of FTIR signals with respect to time was shown for neat PDMS. In panel b, and c, effect of the different phosphor contents on the FTIR signals during cross-linking were analyzed by focusing on first and second derivatives of the Si – H signal at the 2163 cm ⁻¹ respectively.	16

Figure 3.4. Optical microscope image of a) mixture as single layer sample b) is the optical microscope image of the stacking, c) is the SEM image of stacking sample but focused on the cross section under 2500x magnification. Red and yellow arrows show the red phosphor and YAG:Ce ³⁺ particle(s), respectively d) Surface charge of the phosphor particles in PDMS/hexane solution by zeta potential mode of dynamic light scattering.....	18
Figure 3.5. Spectrum of PDMS / phosphor coated PC substrates. a) remote phosphor measurement was done at 3 cm away from the blue LED source. b) direct phosphor measurement was done without having any distance between sample and blue LED source. Irradiance of samples under blue LED illumination having 0.35A input current collected by using the remote (c), and direct measurement (d).	19
Figure 3.6. a) Comparison of illumination of the coatings prepared by the mixture and stacked layers of the phosphor particles b) cartoon demonstration of the interaction of blue light with coatings prepared with two strategies. The one prepared by consecutive spraying provides adequate quality of warm white light.	20
Figure 3.7. Remote and direct spectrum obtained by simulation of stacking and mixture arrangement of phosphor particles in the PDMS coating.....	24
Figure 3.8. SEM image of the a) Glass Bead (inset is the magnified image of glass beads), and b) YAG:Ce ³⁺ . c) - d) present the PL spectrum, and X-ray diffraction of YAG:Ce ³⁺ , respectively.	27
Figure 3.9. a) PL spectra of the coatings at fixed phosphor with GB at various contents. Phosphor Reference represents the phosphor-only coating, and b) the CIE 1931 color coordinates of these samples.....	28
Figure 3.10. a) Appearance of the samples; phosphor-only coating and phosphor + GB (at the ratio 1.5), b) Photograph of the generated white light from the phosphor-only coating, and the phosphor + GB (at the ratio 1.5) coating under blue LED illumination with the driving current 0.35 mA. c) CCT, and CRI versus GB / phosphor mass ratio. Boundary between “No valid CCT (K) & CRI” and valid region represents the amount that phosphor-only coating requires for generating useful white light.....	29

Figure 3.11. Comparison of phosphor + GB coating with a phosphor + Z-Cel in terms of their a) spectra, and b) radiant power and luminous flux. Phosphor Reference represents the phosphor-only coating.....	31
Figure 3.12. XRD pattern $Y(OH)_3:Eu^{3+}$ phosphors prepared at various reaction times; 5, 15, 30, 45, and 60 min.	35
Figure 3.13. PL spectrum of $Y(OH)_3:Eu^{3+}$ phosphors obtained at various reaction times; 5, 15, 30, 45, and 60 min.	36
Figure 3.14. SEM images of the $Y(OH)_3:Eu^{3+}$ phosphors obtained at different synthesis times; a) 5 min, b) 15 min, and c) 60 min. d-f) present the overview TEM and HAADF STEM micrographs of the particles prepared in 60 min. The sample is composed of micron-sized multipods, which seem to be controlled ensemble of ~10 nm thick nanowires.....	37
Figure 3.15. General HAADF STEM and TEM micrographs of the particles prepared in 5 min showing the presence agglomerated nanocrystals.....	38
Figure 3.16. a) XRD pattern of the $Y(OH)_3:Eu^{3+}$ phosphors with various doping ratios; 2.5%, 7.5%, 14%, and 20% by mass. b) The shift of the 2 θ reflection position of 16 $^\circ$ with respect to doping ratio including the particles prepared in 60 min and 1260 min (24 h).....	38
Figure 3.17. Annular dark field (ADF) STEM micrograph of an agglomerate of nanoparticles. STEM-EELS elemental composition maps of the area indicated with a white rectangle: Y (in red) and Eu (in green) maps along with their composite image.....	39
Figure 3.18. Schematic demonstration of the crystal growth mechanism for the development of multipod-like structure of the $Y(OH)_3:Eu^{3+}$ phosphors...	40
Figure 3.19. a) PL spectrum of the $Y(OH)_3:Eu^{3+}$ phosphors with different doping ratios, and b) variation of their corresponding emission peak intensities, labeled with A, B, C, D, and E, with respect to doping ratio	42
Figure 3.20. WLED application of different amount of red $Y(OH)_3:Eu^{3+}$ phosphors combined with YAG:Ce $^{3+}$ phosphor and their corresponding CRI, CCT, LER and Lumen values.	44
Figure 4.1. Structure and Absorption-PL of the yellow, green, and red perylene diimides.....	47

Figure 4.2. Summary of electrospinning path followed for PTE, PDI and DiPhAPDI and visualization of their freestanding PDMS films under daylight and UV illumination.	48
Figure 4.3. Visualization of the WLED samples prepared with different processing methods: either by stacking individual fibers or stacking PDI:DiPhAPDI and PTE fibers separately	49
Figure 4.4. The morphology of PS/organic dye composite fibers	50
Figure 4.5. PL spectrum of individual PDMS/organic dye electrospun fiber composites and their various formation strategies including WLED and WLED 2 (driving current=20 mA)	51
Figure 4.6. Change of optical properties, power efficiency, CRI and CCT under various driving currents	53
Figure 4.7. Change of power efficiency, CRI and CCT under continuous illumination of blue LED (driving current=20 mA).....	56
Figure 5.1. Statistical data of a) publications, and b) citations about the last 20 years.	59
Figure 5.2. Schematic representation of the hot injection method. TEM image of a typical sample is given at inset. Reproduced with permission. Copyright 2017, Wiley-VCH.(Source: Li et al. 2017) b) Schematic representation of room-temperature recrystallization. Reproduced with permission. Copyright 2016, Wiley-VCH.(Source: Li, Wu, et al. 2016).....	62
Figure 5.3. a) Halide perovskites with various anions (or anion ratio) under UV illumination, b-c) collected PL and abs/PL spectra of related samples, respectively. Reproduced with permission. Copyright 2015, American Chemical Society.(Source: Protesescu et al. 2015b) d) demonstrates the size effect of perovskite NCs on the wavelength tunability. Reproduced with permission. Copyright 2015, Wiley-VCH. (Source: Song, Li, et al. 2015)	63
Figure 5.4. Different halide perovskite stabilization methods; a) mixing with mesoporous silica (Source: Wang et al. 2016), and b) growing shell of wider band-gap over halide perovskite NCs. (Source: Bhaumik et al. 2016)	64
Figure 5.5. WLED applications of red halide perovskites integrated into the blue LED excited YAG:Ce ³⁺ phosphor, which are a) directly coated on	

blue LED(Source: Zhou et al. 2017) or b) prepared in the form of PiG, (Source: Zhou, Huang, et al. 2016) systems.	66
Figure 5.6. a) Spectrum of the mixture of blue, green, and red halide perovskites. b-c) present the appearance of blue, green, and red halide perovskites under UV illumination, and their related spectrum after stacking them onto the blue LED, respectively. Reprinted (adapted) with permission from (Source: Pathak et al. 2015). Copyright (2015) American Chemical Society. d) WLED fabricated via stacking the green emitting halide perovskite with a red phosphor over blue LED. (Source: Wang et al. 2017)	68
Figure 5.7. a) Schematic representation of WLED prepared using halide perovskites over UV LED chip, and b) resulting white light generation. Reprinted (adapted) with permission from (Source: Zhang et al. 2017). Copyright (2017) American Chemical Society.....	71

LIST OF TABLES

<u>Table</u>	<u>Page</u>
Table 3.1. Color chromaticity CRI, CCT, and luminous efficacy of the coatings to both remote and direct phosphor configurations.	21
Table 3.2. Peak intensity, peak intensity wavelength and FWHM values of both remote and direct case used in the simulation.	24
Table 4.1. Fiber masses and optical properties of the related samples used in WLED strategy under 20mA of driving current	52
Table 4.2. Fiber masses and optical properties of the related samples used in WLED2 strategy under 20mA of driving current	54

LIST OF ABBREVIATIONS

CCT	Correlated Color Temperature
CFL	Compact Fluorescent Lamps
CIE	Commission Internationale de l'Eclairage
CRI	Color Rendering Index
DMF	N,N-dimethylformamide
EDX	Energy Dispersive X-Ray
FTIR	Fourier Transform Infrared
FWHM	Full Width Half Maxima
LED	Light-emitting Diode
LER	Luminous Efficiency
NP	Nanoparticle
OA	Oleic Acid
OLA	Oleylamine
PC	Polycarbonate
PDMS	Polydimethylsiloxane
pc-WLED	Phosphor-converted White Light Emitting Diode
PL	Photoluminescence
PS	Polystyrene
RGB	Red-Green-Blue
SEM	Scanning Electron Microscope/Microscopy
TEM	Transmission Electron Microscopy
TGA	Thermogravimetric Analysis
UV	Ultraviolet
WLED	White Light Emitting Diode
YAG	Yttrium Aluminum Garnet
XRD	X-ray Diffraction

CHAPTER 1

INTRODUCTION

1.1. Motivation

Lighting is an integral part of human daily lives. Beginning from the discovery of fire, tools have been developed using fire to produce lighting such as candles, lanterns, etc. In general, these tools are simulating sunlight to increase the visibility, and gaining visibility is a significant requirement for humans to feel comfortable, safe, and even it is necessary to keep up their daily routines. The first footprints of the lighting revolution begin with the invention electric dynamo by Faraday in 1831, which makes electricity a viable to use in technology. Then, Thomas Edison invented the incandescent bulb that uses electricity to produce light. Until today, apart from incandescent bulbs, various lighting bulbs based on electricity have been produced such as compact fluorescent lamps (CFL), halogen lamps, and light-emitting diodes (LEDs).

Human population grows exponentially in time. Meanwhile, basic needs and basic expenses of humans increasing in parallel to the population. Among those, energy becomes one of the critical parameters that can face with insufficiency in this period due to limited reservoirs. One of the main reasons of this rapid growth of energy requirement is the increasing demand on the electricity consumption. For instance, lighting is responsible for almost or even more than 20% of the global electricity consumption (Waide and Tanishima 2006). This challenge of increasing electricity consumption due to rapidly growing human population can be solved by making additional investments in building more power plants, developing new and more efficient methods for energy conversion such as converting sunlight into electricity by photovoltaic modules, or introducing new strategies or materials to reduce electricity consumption of existing products.

Electricity consumption has always been in correlation with the lighting starting from the invention of incandescent bulbs. From residential to outdoors, airports to factories, shopping malls to cars, demand and requirement for lighting products grow in parallel to both human population and advancing technology. Significant improvements in terms of

reducing electricity consumption and efficiency have been done already on these products since then. For instance, incandescent bulbs can consume 60W while CFL, which is the next technology that uses gases after the filament-based ones, can consume only 14W. Even more, a breakthrough in this area comes after the invention of LEDs, which is an outcome of solid-state lighting (Schubert et al. 2006, Shur and Zukauskas 2005, Schubert and Kim 2005). In this case, light is generated by a semiconductor through applied current. Compared to traditional filament- and gas-based products, LED based lighting show lower electricity consumption, significantly longer average lifetime, and can provide control on the light output; i.e. color properties can be adjusted through materials employed in the structure of LED. In order to understand the benefit of LED in terms of its energy efficiency, one can look at the 2016 Solid State Lighting Forecast Report of U.S. Department of Energy (<https://www.energy.gov/eere/ssl/ssl-forecast-report>). According to this report, it was mentioned that there will be 75% energy saving by 2035 in the case of LED use for lighting compared to no use of LED case (if the Department of Energy goal about the amount of LED use is achieved).

White light generation through LEDs becomes possible after the invention of red, green, and blue (RGB) LEDs (Cho et al. 2017). These LEDs can be combined into a multi-chip configuration to produce white light since they satisfy RGB, which are the three main colors that form white light. However, due to difference between individual LED chips in terms of their response against temperature and aging, and even against driving current, this type of configuration becomes commercially not favorable due to their complex integration (Shinde and Dhoble 2014, Ye et al. 2010). Another strategy, which is employed in many commercial LED lighting products, is about using down converting materials such as phosphors (Smet, Parmentier, and Poelman 2011, Tucureanu et al. 2015, Xia et al. 2016, Ye et al. 2010, George, Denault, and Seshadri 2013, Lin and Liu 2011), quantum dots (Jang et al. 2010, Demir et al. 2011, Shirasaki et al. 2013, Wood and Bulović 2010), perovskites (Guner and Demir 2018, Li et al. 2017, He, Qiu, and Yang 2017), organic dyes, etc. together with blue or UV-LED to produce white light. Down conversion is an optical process about converting the wavelength of incoming light into a longer wavelength. For instance, in a typical white LED product, blue LED is coated directly with a yellow phosphor *Cerium doped Yttrium Aluminum Garnet* (YAG:Ce³⁺) that is dispersed in epoxy or PDMS matrix. In such a case, blue light produced from the LED partially excites the yellow phosphor and leads to yellow emission. Transmitted blue light combines with the yellow emission over the phosphor coated LED chip, and

generates white light. This type of white light generation through a configuration consisting of a LED and down-converting color conversion layer(s) is known as phosphor-converted white LED (pc-WLED). However, LED chips can be warmed up to ~200°C in time, and such a heating generally causes thermal degradation for the phosphors due to direct coating (Bachmann, Ronda, and Meijerink 2009). To overcome this issue, remote phosphor configuration (Shuai et al. 2012a, Allen and Steckl 2008, Narendran et al. 2005, Tran, You, and Shi 2009b, Acuña et al. 2014), which is about placing color conversion layer some distance apart from the LED chip, can be employed to produce white light.

In this thesis, down converting materials have been focused mainly in the perspective of pc-WLED configuration to produce more efficient white light or to improve white light properties such as *Color Rendering Index* (CRI), and *Correlated Color Temperature* (CCT). Since the LED based lighting is significantly more energy efficient than the other traditional lighting products, studies conducted during this thesis aimed to contribute in this field to make LED-based lighting more favorable, cheaper, and to provide better white light properties compared to the other products.

1.2. Structure and Scope of the Thesis

The first chapter of the thesis introduces the main idea and purpose behind studies conducted during researches. In *chapter 2*, literature is reviewed in parallel to studies have been done in this thesis. Studies that have been made during this thesis were summarized in *chapter 3*, and *chapter 4* with titles depending on the type of down-converting material that is employed: inorganic or organic. Future prospects based on employing halide perovskites as color conversion layers for white light generation as promising materials summarized in *chapter 5* and concluding remarks are given in *chapter 6*.

1.3. Optical Setup

Throughout this thesis, remote-phosphor configuration was used to measure optical features of the generated white light to avoid thermal quenching of polymer/down-

converting material composites due to heating up of LED chip. Optical set-up including remote phosphor configuration and optical measurement was demonstrated in **Figure 1.1**.

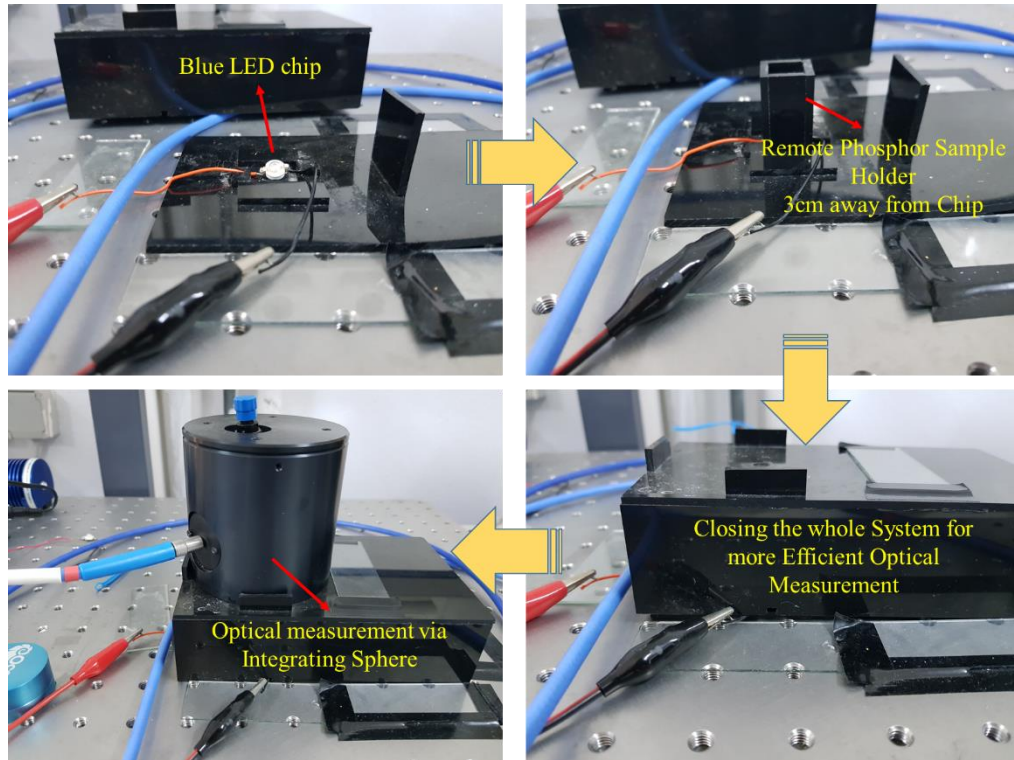


Figure 1.1. Photographic representation of the remote phosphor configuration and optical measurement of the samples via integrating sphere

In this set up, first a single LED chip is located at the bottom of the black box, which was connected to DC power supply via cables. Next, remote phosphor sample holder having 3 cm length between LED chip and its top was placed over LED chip. Any sample was put at the top of it in order to be excited by LED chip. To conduct optical measurements over the sample, the system is closed with the remaining part of the black box having hole just matching with the position of LED chip as demonstrated in third picture of **Figure 1.1**. At last, integrating sphere is put over the hole of black box to measure PL of the sample.

1.4. Methods

The diffraction pattern of the phosphor powders were recorded with an X-ray diffractometer (X'Pert Pro, Philips, Eindhoven, the Netherlands), and the

photoluminescence (PL) spectrum was recorded on a fluorescence spectrophotometer (Cary Eclipse, Agilent, Palo Alto, CA, USA). Fourier transform infrared spectroscopy (FTIR; Spectrum 100, PerkinElmer, Shelton, CT, USA) was used to characterize and track changes in the kinetic behavior of bonds, and scanning electron microscopy (SEM; Quanta 250, FEI, Hillsboro, OR, USA) was used to determine particle, fiber, and composite morphologies. The dispersion of powders in PDMS was observed with an optical microscope (BX 53, Olympus, Tokyo, Japan). Spectra of the resulting emissions were recorded by spectrometer (USB2000+, Ocean Optics Inc., Dunedin, FL, USA). Color coordinates and flux were obtained by an integrating sphere (ISP-50-80-R, Ocean Optics Inc.) connected with the USB2000+ spectrometer via premium fiber cable. Throughout this thesis, blue LED chip of CREE (455 nm, Royal Blue, 1W) was used. Specification and data sheet of the employed LED can be found in (<https://www.cree.com/led-components/media/documents/XLampXTE.pdf>).

CHAPTER 2

LITERATURE REVIEW

Phosphors are traditional down-conversion materials employed heavily in commercial WLED products and display technologies. They consist of a host lattice such as orthosilicates (Ba_2SiO_4 , Sr_3SiO_5 , etc.), garnets ($\text{Y}_3\text{Al}_5\text{O}_{12}$, $\text{Ca}_3\text{Sc}_2\text{Si}_3\text{O}_{12}$, etc.), nitrides ($\text{Sr}_2\text{Si}_5\text{N}_8$, $\text{Ca}_2\text{Si}_5\text{N}_8$, etc.), oxynitrides ($\text{BaSi}_2\text{O}_2\text{N}_2$, $\text{SrSi}_2\text{O}_2\text{N}_2$, etc.), and oxyfluorides ($\text{Sr}_3\text{AlO}_4\text{F}$, $\text{Sr}_2\text{BaAlO}_4\text{F}$, etc.), and activator ions known as dopants such as Ce^{3+} , Eu^{3+} , Dy^{3+} , etc. Details of these phosphors including both the hosts and activator ions can be followed via the reviews. (Xia et al. 2016, George, Denault, and Seshadri 2013) In such a system, electronic configuration of the dopant together with the lattice characteristics of the host determine the resulting optical properties of the phosphors. Depending on the desired application area, optical properties of the phosphors can be adjusted via employing either different host lattice or activator ion.

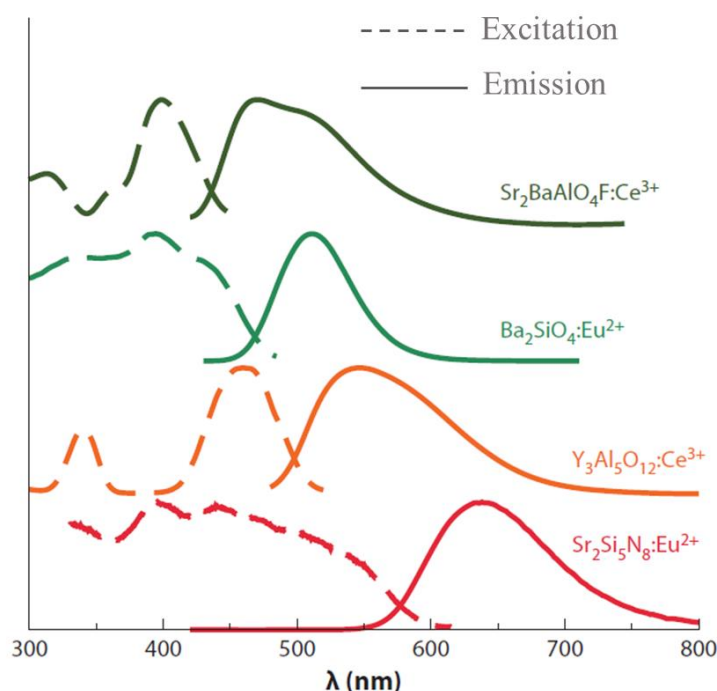


Figure 2.1. Emission and excitation spectra of different phosphors with varying host lattice and activation ion. (modified from (Source: George, Denault, and Seshadri 2013))

Figure 2.1. demonstrates the photoluminescence excitation (presented with dashed lines) and emission (solid lines) spectra of phosphors having different host lattices with varying activator ions; Ce^{3+} or Eu^{2+} . Phosphors with same activator ions show a clear shift in their excitation and emission spectra. For instance, $\text{Sr}_2\text{BaAlO}_4\text{:Ce}^{3+}$ has dark green emission around ~ 500 nm while indicating excitation at two distinct wavelengths; 400 nm and 300 nm. On the other hand, $\text{Y}_3\text{Al}_5\text{O}_{12}\text{:Ce}^{3+}$ provides almost identical excitation and emission patterns but with a significant red-shift for both: there is a yellow emission around 550 nm while excitation shows again two distinct peaks at 350 nm and 450 nm this time indicating 50nm red-shift compared to $\text{Sr}_2\text{BaAlO}_4\text{:Ce}^{3+}$. Same argument is also valid for $\text{Ba}_2\text{SiO}_4\text{:Eu}^{2+}$ and $\text{Sr}_2\text{Si}_5\text{N}_8\text{:Eu}^{2+}$, where the latter indicates a clear 100 nm red-shift in this case compared to optical properties of the former phosphor.

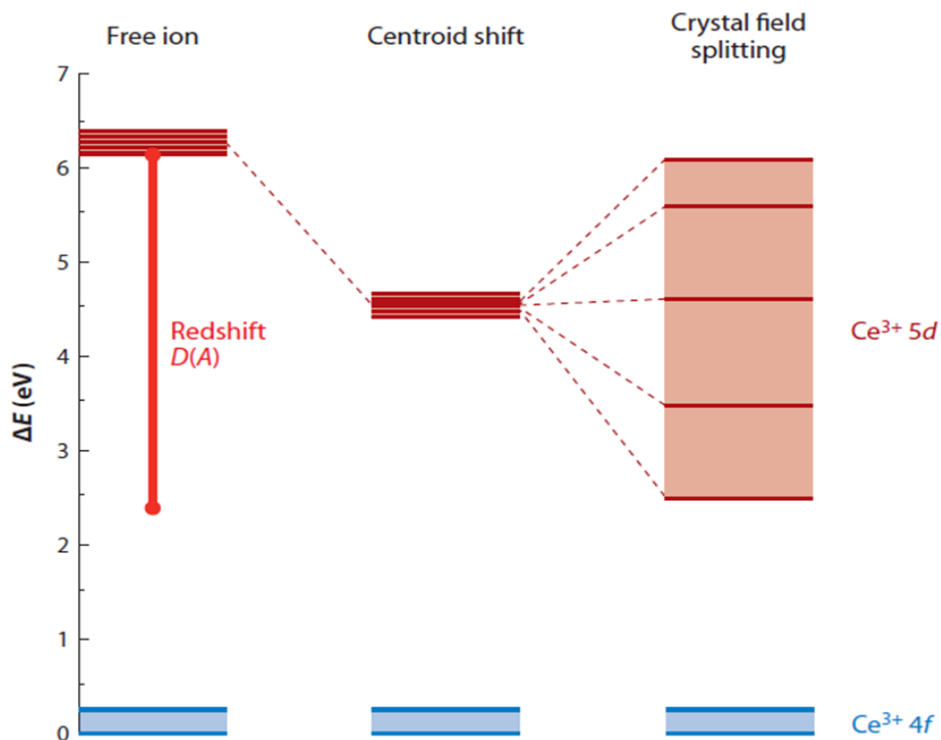


Figure 2.2. Energy level diagram representing the effect of centroid and crystal field splitting due to the host crystal on Ce ion. (adopted from (Source: George, Denault, and Seshadri 2013))

It can be concluded that the band-gap of these phosphors can be adjusted through employing different hosts while keeping dopants such as Eu^{2+} or Ce^{3+} as fixed. Therefore, based on the discussion above, having identical absorption and emission patterns in the presence of different host lattices indicate that these patterns mainly determined by the

employed dopant while the location of their peak wavelengths depend on the host lattice. Theoretically, it has been well-known for a quite long time that there are two main major effects responsible from these resulting optical characteristics of phosphors: centroid shift and crystal field splitting. These two effects are schematically presented in **Figure 2.2** considering Ce ion as an example. In general, these effects are mainly responsible from the adjustment of 5d energy levels since 4f electrons are almost remain stable against them due to their well-shielded locations. In this sense, first, the centroid shift causes 5d levels to shift towards lower energies, which is based on the decreasing inter-electron repulsion. This red-shift from 5d states of free ion due to centroid shift is illustrated **Figure 2.2**. Another effect of the host is crystal field splitting, which refers to the splitting of 5d energy levels that make difference between the highest and lowest 5d states. As a result of this splitting, lowest state of the 5d energy levels gets closer to the 4f states, as already demonstrated in **Figure 2.2**, and again causes an additional red-shift. Therefore, energy state of the Ce ion can be adjusted from UV (gaseous state) to visible range, which the range of this change directly depends on the employed host.

Polymer-based composite films containing yellow garnet particles provide flexible composite films for direct or remote applications with blue LEDs. A part of the incident light passes through the film with virtually no attenuation or backscattering, while some of the primary light is absorbed and converted by the phosphors to secondary light. The combination of incident light and secondary light passing through the film forms white light. To that end, various polymer–phosphor particle systems have been employed for down-conversion (Narendran et al. 2005, Allen and Steckl 2008, Song, Han, et al. 2015), including $\text{CeF}_3:(\text{Tb}^{3+}, \text{Dy}^{3+}, \text{Eu}^{3+})$, (Sayed et al. 2011) $\text{YVO}_4:(\text{Eu}^{3+})$, (Hreniak et al. 2011) GYAG , (Bera et al. 2010) $\text{YAG}:(\text{Ce}^{+3}, \text{Gd}^{3+})$, (Tucureanu et al. 2015) $\text{YAG}:(\text{Ce}^{+3})$, (Allen and Steckl 2008, Saladino et al. 2010, Saladino et al. 2014, Oliva et al. 2014) $\text{Zn}_2\text{SiO}_4:(\text{Mn}^{2+}, \text{Eu}^{3+})$, (Đačanin et al. 2012) $\text{BaIn}_6\text{Y}_2\text{O}_{13}:(\text{Yb}^{3+}, \text{Tm}^{3+}, \text{Er}^{3+})$ (Zhang, Yang, et al. 2015) particles dispersed in poly(methyl methacrylate), Na_2SO_4 (Zhang et al. 2013) and $\text{BaAl}_x\text{O}_y:(\text{Eu}^{2+}, \text{Dy}^{3+})$ (Bem et al. 2011) in low-density polyethylene, $\text{YAG}:\text{Ce}^{+3}$ in polydimethylsiloxane (PDMS), (Esteves, Brokken-Zijp, Laven, and de With 2010, Esteves, Brokken-Zijp, Laven, Huinink, et al. 2010) and $\text{YBO}_3:(\text{Eu}^{2+})$ (Bussière et al. 2013) and $\text{YGG}:(\text{Tb}^{3+})$ (Potdevin et al. 2012) in a polyvinylpyrrolidone matrix. In any case, the goal is a stable white light with a high color rendering index (CRI) and high luminous efficacy as well as a light color that is stable and nearly independent of the

charged current. However, that attractive optical feature is governed entirely by the quality of the material components, their preparation strategy and the internal microstructure of the composite coatings.(Demir et al. 2007, Demir et al. 2006)

On the other hand, approaches such as reducing phosphor content in pc-WLEDs(Ogi et al. 2013, Tsai et al. 2013) and finding phosphor-free conversion materials, including quantum dots(Erdem and Demir 2013) and perovskites(Protesescu et al. 2015a), have been also developed. However, attempts to produce significant materials should result in a high color rendering index (CRI), a low correlated color temperature (CCT), high efficacy, and a stable light output without fluctuations under different driving currents. Moreover, the structure of composite coatings, including its homogeneity(Sommer et al. 2010, Hu et al. 2012) and internal microstructure(Demir et al. 2007, Demir et al. 2006), determines the blue light flux in the overall spectrum(Güner, Köseoğlu, and Demir 2016), i.e., determines the optical performance of coatings in terms of CCT, CRI, efficacy, luminous flux, and radiant flux. These requirements are the main concerns in producing a commercially viable light source.

CCT is crucial for indoor and outdoor lighting (white) applications. This characteristic is the equivalence of a blackbody radiation at particular temperature with the lighting source in charge in terms of the generated light. Thus, while a low CCT (warm white) is preferred for indoor use to promote relaxation, a high CCT (cool white) is desired for outdoor use, such as in mall centers or traffic lightings, to maintain a more energetic atmosphere. In general, cool white corresponds to CCT values > 5,000 K, whereas warm light corresponds to CCT values between 2,500 and 5,000 K. Luminous efficacy (LER) is a characteristic that defines the degree of matching between a spectrum and the sensitivity of the human eye (Erdem, Nizamoglu, and Demir 2012). It is defined as

$$LER = 683 \text{ lm/W} \frac{\int v(\lambda)\phi(\lambda)d\lambda}{\int \phi(\lambda)d\lambda} \quad (1)$$

where $v(\lambda)$ is the luminosity function and $\phi(\lambda)$ is the spectral power distribution per wavelength.

CHAPTER 3

WLED USING INORGANIC PIGMENTS: MULTILAYER, OPTICAL ENHANCEMENT, GREEN SYNTHESIS

3.1 Multilayer design of hybrid phosphor film for application in LEDs

Interaction of the material components, for instance the interaction of phosphor particles with polymer precursors and other ingredients, and the spatial arrangement of the phosphor particles are the key parameters in the structural development of the coating. In this study, the interaction of YAG:Ce⁺³ with PDMS precursors or red phosphor and the arrangement of the particles either stacked layers or random mixture are examined in detail.

Cerium doped Yttrium Aluminum Garnet (YAG:Ce⁺³) was used as yellow phosphor. It has been widely used for WLED applications due to its high conversion efficiency, energy saving aspect compared to incandescent and fluorescent lighting, and low cost (Pan, Wu, and Su 2004). However, there are serious shortcomings such as thermal quenching (Bachmann, Ronda, and Meijerink 2009), low CRI, and red emission deficiency (Lin, Meijerink, and Liu 2016b). Remote phosphor set-up was used to avoid thermal quenching (Shuai et al. 2012b). Additional red phosphor (Sr₂Si₅N₈:Eu²⁺, Europium-doped strontium silicon nitride) was employed to improve the overall CRI and resulting color properties. Besides, PDMS is a transparent binder and a polymeric carrier employed in spraying. In addition, the Si–O bond is rotationally flexible; PDMS shows an unusually high degree of chain flexibility. (Demir, Menciloglu, and Erman 2005) Moreover, the energy of Si-O bond is 452 kJ/mol than common vinyl polymers having C-C bond with 347 kJ/mol. (Zumdahl and Zumdahl) Considering the exposure of the light converting film under highly energetic blue light for a long time, PDMS offers higher UV resistance compared to other alternative vinyl polymers. Spraying of the both YAG:Ce³⁺ and red phosphor particles were performed either mixture as a single layer or consecutively as two distinct stacked layers from the PDMS and hexane solution.

Throughout the text, *stacking layers* refer to multilayer building up of coating by consecutive spraying; on the other hand, *random mixture* associate with the spraying the mixture of both phosphors at once. Crosslinking process was monitored by vibrational spectroscopy both in absence and presence of the phosphor particles. The morphology of the coatings was examined by optical and scanning electron microscopy. The surface charge of the particles was studied by zeta potential of dynamic light scattering. The optical performance of the coatings prepared by these two strategies was compared in terms of CRI, CCT, and efficacy.

3.1.1 Materials and Methods

Phosphor powders YAG:Ce³⁺ with 99% quantum efficiencies and Sr₂Si₅N₈:Eu²⁺ with 45% quantum efficiencies (HB-4155H and HB-640, Zhuhai Hanbo Trading Co., Ltd., Guangdong, China) were used as received. PDMS (SYLGARD 184 Kit, Dow Corning, Midland, MI, USA) was used as a polymer matrix for film formation. Due to high viscosity of PDMS, hexane (>95%, Sigma–Aldrich, St. Louis, MO, USA) was used to thin the PDMS powder solutions.

3.1.2 Preparing the Phosphor Composite Film

Spraying is a coating technique used to make homogeneous films on a given substrate. By atomizing a solution or dispersion using high air pressure, the process is uniquely suited for dispersions consisting of heavy, large guest particles in host polymer solutions. In this study, phosphor particles with a density of approximately 4.6 g·cm⁻³ were sprayed in the form of PDMS–phosphor dispersion thinned by hexane to polycarbonate (PC) diffuser substrates (**Figure 3.1**). Following the standard process, powder was added into a test tube, and the composition of YAG:Ce³⁺ and red phosphor was fixed to 5:1 by mass ratio. PDMS precursors, i.e. a vinyl-ended PDMS oligomers and the curing agent were dropped in a 10:1 mixing ratio with respect to mass into a test tube. Next, hexane was added to reduce viscosity, the dispersion was mixed in a magnetic stirrer and poured into the hopper of a spray gun (400 W, 1–2 bar pressure), and spray

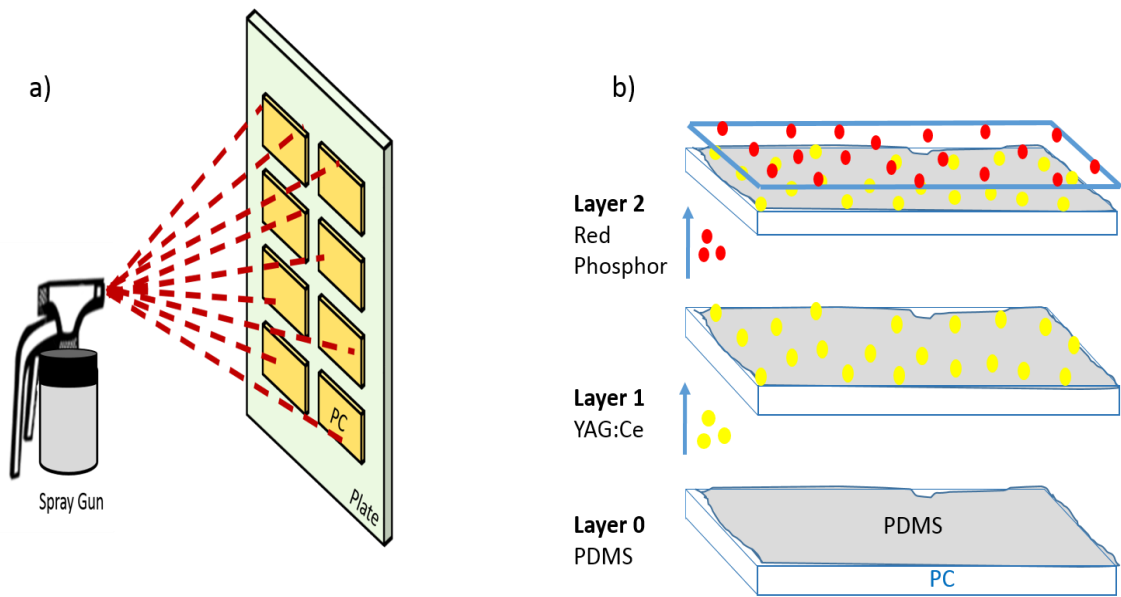


Figure 3.1. Schematic illustration of the spray coating process. Part a) shows the spray of PDMS / Phosphor solution towards PC substrates that are placed carefully on a plate. Part b), and part c) are the demonstration of coating strategies followed during spraying representing the stacking, and mixture as single layer respectively.

coating was performed onto a set of PC substrate 7–10 s. The resulting composite coatings were approximately 60 μm thick; one side of the substrate was smooth and reflective, whereas another surface—the diffuser side—was rough. Phosphor was sprayed onto the diffuser side because rough surfaces can hold the phosphor coating. The samples were left in open air overnight so that the hexane could fully evaporate, after which they were cured at 100 $^{\circ}\text{C}$ for 2 h in an oven.

3.1.3 Results and Discussion

In this part of the thesis, we will discuss the results that have been obtained from the characterizations and experiments.

3.1.3.1 YAG:Ce³⁺ and Red Phosphor Particles

Figure 3.2 shows the morphological and structural characterization of the phosphor particles. Figures 3.2(a) and (b) present SEM images of the YAG:Ce³⁺ and red

phosphor powders, respectively; YAG:Ce³⁺ had a nearly monodisperse polyhedral shape, whereas Sr₂Si₅N₈:Eu²⁺ powder had a rather polydispersed shape that changed from polyhedral to rod-like crystals. This difference was also verified by particle size distributions obtained by the statistical treatment of particles using ImageJ in **Figures 3.2 (c) and (d)**. (Schneider, Rasband, and Eliceiri 2012) Although both powders demonstrated a close mean diameter of nearly 10 μm, Sr₂Si₅N₈:Eu²⁺ had a broader distribution than YAG:Ce³⁺ that extended the tail of the distribution to 60 μm in diameter. **Figure 3.2 (e)** shows the X-ray diffraction pattern of both yellow and red phosphor powders. Reflections were indexed with the crystallographic data of host materials YAG and Sr₂Si₅N₈:Eu²⁺ with Joint Committee on Powder Diffraction Standards (card nos. 01-082-0575 and 01-085-0101, respectively). **Figure 3.2 (f)** illustrates the PL spectrum of the phosphors at room temperature. YAG:Ce³⁺ showed two absorption bands centered at 340 nm and 460 nm that matched the band-gap values collected at 550 nm. Those bands can be related to 4f → 5d absorption transitions separated due to crystal field splitting of 5d states of the Ce³⁺ ion. The broad emission band of YAG:Ce³⁺ centered at 560 nm is the result of radiative energy transfer from the lowest 5d state to the 4f states (excitation wavelength, λ_{Exc} = 478 nm). By contrast, red phosphor has a single broad excitation band at 440 nm collected at the 620 nm wavelength, and a narrower emission band at 620 nm collected at the 478 nm wavelength.

3.1.3.2 Structural Development of the Composite Coatings

Many wet processing approaches—for example, casting, spin coating, and those with doctor blades—were used to obtain PDMS composite homogeneous in terms of both particle dispersion and film thickness. To obtain homogeneous, well-dispersed phosphor particles, the primary requirement of the approaches is to form stable colloid dispersion. The sedimentation of the phosphor colloids is inevitable, since the density of the particles is far greater than that of the polymer and solvent. This density mismatch renders solution-based processing nearly impossible, as well as deteriorates the homogeneity of the coating. Although stabilizing the particles using various surfactants, including cetyltrimethyl ammonium bromide, sodium dodecyl sulfate, and Triton X-100, was studied, none of the surfactants could stabilize the large particles in the polymer solution. Therefore, spray coating appears to be the most convenient approach for forming composite coating with large, heavy particles along with a minor amount of polymeric

carrier. Moreover, unlike with other wet processing methods, the high particle content can be loaded into the polymeric system.

Two different spraying strategies were employed. In the first, the PDMS/YAG:Ce³⁺ dispersion was sprayed as the first layer, upon which PDMS–red phosphor was sprayed

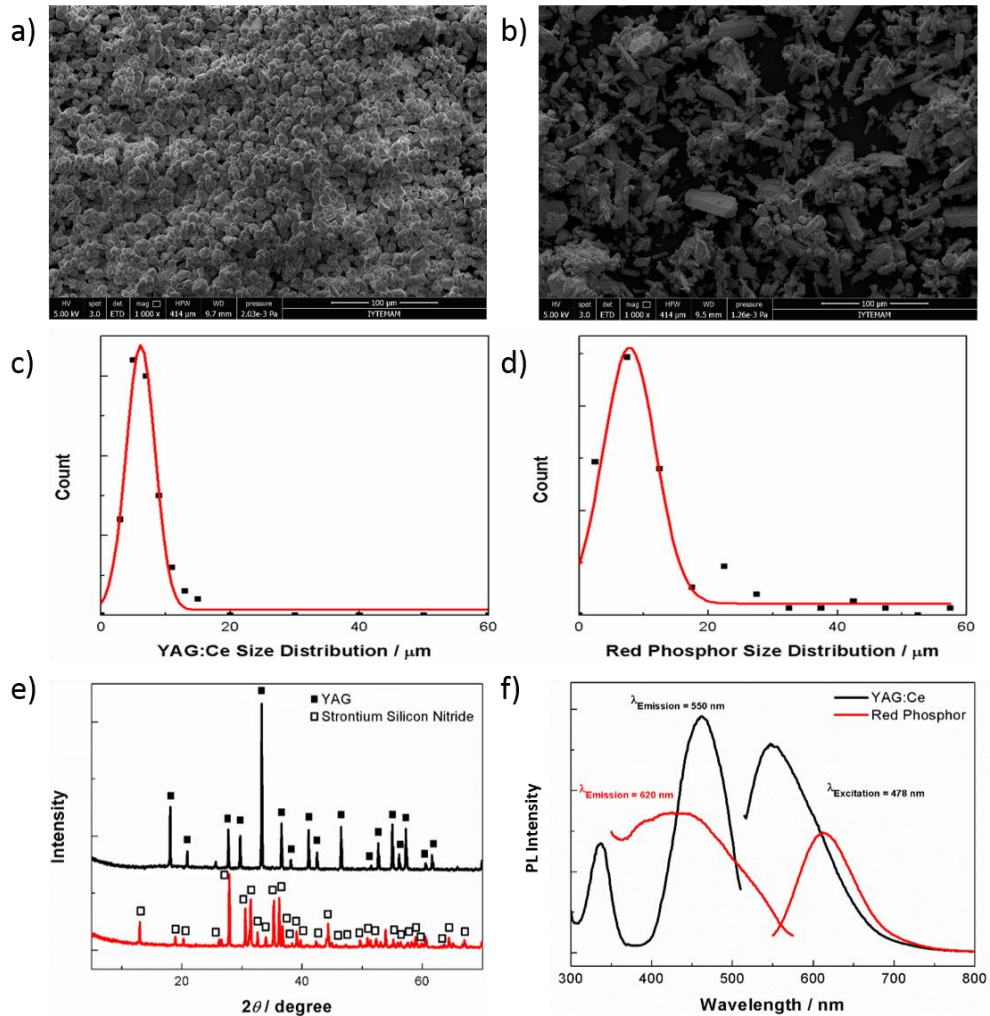


Figure 3.2. SEM images of a) YAG:Ce³⁺, and b) red phosphor powders. Size distribution of these related phosphors, c) YAG:Ce³⁺, and d) red phosphor are also calculated. Panel e is the XRD pattern of phosphor powders, and f) is PL spectrum of the phosphor powders. Excitation spectrum was recorded with emission wavelength at 550nm, and emission spectrum was recorded with the excitation wavelength at 478 nm which is same as the blue LED for YAG:Ce³⁺ (black line). For the red phosphor (red line), excitation spectrum was recorded at emission wavelength at 610 nm. Emission spectrum details are same with the YAG:Ce³⁺.

as the second (**Figure 3.1**). In the second strategy, YAG:Ce³⁺ and red phosphor were mixed with PDMS solution and sprayed on PC substrate at once. In both spraying strategies, pristine PDMS (i.e., without particles) was initially sprayed onto the PC substrate as the so-called zeroth layer. Since particles are much heavier than the surrounding PDMS matrix, they have a strong tendency toward sedimentation through the substrate in the long run, even though the matrix is crosslinked. Such engulfment may cause a segregation of the phosphor particles at the interface of the PC substrate and PDMS matrix. The homogeneous dispersion of the particles in coating eventually worsens particle dispersion and precludes optical stability. (Rimai and DeMejo 1996, Rimai et al. 1997, Rimai et al. 2002)

Crosslinking PDMS occurs via the hydrosilylation of a difunctional vinyl-ended oligomers and four functional groups of the crosslinker methylhydrosiloxane. A Pt catalyst under ambient atmospheric conditions catalyzes the crosslinking reaction, thereby achieving a network throughout the coating volume. During crosslinking, Si-CH=CH₂ bonds of the oligomer interact with Si-H bonds of the curing agent. As a result, Si-CH₂-CH₂-Si chains form intricately until the curing agent is consumed. At the same time, the disappearance of the vibrational signal of Si-H at 2163 cm⁻¹ hints at the progress of crosslinking, the reactions of which were monitored for 2 h. **Figure 3.3 (a)** presents attenuated total reflection mode of the corresponding FTIR spectra of the crosslinking process registered at 4000–400 cm⁻¹. With time, the intensity of this vibrational signal with respect to time disappears, thereby indicating the progress of the crosslinking reaction.

The same process was performed in the presence of 10% and 40% phosphors by mass. **Figures 3.3 (b) and (c)** show the first and second derivative of the intensity of the signal in the presence of 10% and 40% particles, respectively; the first refers to the absorbance signal's rate of change (i.e., speed), whereas the second presents the acceleration of the process. PDMS alone has the highest initial change rate, which is followed by an exponential decrease with respect to time. However, in the presence of phosphor, the initial change rate becomes remarkably reduced. The reduction becomes more remarkable as the phosphor content increases. For instance, at 30 min, the initial rate of the neat PDMS was 85%, yet 79% and 52% for the 10% and 40% particle content, respectively. Similarly, the acceleration of the process reduces the initial Si-H content; whereas it was 85% for PDMS alone and decreased to 58% for PDMS coating with 10% phosphor particles, there was nearly no acceleration for the PDMS–phosphor 40%

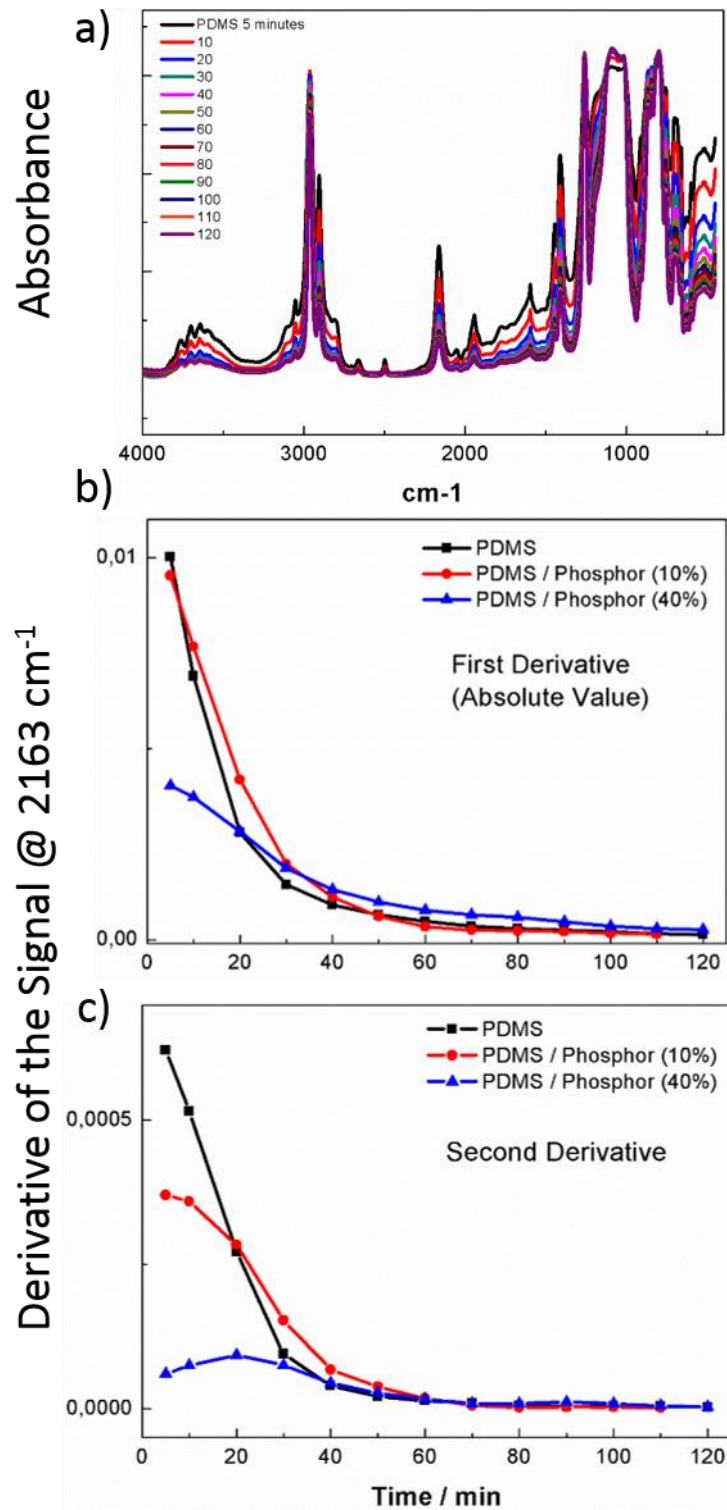


Figure 3.3. FTIR spectrum of cross-linking process. Panel a) presents the change of FTIR signals with respect to time was shown for neat PDMS. In panel b, and c, effect of the different phosphor contents on the FTIR signals during cross-linking were analyzed by focusing on first and second derivatives of the Si – H signal at the 2163 cm⁻¹ respectively.

sample. Clearly, crosslinking is remarkably hindered in the presence of garnet particles, yet nevertheless had been completed in 2 h. The reason for such results could be the hindrance of the diffusion of precursors in the presence of large phosphor particles. Alternatively, such hindrance could stem from the interaction of the particle surfaces with precursors of PDMS in the *in situ* crosslinking process. For confirmation, the particles were treated with the difunctional vinyl-ended oligomer methylhydrosiloxane and crosslinking counterparts, albeit separately. The diffuse reflectance infrared Fourier transform of the particles was registered after isolating the garnet particles via sedimentation and rigorous washing. The spectra of the particles showed strong Si-CH₃ signals that stretched at approximately 2900 cm⁻¹. The presence of the signals in both spectra could suggest a remarkable interaction between particle surface and both PDMS and the curing agent.

Figure 3.4 (a) shows the optical microscope image of composite coating prepared by spraying YAG:Ce³⁺ and red phosphor consecutively on a neat PDMS layer. Displayed with differently colored arrows, phosphor particles seemed homogeneously dispersed over a 50 × 50-μm² area. A cross-section of the composite films prepared by consecutive spraying was examined by SEM, and the electron micrograph in **Figure 3.4 (b)** verifies three distinct layers. The zeroth layer is the first layer on the substrate, above which phosphor particles are evident; a dashed line guiding the eye indicates that yellow particles are sandwiched between the zeroth PDMS and red phosphor/PDMS layers. Assuming the homogeneous dispersion of particles throughout coating, >10⁶ phosphor particles were expected per cm² of coating.

By contrast, the YAG:Ce³⁺ and red phosphor mixture in **Figure 3.4 (c)** is clearly heterogeneous, implying that mixing two different phosphor particles causes the formation of large clusters of phosphor particles, as well as indicates an incompatibility between phosphor particles. To gain further insight into the reason for such heterogeneity, YAG:Ce³⁺ and red phosphor particles were dispersed into the PDMS-hexane solution, albeit separately. The surface charge of the particles was measured by the zeta potential mode of dynamic light scattering (**Figure 3.4 (d)**); for instance, YAG:Ce³⁺ is an oxide particle in nature, and its charge is negative at nearly -10 mV. The origin of the negative charge could be the partial dissociation of the surface hydroxyl group inevitable with any oxide on a particle surface. At the same time, red phosphor showed positive potential at nearly +5 mV. When both YAG:Ce³⁺ and red phosphor were mixed in the PDMS-hexane solution during spraying, a Coulombic attraction occurred between the negatively charged

yellow and positively charged red particles such that large pseudo-clusters formed in the dispersion and thus in the resulting coating.

3.1.3.3 The Optical Performance of Composite Coatings

Figures 3.5(a) and (b) show the PL spectra of the composite coatings obtained by remote and direct measurement strategies, respectively. Regardless of phosphor type employed, an unidentified weak emission signal was obtained at 610 nm in all spectra; this signal might have originated from an impurity in the phosphor system or from the ore in which mineral phosphor particles were achieved, if not both. An intensely sharp

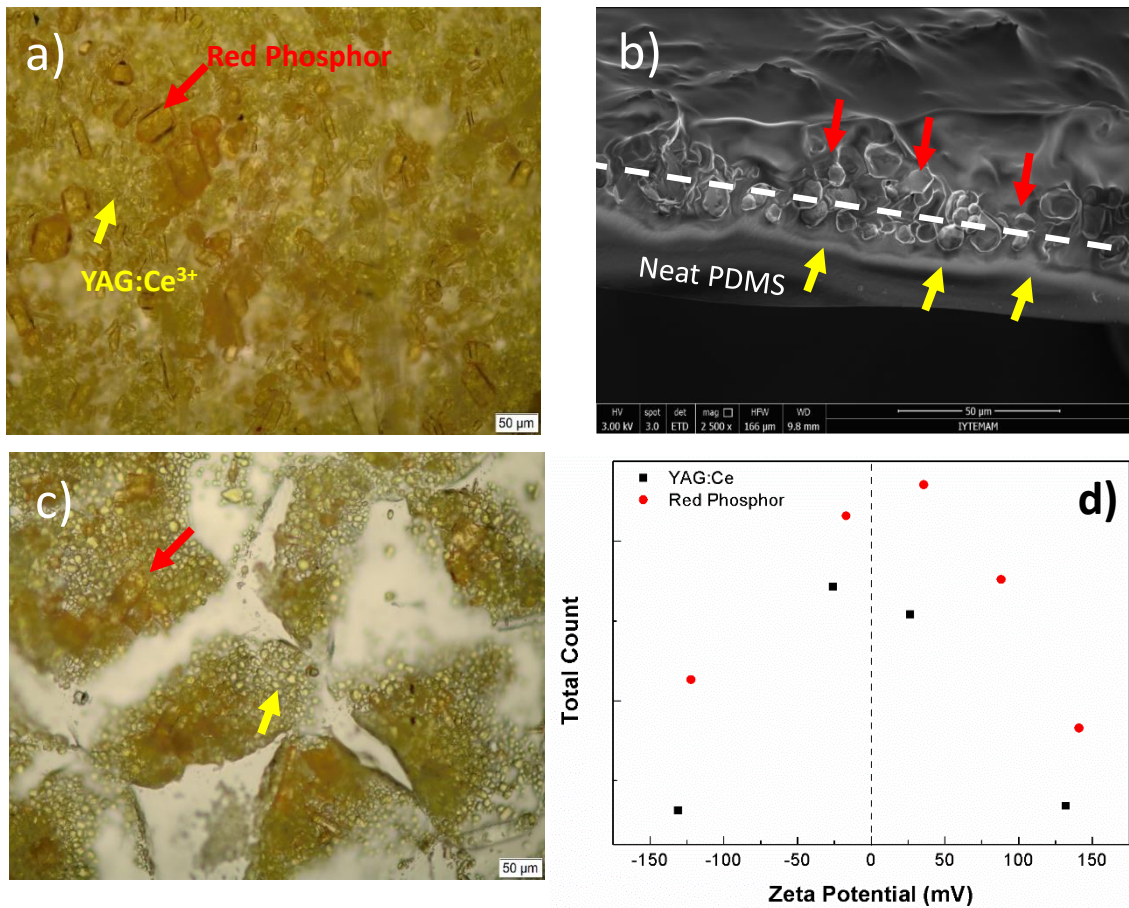


Figure 3.4. Optical microscope image of **a)** mixture as single layer sample **b)** is the optical microscope image of the stacking **c)** is the SEM image of stacking sample but focused on the cross section under 2500 x magnification. Red and yellow arrows show the red phosphor and YAG:Ce³⁺ particle(s), respectively **d)** Surface charge of the phosphor particles in PDMS/hexane solution by zeta potential mode of dynamic light scattering.

signal at 478 nm was attributed to the primary blue light from the blue LED, whereas the broad signal at 550 nm with relatively lower intensity referred to the emission of YAG:Ce³⁺ garnet particles. The 4f → 5d transition of the Ce³⁺ ions in the garnet structure absorbed the incoming blue light, while its corresponding emission appeared in the yellow region. (Demir and Wegner 2012) Because blue and yellow are complimentary colors, their combination resulted in white light emission.

The chief difference between the direct and remote sets of spectra is the ratio of signals in blue and yellow regions. Signals obtained from the direct measurement were

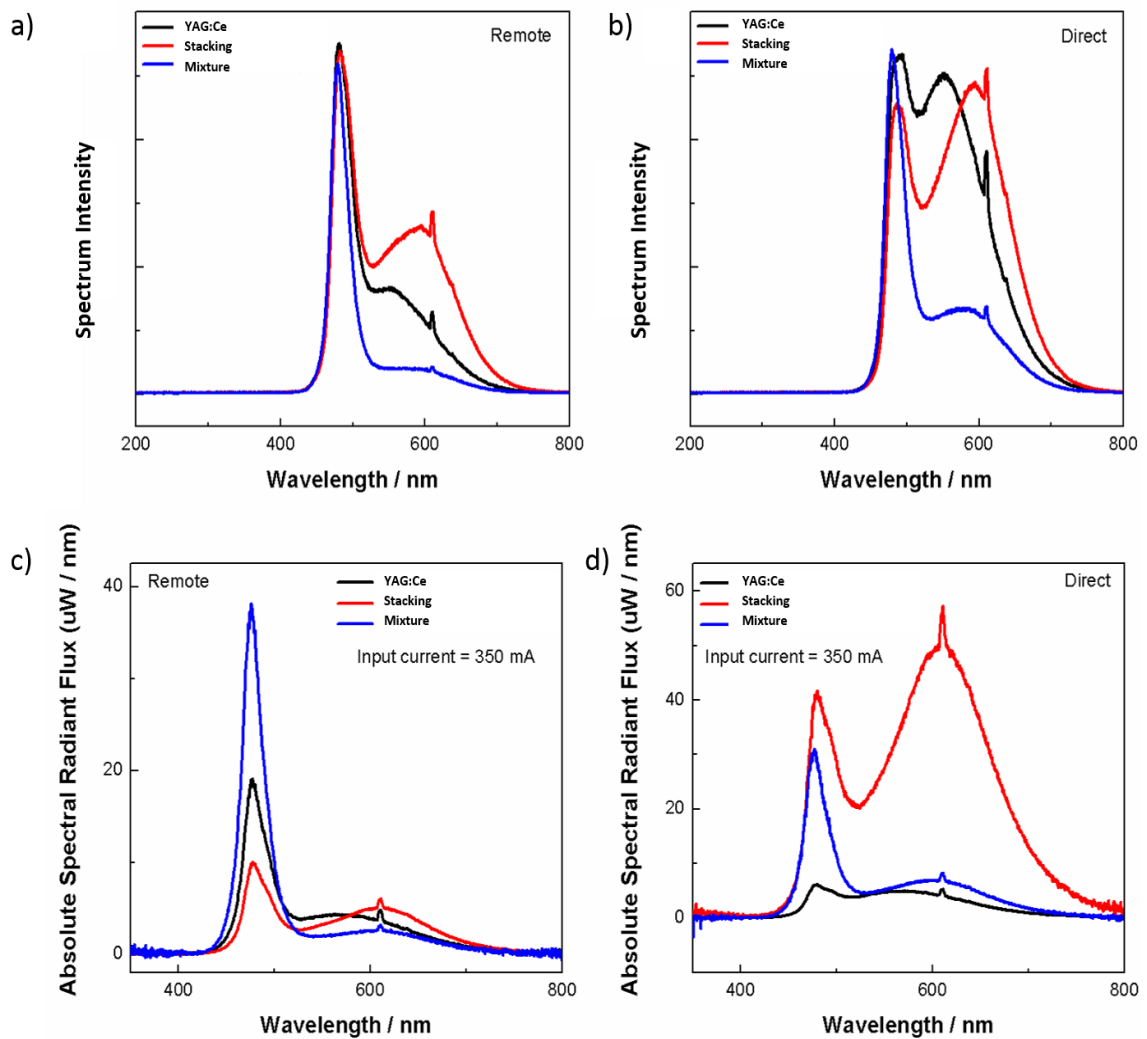


Figure 3.5. Spectrum of PDMS / phosphor coated PC substrates. a) remote phosphor measurement was done at 3 cm away from the blue LED source. b) direct phosphor measurement was done without having any distance between sample and blue LED source. Irradiance of samples under blue LED illumination having 0.35A input current collected by using the remote (c), and direct measurement (d).

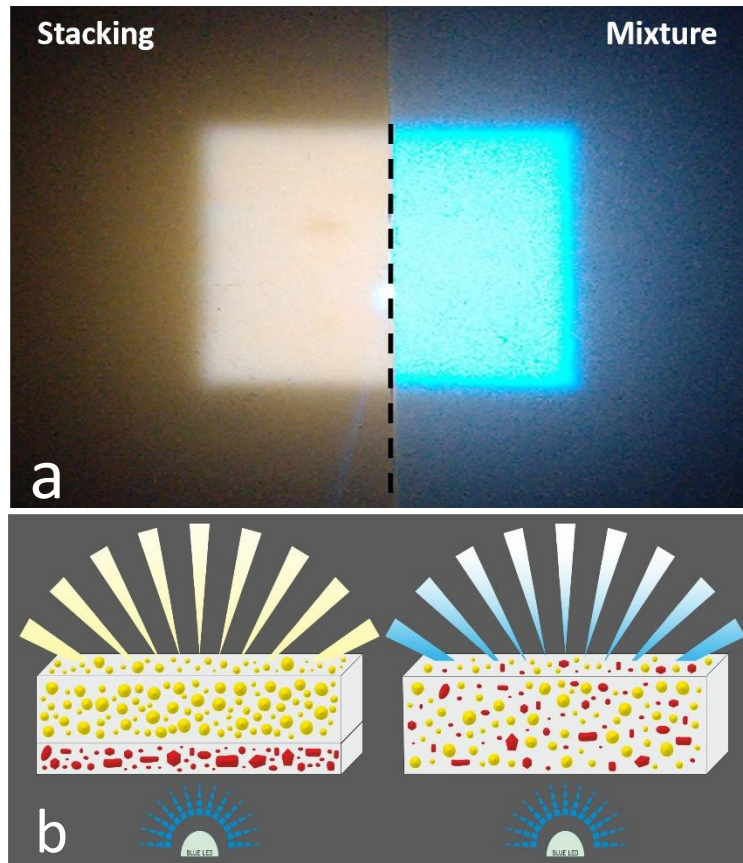


Figure 3.6. **a)** Comparison of illumination of the coatings prepared by the mixture and stacked layers of the phosphor particles **b)** cartoon demonstration of the interaction of blue light with coatings prepared with two strategies. The one prepared by consecutive spraying provides adequate quality of warm white light.

greater than with remote measurement. Since the distance of the phosphor layer and the blue LED was closer, yellow phosphor particles were more intensively exposed to blue light. As a result, the emission unsurprisingly appeared greater with direct measurement.

The quality of white light can be determined from the ratio of blue and yellow signals in the spectrum.(Tran, You, and Shi 2009a) Since YAG:Ce^{3+} is deficient in the red region, $\text{Sr}_2\text{Si}_5\text{N}_8\text{:Eu}$ can be added to improve quantity-related color properties (e.g., CCT). Upon incorporating red phosphor, the overall emission shifted from 550 to 605 nm; however, the arrangement of the phosphor with respect to the incoming blue light strongly influenced the color properties of the white light; for instance, the coating prepared by spraying YAG:Ce^{3+} and red phosphors consecutively as stacked layers presented far greater emission over the yellow–red region than spraying the mixture of

the phosphors once in a single layer, even though they had the same amount and composition of phosphors. **Figures 3.5 (c) and (d)** show the absolute spectral flux obtained from remote and direct measurements, respectively. Clearly, the mixture has intense blue light, which reduces the contribution of phosphors in developing white light. The inadequacy of the mixture in all optical properties emerged simply due to the presence of large empty spaces across the film, as shown in the optical microscope images (**Figure 3.4 (c)**). Blue LED escapes from empty regions without any interaction. At the same time, since those spaces exist less in coating prepared in stacked layers of multiple phosphors using consecutive spraying, a homogeneous dispersion of phosphor particles in two layers over coating can be achieved. **Figure 3.6 (a)** shows photographic images of white light produced as obtained by downconverting blue LED by coatings via stacking layers and the random mixture of phosphor particles; the former displayed much better as a white light source in terms of human perception, thereby confirming the microscopy and spectroscopy results above. It should be noted that in the stacked layer arrangement, the sequence of phosphor layers is critical. Blue LED first contacts red phosphor, whose emission at approximately 610 nm cannot excite yellow YAG:Ce³⁺. Otherwise, blue LED's first contact with the YAG:Ce³⁺ emission from those yellow phosphors is absorbed by the red phosphor, which renders the use of red phosphor inefficient (**Figure 3.6 (b)**).

Table 3.1. Color chromaticity CRI, CCT, and luminous efficacy of the coatings to both remote and direct phosphor configurations.

^aNo meaningful results were obtained from the measurement.

Sample	CIE _x		CIE _y		CRI		CCT (K)		LER (lm / W)
	Remote	Direct	Remote	Direct	Remote	Direct	Remote	Direct	Remote
YAG:Ce ³⁺	0.3	0.4	0.3	0.4	61±1.0	72±1.0	8620±200	4500±50	253
Stacking	0.4	0.4	0.4	0.4	68±1.5	82±1.0	4300±90	2900±100	264
Mixture	a	0.3	a	0.3	a	54±1.0	a	8000±100	165

Table 3.1 shows CRI, CCT, and efficacy values. The coating prepared with YAG:Ce³⁺ only showed 4,500 K, 61 CRI, and 253 lm·watt⁻¹ luminous efficacy. YAG:Ce³⁺ in PDMS thus seems adequate in fabricating cool, white light, yet with limited efficacy. However, coating prepared with the mixture of YAG:Ce³⁺ and red phosphor in spraying was inadequate and even worse than coating prepared with YAG:Ce³⁺ alone. The clustering of phosphor particles resulted in large empty regions dominated by blue light such that CRI and CCT could not be successfully registered in remote measurements. The coating consisting of phosphor particles in two distinct layers improved both color properties and light output; CCT, CRI, and luminous efficacy were 2,900 K, 68, and 264 lm·watt⁻¹, respectively, and color space coordinates x (CIE_x) and y (CIE_y) were between 0.3 and 0.4. These values were also assessed for direct measurement, which generally provided higher values for both CRI and CCT. Note that those values can be adjusted by simply arranging the distance between the phosphor layer and the light source.

In real-time applications, PDMS–phosphor coatings are exposed to blue light for a long time. Such exposure can eventually trigger secondary reactions and cause undesirable consequences—for instance, the degradation of PDMS that may have adverse effects on the film’s optical stability. When blue LED continuously illuminated a piece of representative coating of stacked layers for 4 weeks, periodically registered spectra remained unchanged, thereby indicating that the coating was stable under blue light, at least in the range of conditions employed (i.e., time and atmospheric humidity) in this study.

3.1.3.4 Simulation

The arrangement of phosphor particles in the PDMS matrix was simulated using the Monte Carlo approach developed with the programming language Python;(Hunter 2007) program codes appear in the Appendix B. The spectra were simulated between the 400 and 750 nm wavelengths, considering stacking and random mixture separately. Assuming monolayer coverage of the substrate by phosphor particles, the intensity of the resulting light was determined by the algorithm for each wavelength. When light impinged the phosphor coating, the intensity was attenuated via two mechanisms—namely, absorption and scattering—the probability of each of which is calculated by a partition function consisting of Gaussian functions representing all possible emissions—that is, blue LED

as transmission and both yellow and red as re-emissions—by following the formulas(Shen et al. 2016)

$$I_{tm} = I_0 \exp\left(-4 \ln 2 \frac{(\lambda - \lambda_{tm})^2}{FWHM_{tm}^2}\right) \quad (3.1)$$

$$I_{rm}(y|r) = I_{rm}(y|r) \exp\left(-4 \ln 2 \frac{(\lambda - \lambda_{rm})^2}{FWHM_{rm}^2}\right) \quad (3.2)$$

in which I_0 , and $I_{rm}(y|r)$ are the peak intensities of blue LED, YAG:Ce³⁺, and red phosphors in the experimentally measured spectra, respectively, λ is the wavelength, and λ_{tm} , λ_{rm_y} and λ_{rm_r} are the corresponding wavelengths of the peak intensities of blue LED, YAG:Ce³⁺, and red phosphor. Similarly, $FWHM_{tm}$, $FWHM_{rm_y}$, and $FWHM_{rm_r}$ are at full width at half of the maximum of related blue LED, YAG:Ce³⁺, and red phosphor. The total possible event is thus

$$I_{total} = I_{tm} + I_{rm_y} + I_{rm_r} \quad (3.3)$$

in which I_{rm_y} and I_{rm_r} are the corresponding spectrum intensity of YAG:Ce and red phosphor, respectively. As a result, the probability of each event in the corresponding wavelength in the spectrum can be defined as:

$$p_{tm} = \frac{I_{tm}}{I_{total}} \quad (3.4)$$

$$p_{rm_y} = \frac{I_{rm_y}}{I_{total}} \quad (3.5)$$

$$p_{rm_r} = \frac{I_{rm_r}}{I_{total}} \quad (3.6)$$

in which p_m , p_{rm_y} , and p_{rm_r} are for the blue LED, YAG:Ce³⁺, and red phosphor, respectively. Peak intensities were determined by using **Figures 3.7(a) and (b)**, while peak intensity wavelength and FWHM parameters were calculated by using the PL spectrum in **Figure 3.2(f)**. Parameters are shown in **Table 3.2**. In stacking phosphor particles, incoming light first interacts with the red phosphor with a probability of 27%. YAG:Ce³⁺ is assumed to interact with light based on the 3.7:1 volumetric ratio of YAG:Ce³⁺ and red phosphor.

Blue light will be either transmitted or absorbed by red phosphor, thereby prompting an emission. The YAG:Ce³⁺ layer of the sample interacts with blue light either directly, with a probability of 73%, or indirectly after scattered from the red phosphor.

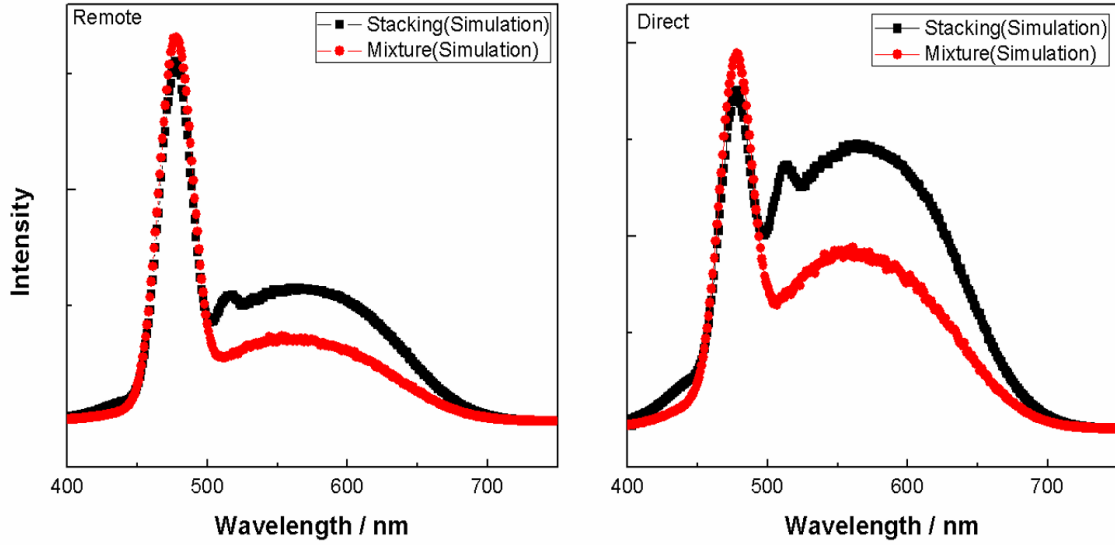


Figure 3.7. Remote and direct spectrum obtained by simulation of stacking and mixture arrangement of phosphor particles in the PDMS coating.

Following the same strategy, incoming blue light is either transmitted or absorbed by YAG:Ce³⁺ and causes a yellow emission. In every step of the interaction, the algorithm compares probabilities, determines the result 3,000 times at each wavelength, and takes

Table 3.2. Peak intensity, peak intensity wavelength and FWHM values of both remote and direct case used in the simulation.

Strategy	Peak Intensity			Peak Intensity Wavelength			FWHM		
	I_{trans}	$I_{reemiss}$	$I_{reemiss_r}$	λ_{trans}	$\lambda_{reemiss_y}$	$\lambda_{reemiss_r}$	$FWHM_{trans}$	$FWHM_{reemiss_y}$	$FWHM_{reemiss_r}$
Remote	884	373	355	478	550	620	30	129	82
Direct	1055	952	935	478	550	620	30	129	82

the average of the set of determinations. In the random mixture of the phosphor particles, the total empty region of the image of the optical microscope in **Figure 3.4(c)** was first

calculated by using ImageJ; the result was 40%. Incoming blue light was directly transmitted with 40% probability. In the case of interaction, again due to the 3.7:1 volumetric ratio, incoming light hit the red phosphor with 22% and the YAG:Ce³⁺ with 78% probability. Regardless, transmission or absorption occurred according to the probabilities defined in **Equations 3.1–3.6** for the corresponding wavelengths. **Figure 3.7** shows the results of simulating both remote and direct spectra; simulation shows the superiority of stacking layers over using the random mixture. In that sense, the results of simulation agree with the experimental results.(Zhu and Narendran 2010)

3.1.4 Conclusion

In this study, we investigated the fabrication of PDMS-based phosphor coating with yellow YAG:Ce³⁺ and red phosphor by spraying. After the interaction of material components during the structural development of the coatings was examined, the mixture of PDMS and phosphor particles were sprayed on a PC substrate, and the resulting coating was subjected to crosslinking at 100 °C. The phosphor particles with micrometer-sized diameters hindered, yet did not entirely obstruct the completion of the crosslinking process. Although red phosphor was integrated into the system, electrostatic interaction existed between YAG:Ce³⁺ and red phosphors, thereby causing the clustering of phosphor particles. As a result of clustering, cracks appeared in the coating, blue light dominated, and the light become cold white. Spraying yellow and red phosphor particles consecutively in stacked layers improved optical features compared to coating prepared by spraying the mixture as a single layer at once. The highest light output was obtained when the longer wavelength of red phosphor was placed on the YAG:Ce³⁺ as the second layer. This method was highly versatile in obtaining coating materials on a large scale in a brief processing time and suitable in potential applications in both direct and remote solid-state lighting.

3.2 Optical Enhancement of Phosphor-Converted WLEDs Using Glass Beads

In this section, we will give details about our work on enhancement of the optical properties of the generated white light through employing glass beads into the composite

system. We characterize the used samples, and investigate the white light properties of the system composing of glass beads and yellow phosphors.

3.2.1 Materials and Methods

Phosphor powder of YAG:Ce³⁺ (HB-4155H, Zhuhai Hanbo Trading Co., Ltd., Guangdong, China) and glass beads having refractive index $n=1.51$ at sodium D line (Potters Industries LLC, USA) were used as received. PDMS (SYLGARD 184 Kit, Dow Corning, Midland, MI, USA) was used as polymer matrix. Hexane (>95%, Sigma–Aldrich, St. Louis, MO, USA) was used to thin the PDMS powder solutions because of PDMS's high viscosity.

3.2.2 Preparing the PDMS / (Phosphor - Glass Bead) Composite Films

PDMS coatings were prepared on diffuser polycarbonate (PC) substrate by spray-coating (Mac Allister PLD 3010, 500 W). Spray coating atomizes the given solution or dispersion via high air pressure. In a typical coating, PDMS oligomers and curing agent were employed in a 10:1 ratio with respect to mass. The amount of inorganic material (GB + phosphor) fall in the range of 50-55% wrt PDMS. For proper spraying, dispersion of PDMS / phosphor was thinned by hexane and then mixed in a magnetic stirrer. The dispersion consisting of hexane, PDMS, phosphor, and GB placed into the hopper of a spray gun with glass vial. The dispersion was sprayed onto PC diffuser. The resulting thickness of the composite coating for YAG:Ce³⁺ was in range of 60 - 100 μm depending on the solid content. Samples were left in room temperature overnight so that the hexane could fully evaporate, after which they were cured at 120 °C for 1 h in an oven.

3.2.3 Optical Measurement

Remote measurement setup was designed to simulate a remote phosphor configuration (Shuai et al. 2012a, Allen and Steckl 2008, Narendran et al. 2005, Tran, You, and Shi 2009b, Acuña et al. 2014). A fixed distance (3 cm) was maintained between the film and blue LED surface in a black chamber. LED (Cree, Royal Blue 1W, USA) that is used in this configuration emits a monochromatic light at 455 nm. Altogether, the system run with a 0.35 mA input current.

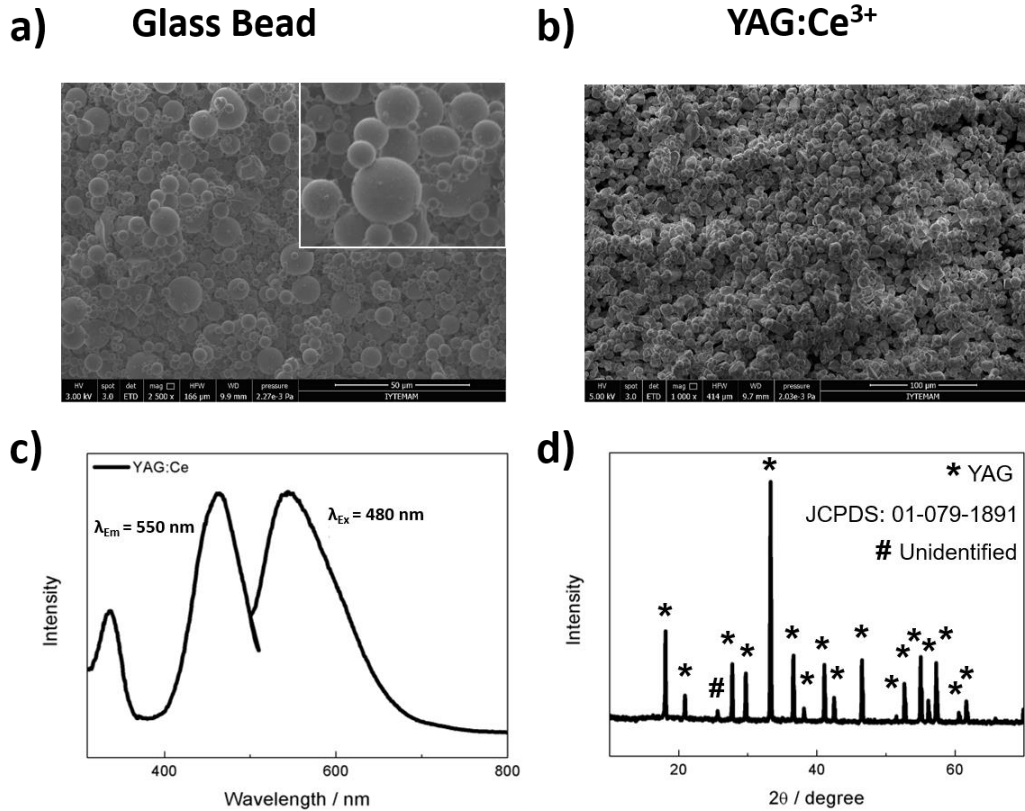


Figure 3.8. SEM image of the **a)** Glass Bead (inset is the magnified image of glass beads), and **b)** YAG:Ce³⁺. **c)** - **d)** present the PL spectrum, and X-ray diffraction of YAG:Ce³⁺, respectively.

3.2.4 Results and Discussion

In this section, we will give further information about the materials, and resulting PL spectrum and optical properties of the generated white light.

3.2.4.1 YAG:Ce³⁺ and Glass Beads

Morphological and structural characterization of both YAG:Ce³⁺ and glass beads are given in **Figure 3.8**. In this sense, **Figure 3.8 (a)** and **(b)** show the SEM images and particle size distribution of both glass beads and YAG:Ce³⁺ respectively. It is observed that phosphor and glass bead powders depict spherical shape with having monodisperse distribution around 5 µm and 3 µm, respectively. Particle size distributions obtained statistically by counting particle sizes using ImageJ.(Schneider, Rasband, and Eliceiri 2012) **Figure 3.8 (c)**, two absorption bands centered at 340 nm and 460 nm are observed

by fixing the emission wavelength at 550 nm. These bands are related to splitted $4f \rightarrow 5d$ transition states of Cerium, which is due to crystal field effect (Tunusoğlu et al. 2012). On the other hand, emission spectrum was recorded by fixing the excitation wavelength at 458 nm. In **Figure 3.8 (d)**, reflections of phosphor powder were indexed with the crystallographic data of host material YAG with Joint Committee on Powder Diffraction Standards (card no: 01-079 – 1891).

3.2.4.2 The Effect of Glass Beads on the Optical Performance of Phosphor Layer

Figure 3.9 (a) shows the PL spectra of PDMS coatings containing a constant amount of phosphor and various concentrations of GB. The reference spectrum is obtained from a coating prepared using PDMS and phosphor particles without beads; this coating presents

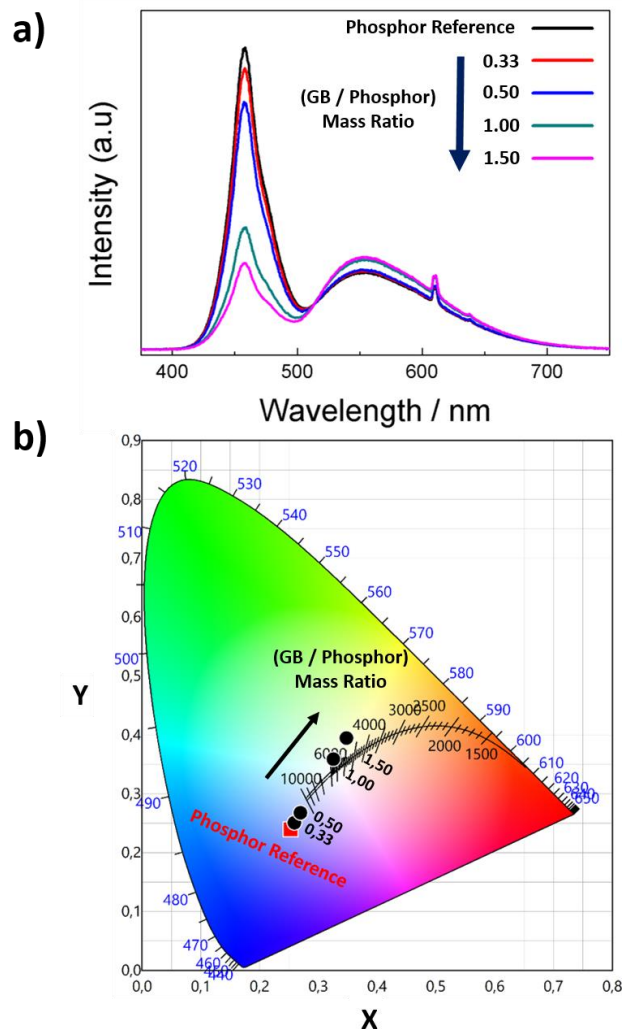


Figure 3.9. a) PL spectra of the coatings at fixed phosphor with GB at various contents. Phosphor Reference represents the phosphor-only coating, and b) the CIE 1931 color coordinates of these samples.

an efficacy of 121 lm/W, luminous flux of 0.248 lm, and no valid CCT or CRI, which means it does not generate white light.

Unsurprisingly, PDMS coatings containing phosphor particles provide two signals. The first signal lies in the blue region and could be attributed to the photons transmitted

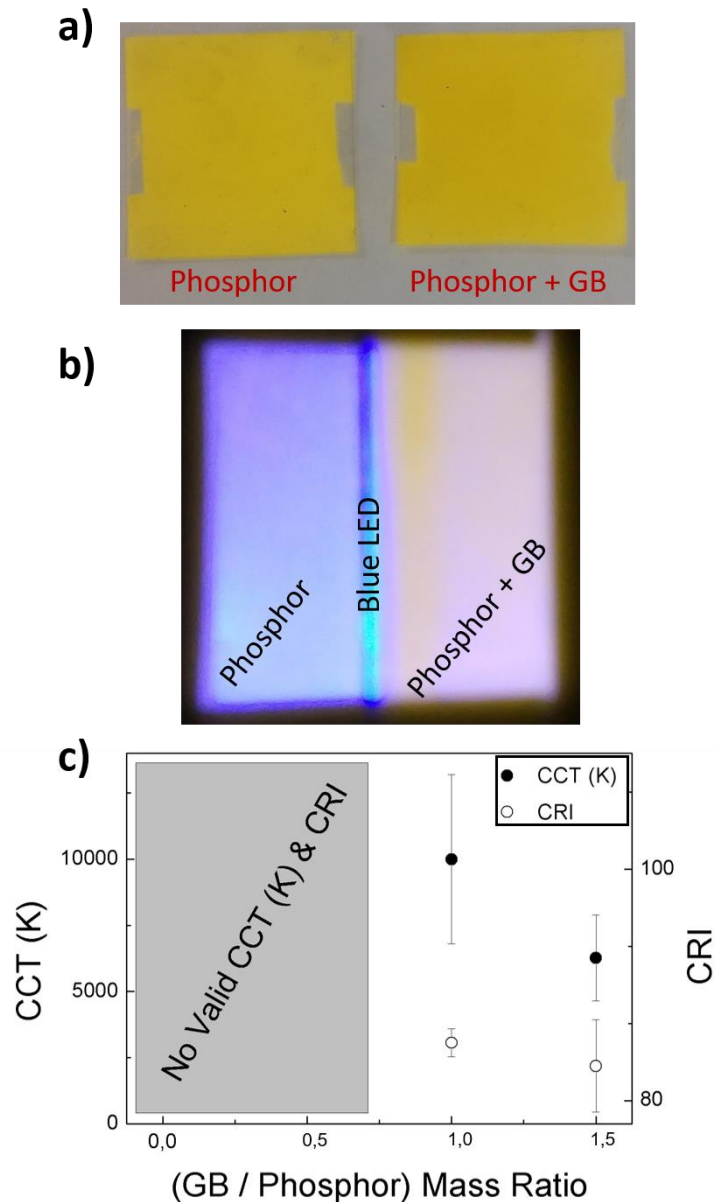


Figure 3.10. a) Appearance of the samples; phosphor-only coating and phosphor + GB (at the ratio 1.5), b) Photograph of the generated white light from the phosphor-only coating, and the phosphor + GB (at the ratio 1.5) coating under blue LED illumination with the driving current 0.35 mA. c) CCT, and CRI versus GB / phosphor mass ratio. Boundary between “No valid CCT (K) & CRI” and valid region represents the amount that phosphor-only coating requires for generating useful white light.

through the coating, while the second signal lies in the yellow region and could be attributed to the emission of the YAG:Ce³⁺ phosphor. The quality of white light in terms of CCT is related to the ratio of these two signals. The phosphor concentration is the most significant parameter influencing the production of white light, and a threshold concentration of yellow phosphor particles should ideally be maintained to produce good-quality light. A valid CCT for commercial applications appears only at a phosphor / (amount of inorganic material with respect to the solid content) ratio of 1.15.

In this study, we began with a ratio of 0.77, at which point no white light optical feature is found upon illumination of the coating with blue light. This result can be attributed to the lack of a yellow flux region in the coating. Addition of small amounts of GB to the PDMS + YAG:Ce³⁺ system, as shown in **Figure 3.9 (a)**, causes the shape of the spectrum to remain unchanged, i.e., two signals appearing in the blue and yellow regions are still observed. However, the ratio of these signals varies such that the transmission of blue light from the PDMS coating decreases (7%) while its yellow emission is maintained. The presence of GB can lead to a blue-signal reduction of nearly 71% and a simultaneous increase in yellow light emission of 20% at a GB/phosphor ratio of 1.5. **Figure 3.9 (b)** shows the CIE 1931 color coordinates of these samples. Phosphor reference shows an explicit blue color while it changes towards warm white color with the addition of glass beads. In **Figure 3.10 (a)**, photograph of both phosphor reference, and phosphor + GB coating at (GB / phosphor) mass ratio at 1.5 is given. The difference is that phosphor + GB sample has slightly more intensive yellow appearance than the phosphor reference. The effect of addition of GB to the coating on the white light generated can be observed explicitly in **Figure 3.10 (b-c)**. In **Figure 3.10 (b)**, differences between the phosphor and phosphor + GB coatings are shown photographically; here, samples are illuminated with a blue LED under a driving current of 0.35 mA. A highly bluish light is observed from the phosphor-only coating; this light not as blue as the LED light, but it cannot be considered a useful bluish white because it presents no valid CCT or CRI. In the presence of GB at a ratio of 1.5, a warm white light is observed. The CCT and CRI of this coating change from “not valid” to 6300 K and 83, respectively (**Figure 3.10 (c)**). An efficacy of 197 lm/W, indicating a significant improvement of 63%, is also observed. In other words, introducing GB to the phosphor system provides a means to achieve a viable and controllable white light source. A comparison of the phosphor-only coating (Phosphor / (amount of inorganic material with respect to the solid content) ratio, 1.15) with the phosphor + GB coating (GB/phosphor ratio, 1.5); the optical performance of these

coatings is nearly identical but the CCT of the phosphor + GB coating is markedly improved. This finding indicates that phosphor consumption may be reduced by about 33% by introducing GB to the system.

To verify this unique effect of GB, PDMS composites with Z-Cel (Sodium aluminosilicate), which are spherical and opaque particles with an average particle diameter of 2–4 μm , were prepared. Z-Cel has a refractive index and density similar to those of GB, and its volume fraction and phosphor content in the composite were fixed as identical with the GB/phosphor ratio of 1.5. The main difference between them is, Z-Cel is having a crystalline structure while GB is amorphous. **Figure 3.11 (a)** shows the overall spectrum of the phosphor + Z-Cel coating. While the presence of Z-Cel can reduce the amount of blue light emitted, it cannot enhance the yellow flux region. The CCT values of the phosphor + Z-Cel and phosphor + GB coatings were 5100 and 6300 K, respectively. However, the CRI of the phosphor + Z-Cel coating was 78 in comparison

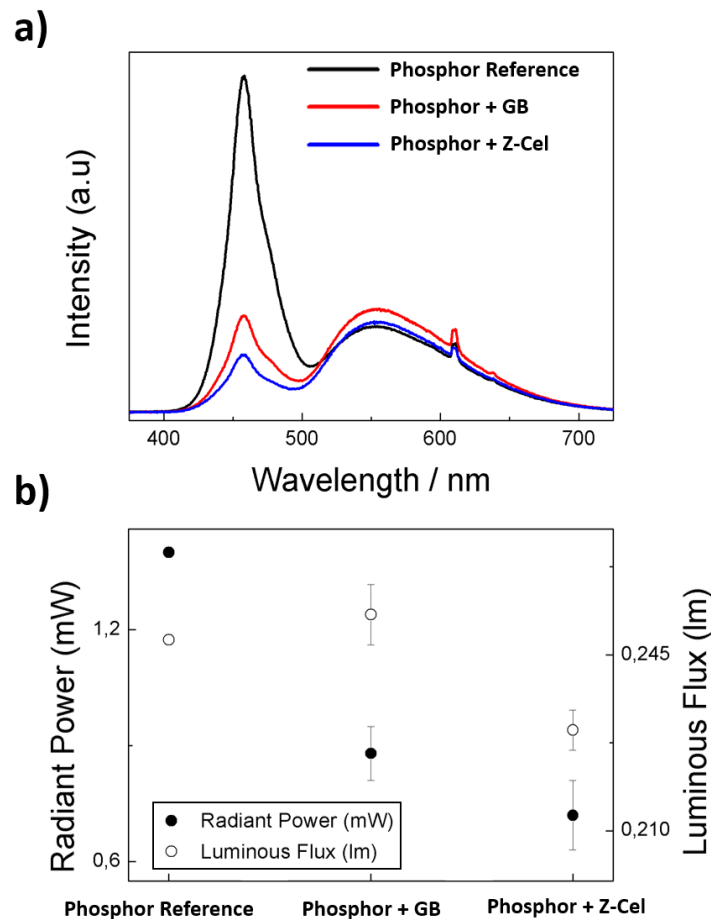


Figure 3.11. Comparison of phosphor + GB coating with a phosphor + Z-Cel in terms of their a) spectra, and b) radiant power and luminous flux. Phosphor Reference represents the phosphor-only coating

with the 83 of the phosphor + GB coating. Reducing the blue region alone can lead to tuning of the CCT; however, since no enhancement in the yellow flux region is observed, the phosphor + Z-Cel coating may be expected to show no improvement in luminous flux.

Figure 3.11 (b) shows the radiant power and luminous flux of the coatings. The luminous flux of the phosphor + Z-Cel coating is decreased (verifying the statement above) while that of the phosphor + GB coating shows improvement compared with the phosphor reference. This result indicates that light quality becomes poorer in terms of human vision when Z-Cel is used. Moreover, the phosphor + Z-Cel coating traps blue light more by increasing the total path length of the blue light, which means that it takes more time for blue light to escape from the coating. This increase is evidenced by a decrease in the radiant powers given in **Figure 3.11 (b)**; it is the highest for phosphor + Z-Cel compared to both phosphor reference and phosphor + glass bead samples. While CCT was not reduced significantly in the presence of Z-Cel, other optical performance parameters for instance CRI, luminous flux, and radiant power are noticeably decreased.

Increasing the GB or any scatterer content in the coatings shortens the transport mean free path,(Leung et al. 2014) which is the average distance the photons travel between two successive interactions between either phosphor and GB particles or GB and GB particles, and increases the multiple scattering of light within the coating volume. Blue light gets trapped more inside the coating volume since it scatters more extensively than yellow light(Leung et al. 2014, Vos et al. 2013). Therefore, a decrease in the blue light flux region takes place. This result is typically observed in both GB and Z-Cel, and the effect of this trapping in terms of reduction in the blue light is shown for either cases in **Figure 3.9** and **Figure 3.11 (a)**. Reducing the transmitted blue light from the sample via increasing the multiple scattering of light within the coating therefore requires no any specialty: it may work for any scatterer particles. However, **Figure 3.9** experimentally demonstrates that increasing the GB content of the coatings uniquely enhances the yellow flux region (which is not observed in the composite containing Z-Cel). This enhancement can be related to the difference between Z-Cel and GB in terms of their interaction with light; Z-Cel shows very high scattering behavior because of its crystallinity while glass bead can behave similar to a lens. In this sense, in addition to scattering of blue light, GB can show focusing, secondary reflections, and also may cause extra total internal reflections. Therefore, while both samples show reduction of blue light due to multiple scattering of light, it is assumed that the above difference between Z-Cel (as ordinary scatterer) and

GB in terms of their blue light interaction is responsible from the enhancement of the yellow flux region.

3.2.5 Conclusion

In this work, phosphor + GB coatings with varying GB contents were prepared, and the effect of GB on the optical features of the coatings was examined. Addition of GB as an optical element improved the CCT, CRI, and efficacy of the resulting coatings, and the possible reasons behind these improvements were discussed. Phosphor consumption could be reduced by nearly 33% by addition of GB (in this study, it is obtained at the particular GB/phosphor mass ratio of 1.5). These findings could be extended to a number of optical systems, such as afterglow materials, solar cells, and other lighting applications.

3.3 Green Fabrication of $\text{Y}(\text{OH})_3:\text{Eu}^{3+}$ Red Phosphors for White Light Generation

Obtaining suitable red phosphors to produce better phosphor-converted WLED systems having higher CRI and lower CCT is still an issue today. To date, numerous methods for obtaining red phosphor to be used either over blue LED or UV LED were reported. Among those, Eu^{2+} doped nitrides are promising red phosphors, and heavily employed already in WLED configurations. However, the synthesis conditions of these materials require harsh conditions such as high temperature and high pressure, and water-free solvents, which restricts their commercialization. Therefore, facile synthesis methods are also required in the case of red-emitting phosphor fabrication. In this context, several methods have been used widely such as, sol-gel, hydrothermal, combustion, emulsion, precipitation etc. (Li and Yanagisawa 2008, Higashi et al. 2017, Towata et al. 2008, Shiba et al. 2013)

Among those, sol-gel and co-precipitation method are, in general, slow, and usually involve additional steps. On the other hand, there is huge waste of organic solvents during the emulsion process, which makes this method inefficient in terms of cost and toxicity. Surfactant-free hydrothermal synthesis methods are desirable since it is single step, rapid and also able to decrease the toxicity of nanocrystals. (Darr et al. 2017) Water-based

reactions at ambient conditions are highly desired for the phosphor synthesis. In this study, luminescent red $\text{Y}(\text{OH})_3:\text{Eu}^{3+}$ phosphors were obtained in LiOH/water solution. It has been found that doping was achieved rapidly, even after 5 min. However, it took 1 h for complete crystallization. During the reaction process, Li ions distort the crystal structure and lead to increase in the formation of substitutional defects, where Y is replaced by Eu ions. (Li et al. 2012, Bai et al. 2009, Dubey et al. 2017, Zhao et al. 2013) To date, synthesis conditions of $\text{Y}(\text{OH})_3:\text{Eu}^{3+}$ were reported as requiring different reaction temperatures with various reaction times, from 12 h to several days. (Yanli et al. 2009, Wang, Peng, and Li 2011, Saravanan et al. 2015, Zhang et al. 2008, Li, Yanagisawa, and Kumada 2009) Therefore, production of $\text{Y}(\text{OH})_3:\text{Eu}^{3+}$ phosphors at room temperature for 1 h is a challenge, and this material can be promising red phosphor to be used as a down-conversion material for white light generation. (Choi et al. 2013, Sotiriou, Schneider, and Pratsinis 2010, Jayasimhadri et al. 2010, Buissette et al. 2006)

3.3.1 Materials and Methods

Yttrium (III) acetate hydrate ($\text{Y}(\text{Ac})_3 \cdot \text{H}_2\text{O}$; >99%), europium (III) acetate hydrate ($\text{Eu}(\text{Ac})_3 \cdot \text{H}_2\text{O}$; >99%), lithium hydroxide (LiOH; 98%), was purchased from Sigma–Aldrich (St. Louis, MO, USA) and was used as received without any further purification. Cerium doped Yttrium Aluminum Garnet ($\text{YAG}:\text{Ce}^{3+}$, HB-4155H, Zhuhai Hanbo Trading Co., Ltd., Guangdong, China) was used yellow phosphor and PDMS (SYLGARD 184 Kit, Dow Corning, Midland, MI, USA) was used as the polymer matrix.

3.3.2 Synthesis of Eu-doped Yttrium Hydroxide Crystals

An amount of yttrium (III) acetate hydrate (5.63×10^{-4} moles) and europium (III) acetate hydrate (4.55×10^{-5} moles) were dissolved in 10 mL of deionized water. Subsequently, the mixture was stirred in glass container until appeared transparent. An amount of LiOH (0.04 moles) was added into the transparent solution, respectively. The solutions were mixed and sonicated for 5 minutes. After the sonication process, reaction was maintained for 1h at room temperature. Reaction mixture was cooled down and centrifuged 2 times with water and 1 time with ethanol (5m, 6000 rpm). After centrifugation, isolated products were dried in oven at 100°C for 1 hour.

3.3.3 Results and Discussion

Figure 3.12 presents X-ray Diffraction pattern of $\text{Y}(\text{OH})_3:\text{Eu}^{3+}$ phosphor at various reaction time. The characteristic reflections of $\text{Y}(\text{OH})_3$ appears at 16° , 28° , 30° , 33° , 42° , 44° , 50° , 51° , 54° , 59° , and 60° marked with * satisfying JCPDS: 01-083-2042. The pattern of starting material, i.e. unreacted yttrium acetate is given for the comparison. The evolution of the crystal is clearly seen in the patterns. When the yttrium acetate is treated with alkaline water even in 5 min, its reflections begin to disappear. The extension of synthesis time to 15 min reduces the intensity of reflections, at the end of 45 min, characteristic signals of the $\text{Y}(\text{OH})_3$ labeled with * become more evident. After 60 min reaction time, reflection signals of the resulting crystals were found to be perfectly matched with the crystallographic data of JCPDS: 01-083-2042.

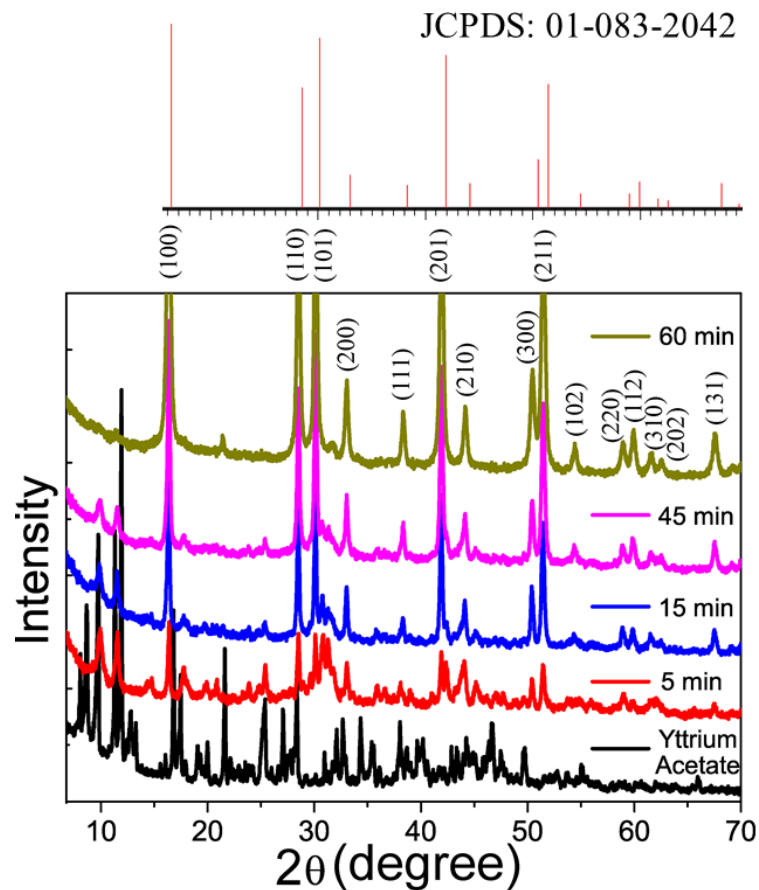


Figure 3.12. XRD pattern $\text{Y}(\text{OH})_3:\text{Eu}^{3+}$ phosphors prepared at various reaction times; 5, 15, 30, 45, and 60 min.

Figure 3.13 shows photoluminescence spectrum of the $\text{Y}(\text{OH})_3:\text{Eu}^{3+}$ phosphors registered at 365 nm excitation wavelength. At first 5 min, sharp emission signals appear at 592, 595, 613, 616, 690, 697 and 700 nm indicating specific D-D and D-F transitions of Eu^{3+} states due to crystal splitting in the $\text{Y}(\text{OH})_3$ host. As the synthesis time is extended, the intensity of the signals at 592 and 697 nm a significant increase while the ones at 613 and 700 nm are diminishing. This variation in the emission signals may be the result of the crystallization. When the morphology of the crystals change, defect states may vary. SEM images presented in **Fig. 3.14(a-c)** demonstrate the morphology of the $\text{Y}(\text{OH})_3:\text{Eu}^{3+}$ crystals. The change in morphology of the crystals is evident. The phosphors obtained in 5 min reaction time shows needle-like shape with nano-scale size distribution (**Figure 3.14 (a)**). After 15 min, (**Figure 3.14 (b)**), the crystals grow larger and started to show rod-like structure with sub-micron sizes. As the reaction time is extended to 60 min, the

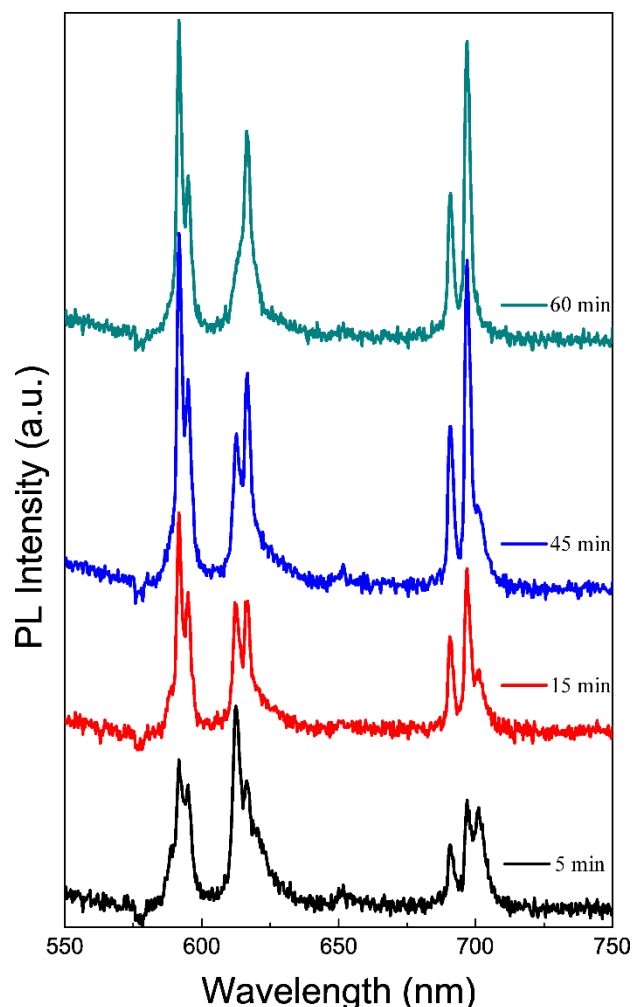


Figure 3.13. PL spectrum of $\text{Y}(\text{OH})_3:\text{Eu}^{3+}$ phosphors obtained at various reaction times; 5, 15, 30, 45, and 60 min.

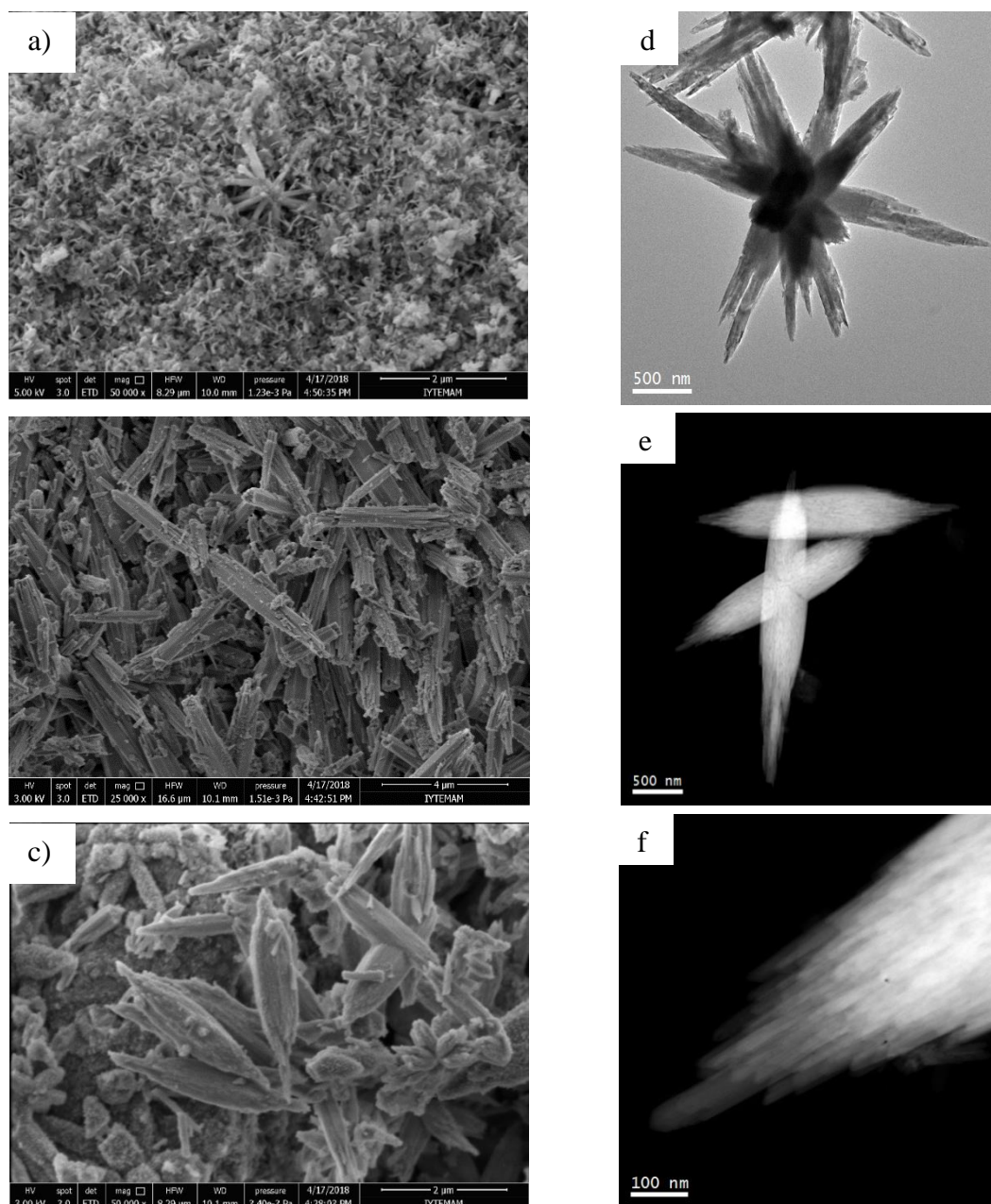


Figure 3.14. SEM images of the $\text{Y}(\text{OH})_3:\text{Eu}^{3+}$ phosphors obtained at different synthesis times; a) 5 min, b) 15 min, and c) 60 min. d-f) present the overview TEM and HAADF STEM micrographs of the particles prepared in 60 min. The sample is composed of micron-sized multipods, which seem to be controlled ensemble of ~ 10 nm thick nanowires.

crystals transform into rice-like structure while keeping their size (**Figure 3.14 (c)**). This may be the result of consumed reagents that stop the formation of new nucleated cores. Therefore, without nucleation, the size of the pre-formed individual crystals remains unchanged although the reaction temperature is fixed.

For more detailed information about the morphology of $\text{Y}(\text{OH})_3:\text{Eu}^{3+}$ crystals, general TEM and HAADF STEM micrographs of the 60 min sample presented in **Figure 3.14 (d-f)**. A multipod-like structure (**Figure 3.14 (d)**) together with rice-like ones (**Figure 3.14 (e-f)**) was obtained.

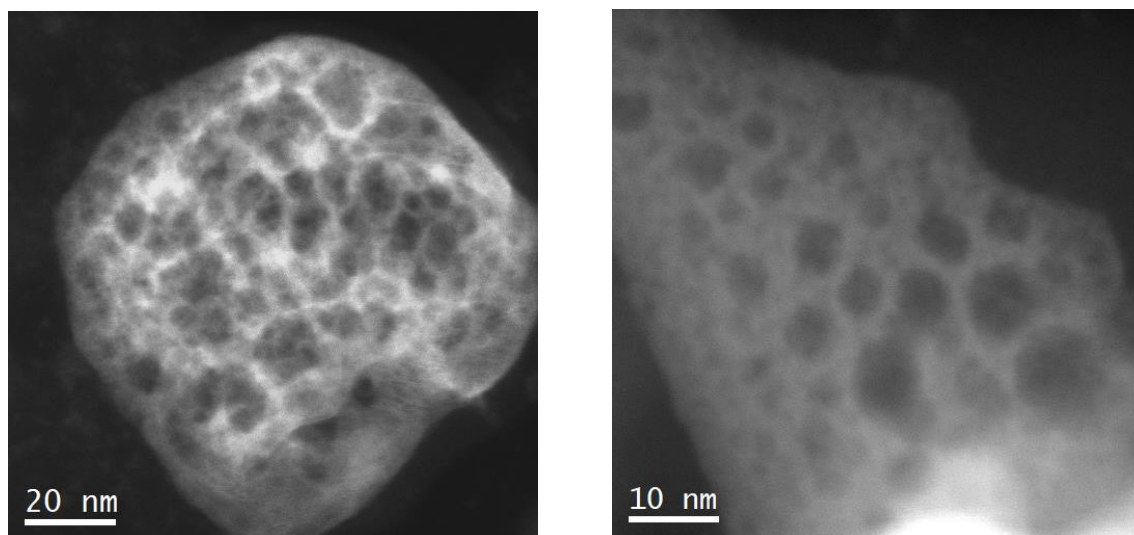


Figure 3.15. General HAADF STEM and TEM micrographs of the particles prepared in 5 min showing the presence agglomerated nanocrystals.

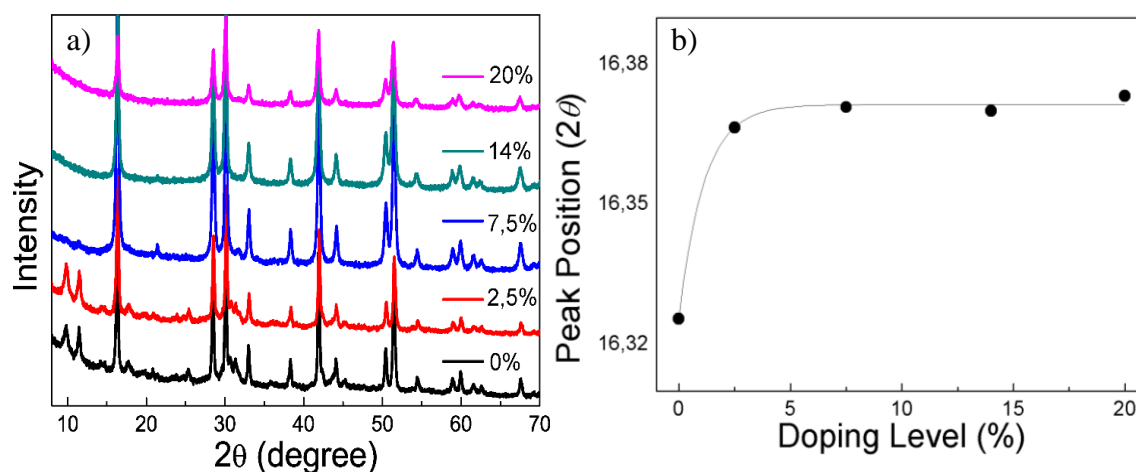


Figure 3.16. **a)** XRD pattern of the $\text{Y}(\text{OH})_3:\text{Eu}^{3+}$ phosphors with various doping ratios; 2.5%, 7.5%, 14%, and 20% by mass. **b)** The shift of the 2θ reflection position of 16° with respect to doping ratio including the particles prepared in 60 min and 1260 min (24 h).

Higher magnifications, as presented in **Figure 3.14 (e)**, indicate that multipod-like structures are the result of the reunion of rice-like structures. On the other hand, higher magnification over the rice-like shape demonstrate that these structures have fringed edges (**Figure 3.14 (f)**), which may be the ensemble of ~ 10 nm thick nanowires.

Figure 3.15 shows several low magnification high angle annular dark field (HAADF) STEM micrographs and a bright field TEM micrograph revealing that the sample consists of agglomerated nanoparticles. The clusters formed by the sub-10 nm nanoparticles have sizes between 50 nm to a few microns. It is possible to visualize the individual nanoparticles in the lower left HAADF STEM micrograph where the building blocks of these agglomerates seem to have sizes smaller than 5 nm.

To understand the effect of dopant ratio, $\text{Y}(\text{OH})_3:\text{Eu}^{3+}$ phosphors were synthesized for 60 min at various dopant ratios. XRD pattern of the samples is presented in **Figure 3.16 (a)**. All samples employed from 2.5% to 20% doping ratio were indexed with the same crystal

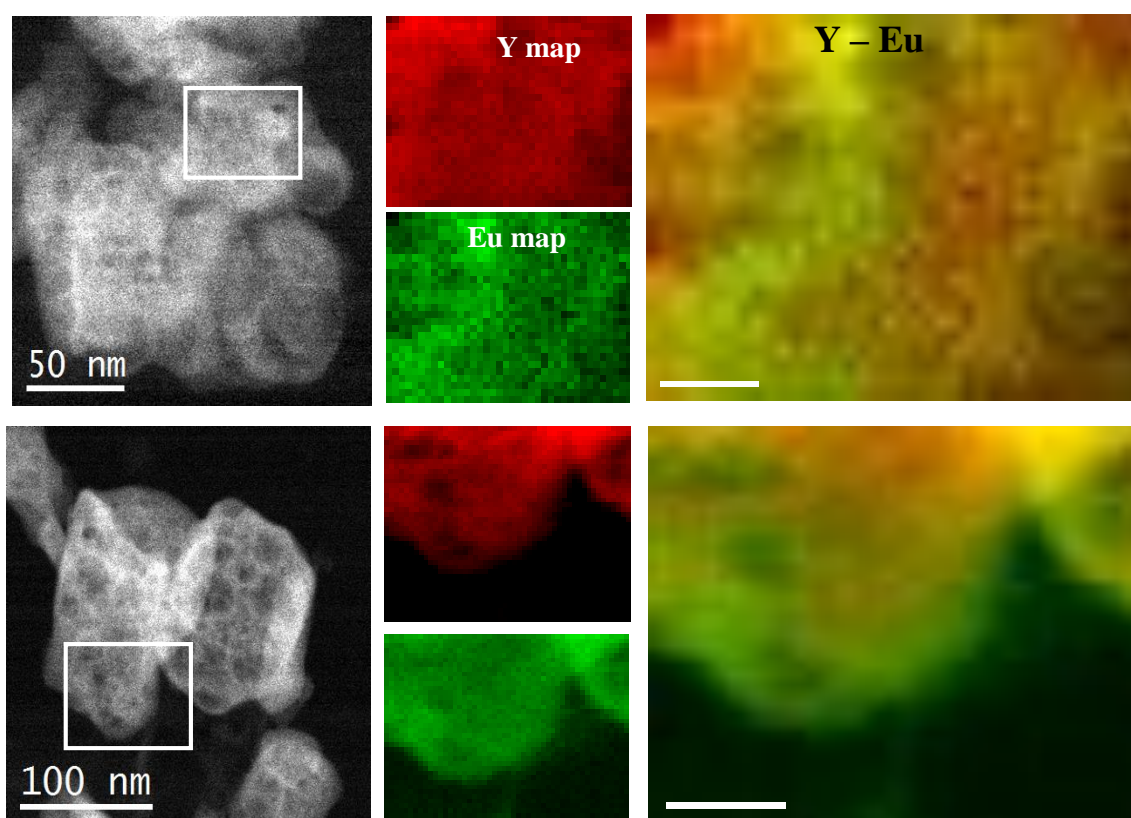


Figure 3.17. Annular dark field (ADF) STEM micrograph of an agglomerate of nanoparticles. STEM-EELS elemental composition maps of the area indicated with a white rectangle: Y (in red) and Eu (in green) maps along with their composite image.

structure previously reported in **Figure 3.12**. Since atomic size of Y and Eu are different, the highest reflection at 16° (2θ) corresponding to (100) plane was examined whether any shift is present for the samples of all doping ratios.

The signals are fitted with a Gaussian distribution, and their exact location was plotted individually against doping ratio in **Figure 3.16 (b)**. The crystals prepared in 1 h and 24 h were studied, and peak position against their doping ratios is given. As the doping ratio increases, a clear shift of the reflections is observed for the both samples. This shift may be the result of enlarging lattice of host crystal due to doping of Eu^{3+} ions. The shift is more evident in the case of phosphors prepared in 24 h, which may imply that extending reaction time, more Eu^{3+} replaced with Y ions as substitutional defect leading to increase in the lattice constant.

Figure 3.17 shows an ADF STEM micrograph and STEM-EELS analyses of the indicated area. Elemental composition maps of Y (red) and Eu (green) along with their composites are shown. (Experimental note: The above presented maps are obtained from the Eu M_{5,4} edges located at 1131 eV and 1161 eV and Y L_{3,2} edges located 2080 eV and 2155 eV. The limitation of the previous EELS maps does not apply here as we could get a spectrum image by using a 1 eV/channel.) As can be seen in the composite map, Y and Eu are distributed quite homogeneously throughout the nanoparticles with some presence of slightly Eu rich or Y rich regions.

3.3.3.1 Growth Mechanism of $\text{Y}(\text{OH})_3:\text{Eu}^{3+}$ Crystals

Growth mechanism of the resulting $\text{Y}(\text{OH})_3:\text{Eu}^{3+}$ crystals was investigated already through considering both SEM and TEM images above. The growth mechanism that

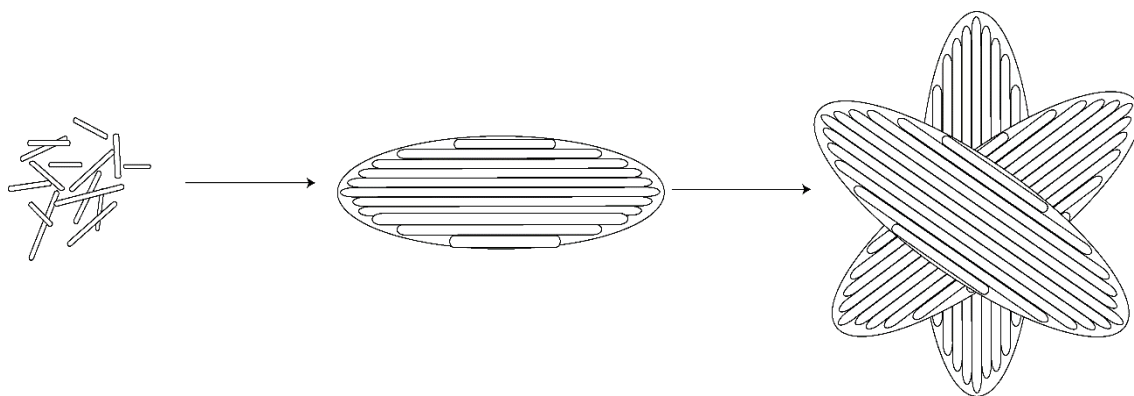


Figure 3.18. Schematic demonstration of the crystal growth mechanism for the development of multipod-like structure of the $\text{Y}(\text{OH})_3:\text{Eu}^{3+}$ phosphors.

governs almost the entire nucleation and crystal growth process here was reported already by Hussain et al. (Hussain et al. 2015) in detail, where the authors employed hexamethylenetetramine (HMTA) during the fabrication of $\text{La}(\text{OH})_3:\text{Eu}^{3+}$ crystals. HMTA degrades into ammonia that acts as hydroxide source. In this study, HMTA was replaced with LiOH, and $\text{Y}(\text{OH})_3:\text{Eu}^{3+}$ crystals were obtained through the interaction of OH^- ions released from LiOH with Y^{3+} ions from the yttrium source in water at room temperature. Even at 5 min, $\text{Y}(\text{OH})_3:(7.5\% \text{Eu}^{3+})$ crystals were being formed as having needle-like shape. Such a fast formation of crystals may hint about the fast nucleation, and here, similar to the idea proposed by Hussain et al. (Hussain et al. 2015) (where the authors argued that the excessive NH_4^+ ions may accelerate the reaction between La^{3+} and OH^-), excessive Li^+ ions in the reaction media may be responsible for this rapid growth. Extending reaction time to 15 min, crystals grow into larger structures and rod-like structure appears in the form of nano-rod bundles probably due to crystal splitting. For 60 min of reaction time, rod-like structures transform into rice-like shapes that are in contact mainly with each other as a part of self-assembly process occurring as a result of saturated splitting process (Hussain et al. 2015). Moreover, multipod-like (or flower-like) morphology was also observed for some particular crystals, which are probably the result of this self-assembly process that finds itself more time to act on these particular crystals. The crystal growth mechanism is summarized and illustrated in **Figure 3.18**. Compared to HMTA, which decomposes into ammonia and releases OH^- ions slowly, LiOH is able to give OH^- ions through complete dissociation directly to the reaction medium. Since the rate of hydroxide release is a strong parameter to control size and size distribution and defect content of the resulting crystal, it is expected to obtain variation for these values in the case of comparing the effect of HMTA and LiOH on the crystal growth. Moreover, such a difference between HMTA and LiOH in terms of the rate of OH^- release may allow the formation of these crystals even at room temperature as reported in this study, while the authors that used HMTA were kept the reaction mixture at 75 °C. On the other hand, crystal growth splitting, as observed for various material systems such as SrTiO_3 (Toshima et al. 2008), Zn_2GeO_4 (Liu et al. 2012), $\text{La}(\text{OH})_3:\text{Eu}^{3+}$ and $\text{La}_2\text{O}_3:\text{Eu}^{3+}$ (Hussain et al. 2015) in literature, is associated with fast crystal growth. A possible cause could be the oversaturation of reactant species. When the concentration of reactive species appears to be higher than a threshold that may vary to each material depending on its chemistry, fast growth of the crystal takes place. This growth may force a high density of crystal defects, i.e. the atoms do not have enough time for the placement in crystal array and

metal atom misplacement may occur during the fast growth. These defects gradually develop nuclei sites developing branches, leading eventually to splitting.

Figure 3.19 (a) presents the PL spectra of the $\text{Y}(\text{OH})_3:\text{Eu}^{3+}$ red phosphors having various dopant ratios. Characteristic signals of the corresponding transition states of the Eu^{3+} are

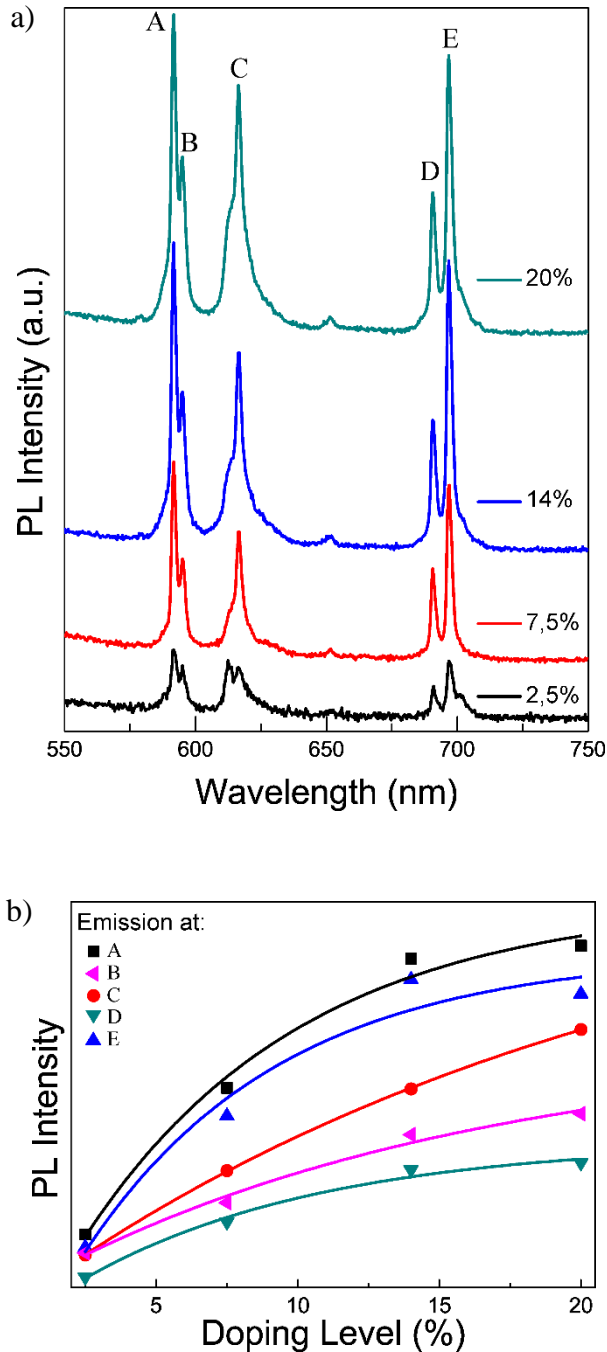


Figure 3.19. **a)** PL spectrum of the $\text{Y}(\text{OH})_3:\text{Eu}^{3+}$ phosphors with different doping ratios, and **b)** variation of their corresponding emission peak intensities, labeled with A, B, C, D, and E, with respect to doping ratio.

labeled with A, B, C, D and E to be able to track their changes with respect to adjusted dopant ratios, which was reported in **Figure 3.19 (b)**. Initially, at the doping ratio of 2.5%, these signals are comparable with each other in terms of their PL intensity. However, with the increasing doping ratio, all emission peaks, especially the signals corresponding to A, C, and E show significant increase. This emission intensity change depending on the doping ratio was reported already in **Figure 3.19 (b)**. The increase of the emission peaks of A, C, and E follow paths those grow faster than the remaining B and D. In any case, these paths are saturating with respect to doping ratio, which is expected since the possibility of having substitutional defect for Eu ions to replace with Y have limitation. This limit can be inferred from the **Figure 3.19 (b)** as 25-30%.

3.3.3.2 White Light Application of $\text{Y(OH)}_3\text{:Eu}^{3+}$

The effect of as prepared $\text{Y(OH)}_3\text{:Eu}^{3+}$ submicron particles as red phosphor on the optical features of YAG-based white LEDs was investigated. Both yellow YAG:Ce^{3+} phosphor and the $\text{Y(OH)}_3\text{:Eu}^{3+}$ submicron particles were mixed with varying ratios in mass (the amount of YAG:Ce^{3+} is fixed) in PDMS matrix (composing of silicon elastomer and curing agent with 10:1 ratio). Optical properties (PL, CRI, CCT, LER, and Lumen) of the PDMS composites are presented in **Figure 3.20**. PL spectrum of the composites including either solely YAG:Ce^{3+} or the mixture of YAG:Ce^{3+} and $\text{Y(OH)}_3\text{:Eu}^{3+}$ particles at various ratios by mass was registered (**Figure 3.20(a)**). In the case of the composite prepared by solely YAG:Ce^{3+} shows a broad range emission having a peak at 550 nm. There are two unidentified sharp emission signals; one at 550 nm appearing on the characteristic emission signal of the YAG:Ce^{3+} and another at 610 nm. With the integration of red phosphor into the PDMS/ YAG:Ce^{3+} system, characteristic signals of the phosphor appear. The signals are designated as A, B, C, D, and E in **Figure 3.19**. When the amount of red phosphor increases, the intensity of these signals increases.

Figure 3.20(b) presents CRI and CCT of the PDMS composites as a function of the amount of red phosphor. While CRI remains almost unchanged, CCT shows a remarkable decrease from 3900 K to 3600 K. The main reason of this inadequate CRI results for this system may be the lack of blue color. On the other hand, a significant improvement value from 281 to 348 lm/W (nearly 24% increase) is observed for luminous efficiencies (LER) as the red phosphor is employed (**Figure 3.20(c)**). Meanwhile, lumens remain almost fixed as the red phosphor amount increases. According to color coordinates as presented

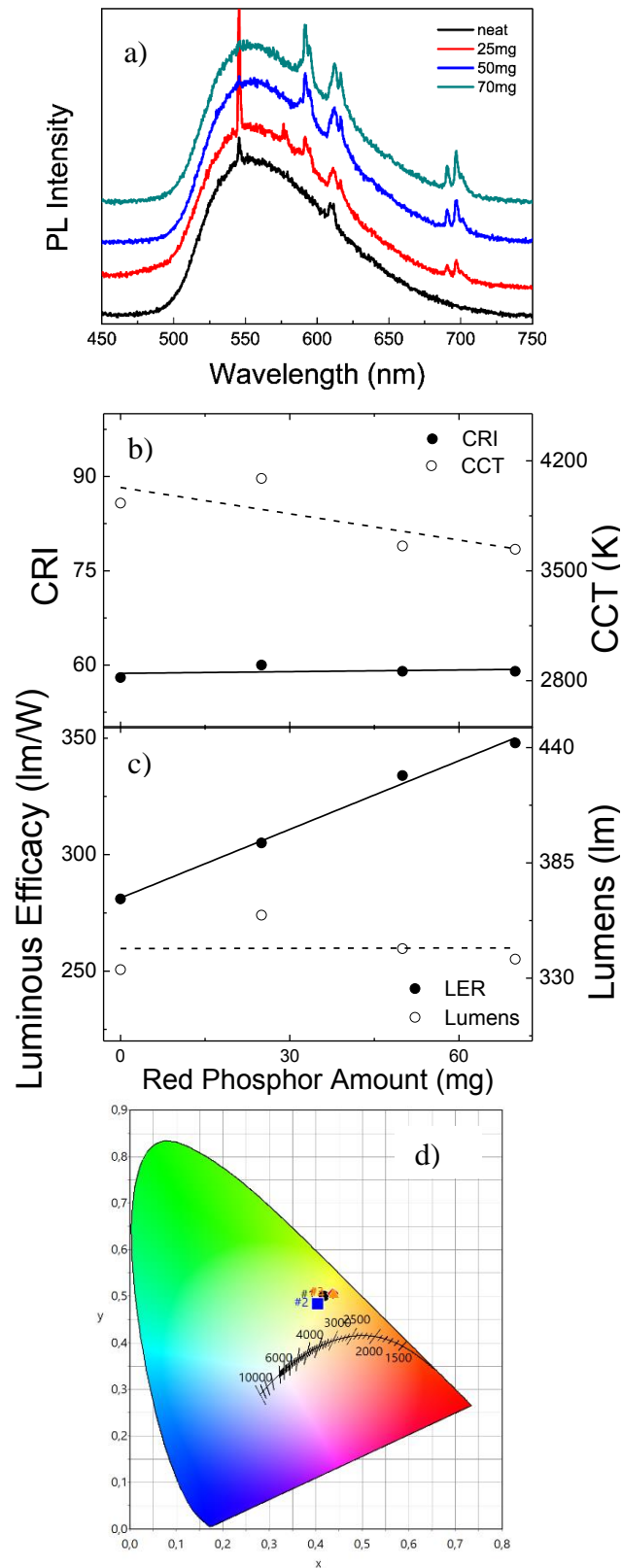


Figure 3.20. WLED application of different amount of red $Y(OH)_3:Eu^{3+}$ phosphors combined with $YAG:Ce^{3+}$ phosphor and their corresponding CRI, CCT, LER and Lumen values.

in **Figure 3.20(d)**, all PDMS composites seem to be accumulated in yellow region. They are far from the white and require blue color to be able to shift resulting color towards white.

3.3.4 Conclusion

In this work, synthesizing $Y(OH)_3:Eu^{3+}$ crystals under room temperature was done and by looking the ADF STEM, it is understood that doping is also achieved at that temperature. Prepared crystals were synthesized without using any toxic surfactants and reaction matrix was water, so it is clearly said that $Y(OH)_3:Eu^{3+}$ crystals are environmental friendly. With the method that is used in this work, new view of synthesizing inorganic optic crystals can be thought.

CHAPTER 4

WLED USING ORGANIC ONE: FIBERS CONTAINNING PERYLENE DYES

4.1 Perylene-Embedded Electrospun PS Fibers for White Light Generation

Apart from the use of inorganic materials such as phosphors, organic dyes can also be employed as color conversion layers in phosphor-converted white LED configurations to produce white light.(Caruso et al. 2012, Mosca et al. 2013, Guner et al. 2019) Among those, perylene diimides (PDI) and their derivatives, are materials that can be used in photovoltaic devices, sensors, LEDs, and field effect transistors due to their strong visible range absorption, high PL quantum yield, high photostability and thermal durability (Oner, Varlikli, and Icli 2011, Kozma, Mróz, and Galeotti 2015, Li and Wonneberger 2012, Huang 2010, Liang, Sun, et al. 2016, Liu et al. 2017, Chen et al. 2015, Fan et al. 2016, Caruso et al. 2012, Zafer et al. 2005, Jiang et al. 2014, Li, Liu, et al. 2016, Mosca et al. 2013). These dyes are cheaper than the inorganic phosphors such as YAG:Ce³⁺, not toxic, not hazardous to human health, and more abundant than the inorganic phosphors since they contain rare-earth dopants, which are constrained by the existing reservoirs.

Electrospinning is a facile technique to produce polymer fibers. It requires high potential difference between a polymer droplet and a collector to form jet. In this sense, either polymer or polymer/solvent system must be determined carefully to allow fiber formation. Otherwise, any polymer/solvent system that not able to respond to the produced electric field cannot form jet, and therefore, no any fibers can be formed over the collector. To date, various neat polymer/solvent systems were reported as being employed to obtain fibers successfully either having μm or nm in size (Demir et al. 2002). Fibers, due to their high surface area, can be employed in LED based white light applications since they are able to scatter light intensively by increasing the optical path length of the LED.

In this chapter, green, yellow and red emitting perylene derivatives were associated with polystyrene (PS) fibers. The prepared perylene containing fibers were combined together into a single poly(dimethyl siloxane) (PDMS) film as frequency conversion layer and applied on a blue LED to obtain tri-chromatic white light source. As a result, high CRI, low CCT color and stable conversion layers were achieved over a blue LED chip. This method of organic dye embedded fibers presents an alternative to phosphor based color conversion layers.

4.1.1 Materials and Methods

Synthesis conditions of the red, green, and yellow perylene diimides that were used in this study are presented in detail in the thesis of Erkan Aksoy. Nevertheless, to avoid from confusion, structure of these dyes and their corresponding absorption and emission spectrum were presented in **Figure 4.1**. Polydimethylsiloxane (PDMS, Sylgard-184, Dow Corning), toluene (Tol., $\geq 99.9\%$, Sigma-Aldrich), tetrahydrofuran (THF, VWR, $\geq 99.7\%$), and polystyrene (PS, Sigma-Aldrich) were purchased and used as received without any further purification.

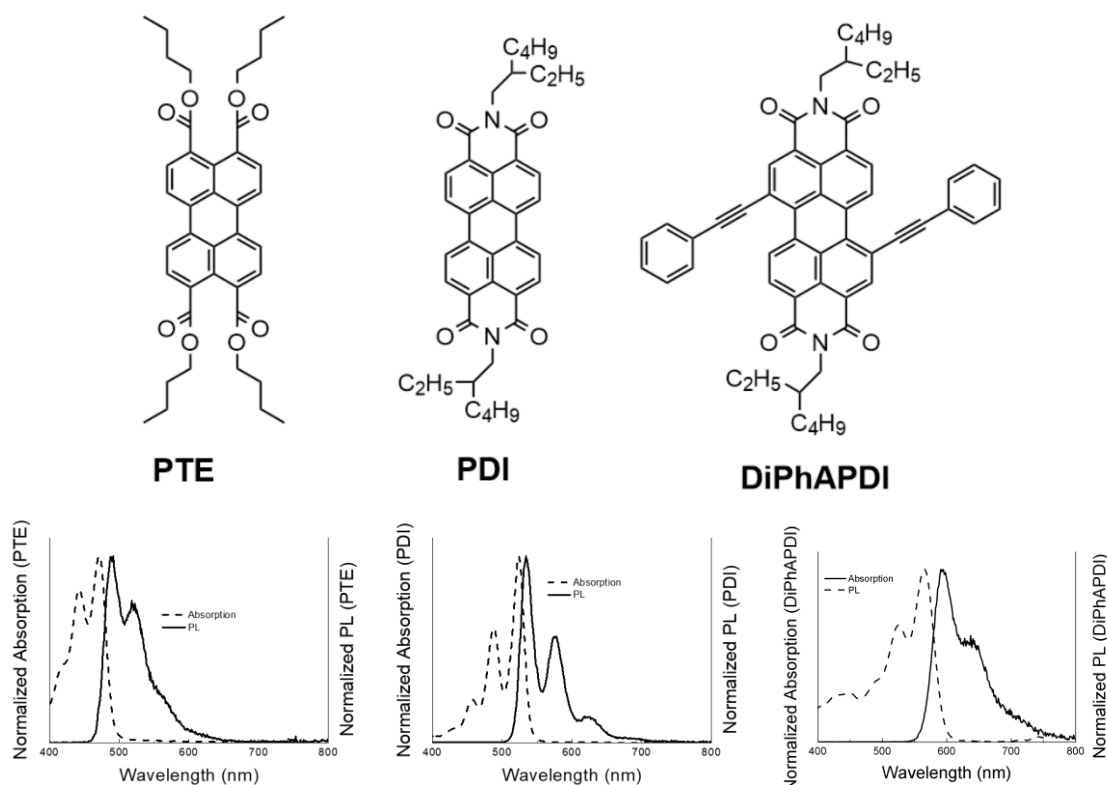


Figure 4.1. Structure and Absorption-PL of the yellow, green, and red perylene diimides

4.1.2 Preparation of Organic Dye-Embedded PS Fibers

PS solution was prepared as 40% w/v in equal volume of Tol. and THF. Then, 1 mL from this PS solution and 0.3 mL from the organic dye/THF (0.2 mg/mL) were mixed in a glass vial. Electrospinning technique was used to prepare organic dye embedded fibers. Therefore, to prepare fibers, the resulting composite was loaded into a syringe and placed on a syringe pump. The parameters for electrospinning were fixed at 18 kV for voltage and $0.7 \text{ mL}\cdot\text{h}^{-1}$ for the flow rate. Due to the potential difference between the tip of syringe and the aluminum foil collector, PS/organic dye jets were formed and lead to production PS/organic dye fibers over the aluminum foil. Fibers that were formed in a nonwoven shape over aluminum foil collector were collected. The starting PS:dye solution is drop-casted and dried under room conditions for comparison.

4.1.3 Preparation of PDMS/Organic Dye Embedded PS Fiber Composites

To obtain PDMS/organic dye embedded PS fiber composite free-standing film, collected PS fibers were put in a mold. Then, total amount of 1g PDMS, with a ratio of 1:10 for curing agent:oligomer, was cast onto the fiber mats in the mold to cover all fiber surfaces. Mold was put into a vacuum oven at room temperature for 1h and then cured at 100° for 15 min. Finally, freestanding PDMS film containing organic dye embedded fiber was extracted from the mold. The entire process is summarized in **Figure 4.2**.

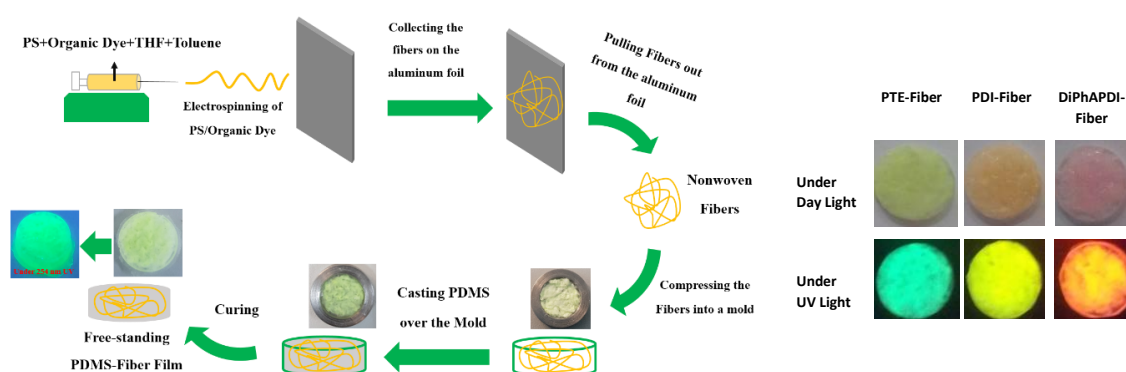


Figure 4.2. Summary of electrospinning path followed for PTE, PDI and DiPhAPDI and visualization of their freestanding PDMS films under daylight and UV illumination.

4.1.4 WLED studies

For WLED application, two different preparation methods were used. In the first case, all PS/organic dye fibers were stacked individually with specific amounts and compressed as whole in the mold (**Figure 4.3**) and labeled as WLED. A single free-standing PDMS/organic dye embedded PS fibers composite film was obtained after casting and curing the PDMS over stacked fibers.

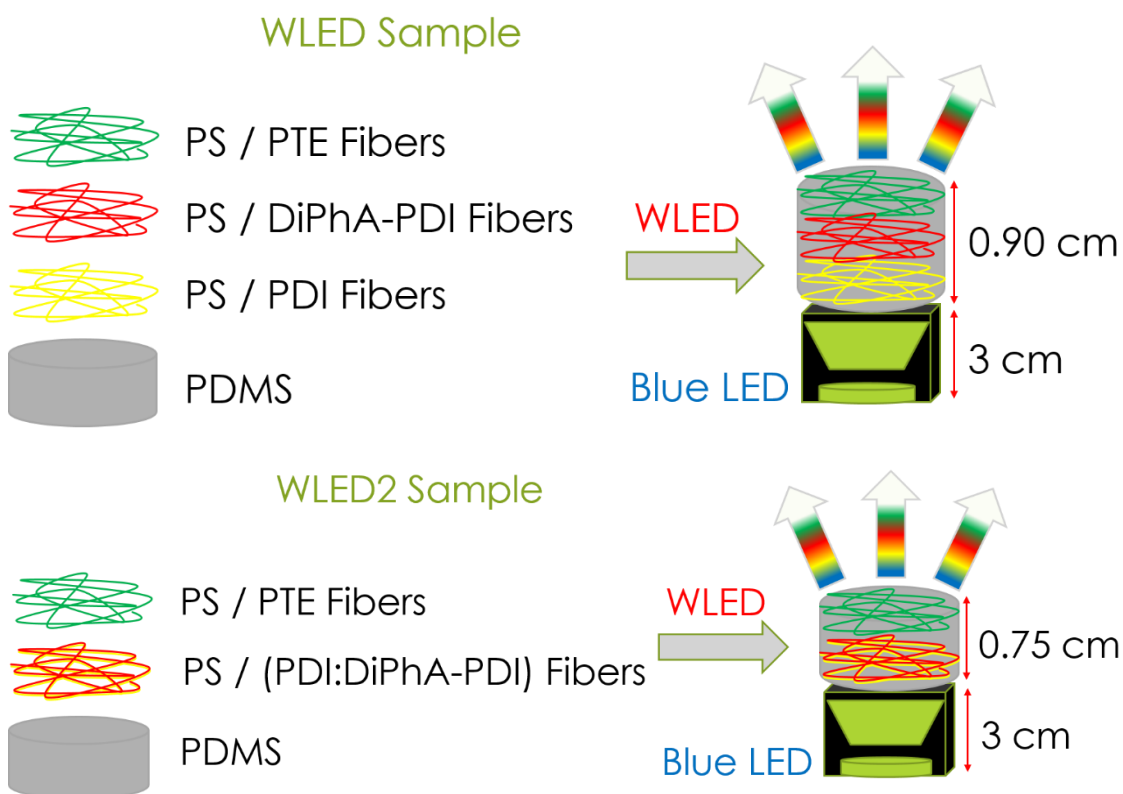


Figure 4.3. Visualization of the WLED samples prepared with different processing methods: either by stacking individual fibers or stacking PDI:DiPhAPDI and PTE fibers separately

In the second strategy, which is labeled as WLED 2, PDI and DiPhAPDI solutions (0.2 mg/ml) were mixed in a glass vial that contain 1mL from the PS solution (40% w/v in equal volume of THF:Tol.) with an equal volume (1:1 v/v ratio). To keep the organic dye/PS ratio, total volume of the PDI and DiPhAPDI mixture was fixed to 0.3 mL.

Electrospun fibers that contain equal volume of PDI and DiPhAPDI organic dyes were obtained after electrospinning. These fibers and the already prepared PTE fibers were

then stacked in the mold individually with various amounts and free-standing PDMS/organic dye embedded PS fiber composite films were prepared (**Figure 4.3**).

4.1.5 Results and Discussion

Figure 4.4 presents the morphology of the resulting PS:dye fibers. Overall distribution of the composite fibers (**Figure 4.4 (a)**), indicates that fibers are formed individually having size of 4-6 μm . Interestingly; most of these individual fibers appear as they were the result of merged two single fibers. Moreover, applying higher magnification to these fibers demonstrates that these fibers possess porosity with 50-100 nm in diameter on their surface (**Figure 4.4 (b)**). Compared to fibers having smooth surface, porosity may improve the optical path length of the incoming blue light and may enhance the PL of organic dye.

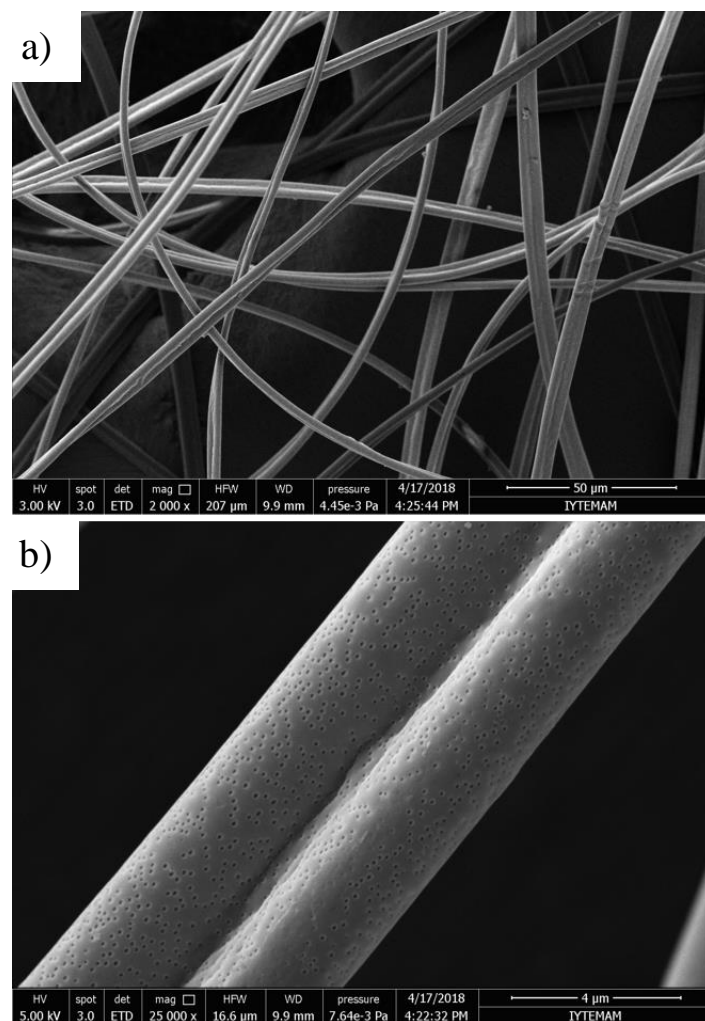


Figure 4.4. The morphology of PS/organic dye composite fibers.

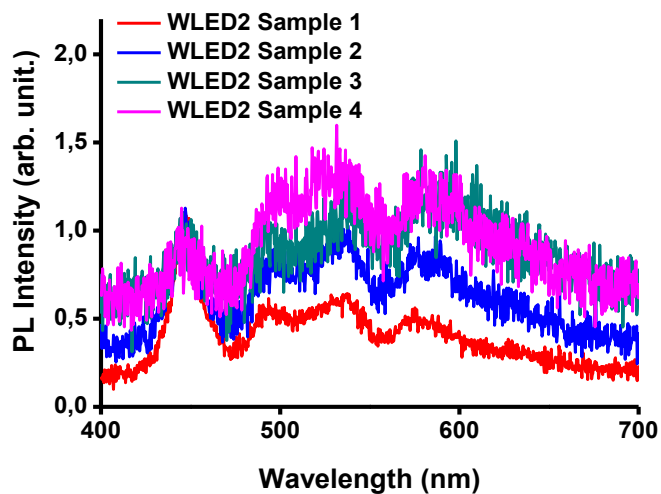
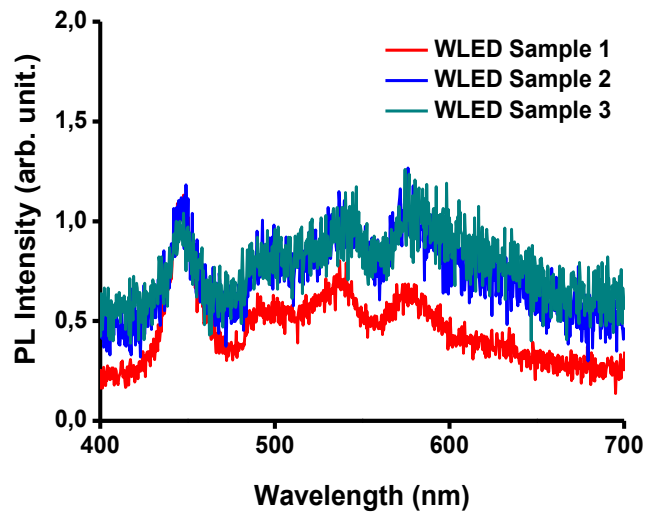
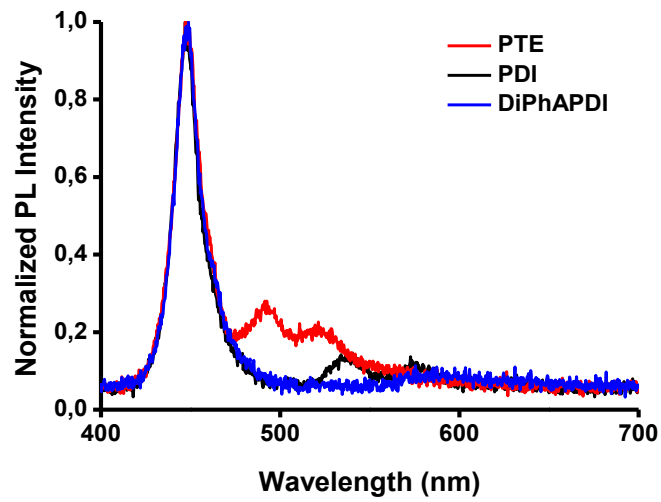


Figure 4.5. PL spectrum of individual PDMS/organic dye electrospun fiber composites and their various formation strategies including WLED and WLED 2 (driving current=20 mA)

Furthermore, compared to drop-casting of the PS/organic dye solution over a glass surface, which produces a single PS/organic dye film having particular optical features, one can obtain many fibers (approximately 60mg with the electrospinning setup used in this study) with the same solution by using electrospinning technique. These fibers can be employed in white light applications with different amounts in mass for a single sample to tune the optical features such CCT and luminous efficiency of the produced frequency conversion layers. Moreover, one can prepare more than one sample, even 2, 3 or 4 samples, by keeping the amount of these fibers fixed. For instance, one can produce three samples from WLED sample 3 or 2 from the WLED 2 sample 2 where they show highly satisfying optical features that will be presented and discussed below in detail.

Table 4.1 Fiber masses and optical properties of the related samples used in WLED strategy under 20mA of driving current

Sample #	PDI Fiber Mass (mg)	DiPhAPDI Fiber Mass (mg)	PTE Fiber Mass (mg)	CRI	CCT (K)	Power efficiency (lm/W)
1	15	10	10	86	6679	222
2	20	15	10	89	5205	212
3	20	20	10	92	4918	197

Prepared organic dye embedded PS fibers with different colors, PDI as yellow, PTE as green, and DiPhAPDI as red, were put into a form of color conversion layer by casting PDMS over these fibers in the mold. PDMS / PDI, PTE, and DiPhAPDI composite fibers were put onto a 455 nm blue LED under driving current of 20 mA separately first. Top figure of **Figure 4.5** presents the resulting spectrum of these samples. Obviously, PDI and PTE show explicit emission under blue LED and maintain their individual characteristic PL peaks. On the other hand, red emission of the DiPhAPDI sample is not efficient in terms of PL intensity as others, but still can contribute as red color to overall system. Middle figure of the **Figure 4.5** presents PL spectrum of the WLED samples with varying individual fiber masses. Note that stacking sequence of these individual organic dye fibers, corresponding to PTE, PDI and DiPhAPDI dyes separately, was determined by considering their absorption and quantum yield features. In the case of preparing conversion layers with stacking formation, such as stacking red and yellow phosphors, the mainstream design is to sort these individual conversion layers from lowest band-gap

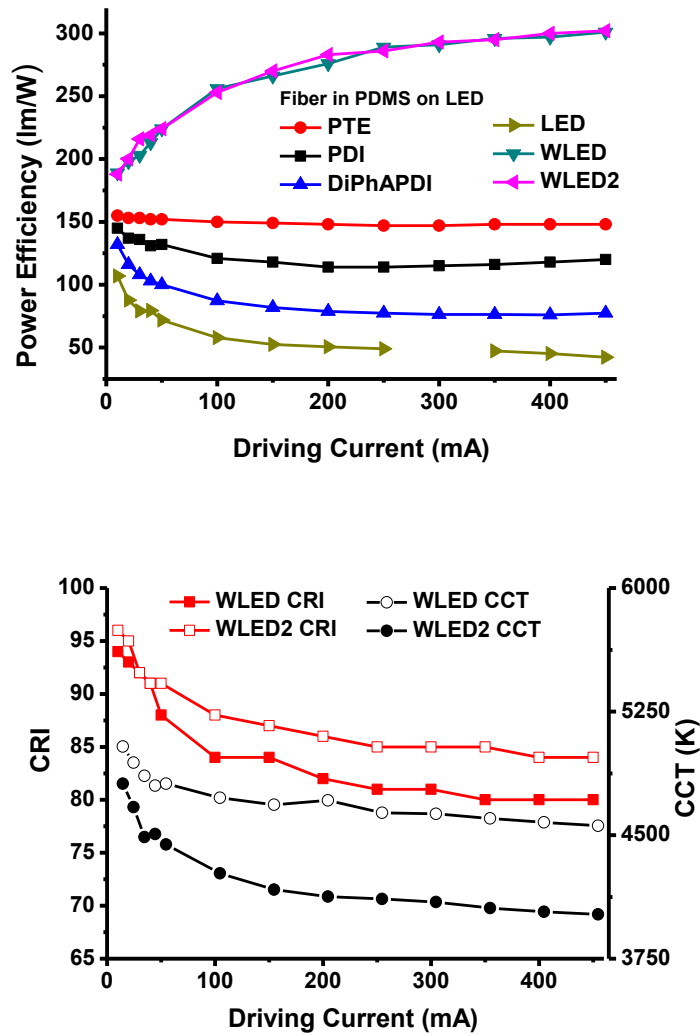


Figure 4.6. Change of optical properties, power efficiency, CRI and CCT under various driving currents

to highest above LED to avoid from internal absorptions. Therefore, DiPhAPDI, PDI and PTE fibers are expected to be stacked over blue LED in this order. However, even though PTE fibers are still the farthest from the LED, locations of DiPhAPDI and PDI are replaced to increase PL intensity of DiPhAPDI fibers based on internal absorption such as its additional absorption from PDI. It is observed from their spectrum that the individual characteristic peaks of the organic dyes are still preserved even after their stacking formation and PDMS coating for all samples. In terms of optical features, all samples were achieved to show CRI greater than 85 (**Table 4.1**). From Sample 1 to Sample 3, as the total fiber mass increases, CCT started to reduce from 6679K to 4918K while CRI shows a clear increment from 86 to 92, which is based on the improved red-

Table 4.2 Fiber masses and optical properties of the related samples used in WLED2 strategy under 20mA of driving current

Sample #	PDI:DiPhAPDI Fiber Mass (mg)	PTE Fiber Mass (mg)	CRI	CCT (K)	Power efficiency (lm/W)
1	22	6	89	7490	219
2	30	10	89	5677	220
3	40	10	94	4646	199
4	35	15	90	5102	211

emission due to increasing amount of DiPhAPDI fiber. Therefore, with the adjustment of fiber content, one can achieve both improvement for CRI and tuning for CCT values. However, there is an opposite correlation between total fiber content, CRI and luminous efficiency. With the increasing CRI together with increasing fiber content, luminous efficiencies show a slight decrease. For the second strategy (WLED 2), resulting PL spectrum of WLED 2 samples is given in bottom figure of the **Figure 4.5**. Even though the contribution of red and yellow colors are now coming from a single fiber composition unlike the first strategy where these dyes contribute individually based on their sequential positioning as two different fiber contents, it is observed that the resulting PL still contains the individual characteristic PL peaks of these dyes. Similarly, by varying the amount of fibers in mass, different CRI, which all samples have showed almost $CRI \geq 90$, and adjustable CCT values that are taking values between 7500K and 5000K, are obtained (**Table 4.2**). Meanwhile, luminous efficiency again drops approximately 20 lm/W. One further sample, as WLED 2 sample 4, was produced with using the same total fiber amount in mass with WLED 2 sample 3 to compare the effect of PDI: DiPhAPDI and PTE fiber content ratios. It is clear that even though they have the same total fiber mass in total, by increasing the PTE amount while decreasing the PDI: DiPhAPDI lead to a decrease in CRI and an increase in both CCT and luminous efficiency. Therefore, one can conclude that even though total fiber amount is significant in the fabrication of WLED products containing these PS/organic dye fibers to obtain desired optical features, the ratio of employed fibers in either WLED or WLED 2 strategies can also provide a fine tuning among these optical features.

Figure 4.6 presents the change of optical properties such as power efficiency, CRI, and CCT with respect to driving current. In the first case, there is a clear inverse relationship

between increasing driving current and the power efficiencies of individual PDMS/organic dye fiber composites including PTE, PDI, and DiPhAPDI dyes in the order based on their quantum yields from highest to lowest. Comparing these samples with bare LED output, which shows a dramatic decrease with the increasing driving current, reveals that even though these samples have decreasing profile for power efficiencies, are still less than the bare LED output. Among those samples, PDMS/ PTE fiber composite remains almost stable. On the other hand, WLED and WLED 2 samples, which were selected among the ones with highest CRI; Sample 3 of both strategies, indicate dramatic increase with the increasing driving current. They follow almost the same path together, and reach even 300 lm/W of power efficiency at higher driving current values. Further investigation was performed for these WLED and WLED 2 samples in terms of their CRI and CCT values. Obviously, as the driving current increases, CRI and CCT values of the both samples decrease. In the case of CRI, among the decaying profiles of these samples, WLED 2 has the lowest decaying rate. However, in the case of CCT, WLED 2 decays faster than the WLED unlike the previous case, providing a broader tunability range for the CCT values. Therefore, WLED 2 can be offered as a better strategy than the WLED since its CRI values drop less with the increasing driving current while CCT values showing a broader range of adjustment.

Another essential parameter that determines whether these samples can be commercialized or not, is their optical stability against continuous illumination of blue LED under 20mA driving current. In this sense, periodic measurements in time have been done on both the same WLED and WLED 2 samples that were used already in previous case. It is observed that even though there is a fluctuation for the values of power efficiencies of both WLED and WLED 2 samples, both dataset can be fitted to a linearly straight curve showing a clear stability in time, for 240 min (**Figure 4.7**). These samples have almost the same fitting curve that implies both samples show the same stability performance in terms of their power efficiencies against continuous illumination. On the other hand, CRI and CCT values of both samples were observed to follow a linear straight curve also in time similar to previous case. The main difference between these two samples is their different CRI and CCT values that is the reason of the shift observed for both y-axis unlike the power efficiencies where they were started from almost the same point in their y-axis. However, even though these straight stability curves have different

starting points, they indicate an obvious stability with respect to changing time, for 240 min.

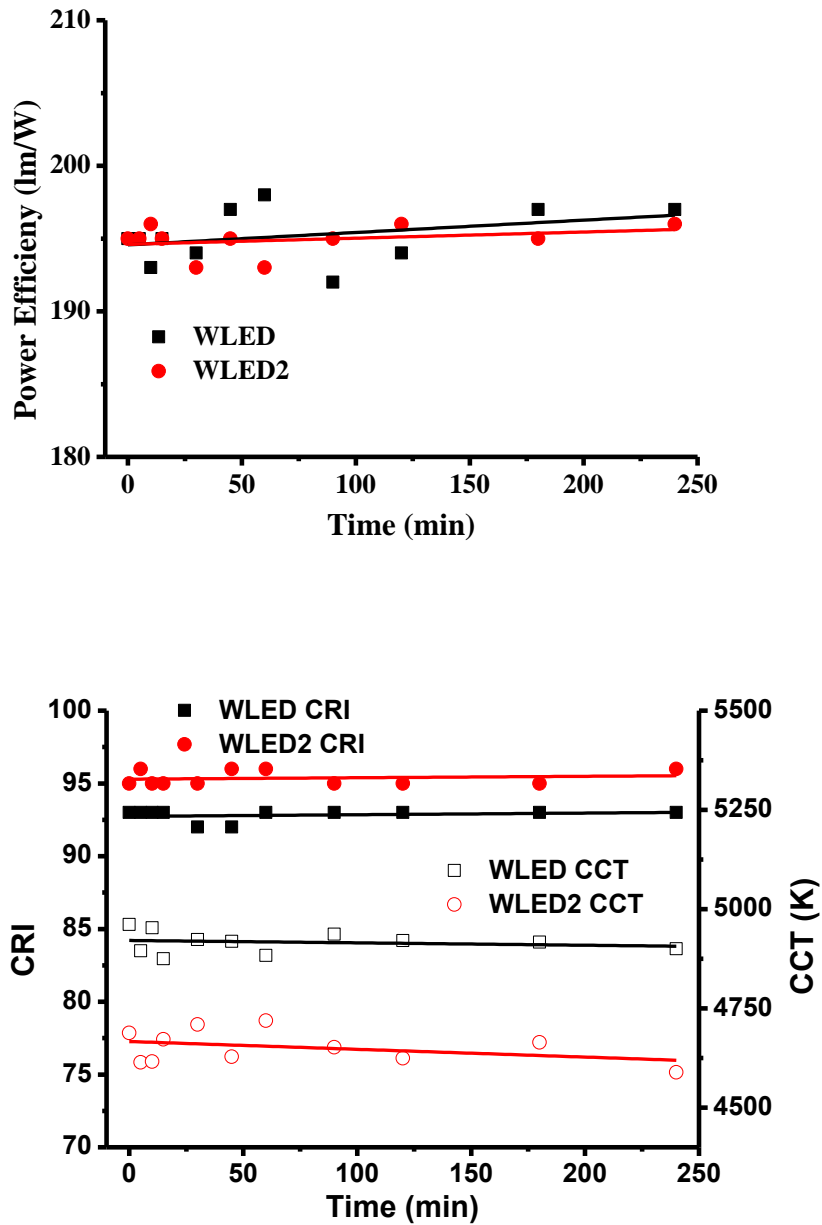


Figure 4.7. Change of power efficiency, CRI and CCT under continuous illumination of blue LED (driving current=20 mA).

Therefore, it can be concluded that both WLED and WLED 2 samples were found as optically stable under continuous LED illumination having 20mA driving current. In this sense, these materials, polymer/organic dye composite fibers, can be a promising

alternative to inorganic phosphors as frequency conversion layer to be used in lighting industry in future.

4.1.6 Conclusion

A fabrication method of organic dye based frequency conversion layers to be used in WLED applications is offered. To the best of our knowledge, fabricated samples showed the highest CRI and power efficiency values in literature that the perylene dyes were used as down conversion materials and adjustable CCT depending on the used fiber amount in mass. Moreover, applying various driving currents and exposing these samples to continuous illumination of blue LED reveal that these samples have performed well enough, where they are found to follow a growing curve for power efficiencies with increasing driving current and found to be stable under continuous illumination for 240 min.

CHAPTER 5

Future Prospects

5.1 Halide Perovskite-based Applications

Halide perovskites have a unique crystal structure in the form of ABX_3 (A: organic or inorganic cation, B: divalent metal cation, and X: halide anion (Br^- , I^- , Cl^-)). To date, three possible cations for A has been reported, which are able to stabilize the perovskite structure; MA, FA, and Cs^+ .(Stoumpos and Kanatzidis 2015) Goldschmidt's Tolerance Factor,(Goldschmidt 1926) $t = (r_A + r_X)/\sqrt{2(r_B + r_X)}$, where r_A , r_B , and r_X are respective ions in the ABX_3 formula, hint about the formation of well-defined perovskite structure.(Saparov and Mitzi 2016) For instance, the majority of the 3-D perovskites were found (empirically) satisfying $0.8 \leq t \leq 1.0$. Depending on the type of cation, halide perovskites can be divided into two groups. If the cation A of the perovskite involves either MA or FA or both, the structure falls into the group of organometallic halide. On the other hand, if Cs^+ is employed, the structure is considered to be the all-inorganic halide perovskites. All-inorganic lead halide perovskites ($CsPbX_3$) have been known since 1890s.(Wells 1893) However, it had taken six decades to report the semi-conductive nature of these materials.(MØLLER 1958) Organometallic halide perovskites ($MAPbX_3$ or $FAPbX_3$), by contrast, have been introduced at late 1970s and known for almost 40 years.(Weber 1978)

First known applications of these halide perovskites were performed with using organic cations. These materials were found to show significant optical features; small exciton binding energies, high charge carrier mobilities, strong light absorption, etc.,(Mitzi 1999, Bai, Yuan, and Gao 2016, Lin et al. 2015) and lead to the discovery of the highly efficient photovoltaic (PV) devices of halide perovskites.(Kojima et al. 2009, Green, Ho-Baillie, and Snaith 2014) Since then, these materials involving either organic or inorganic cations, have begun to gain significant attention and these developments bring halide perovskites into the research spotlight recently.(Snaith 2013, Kovalenko, Protesescu, and Bodnarchuk 2017, Correa-Baena et al. 2017) Apart from their use in PV devices, they show more than

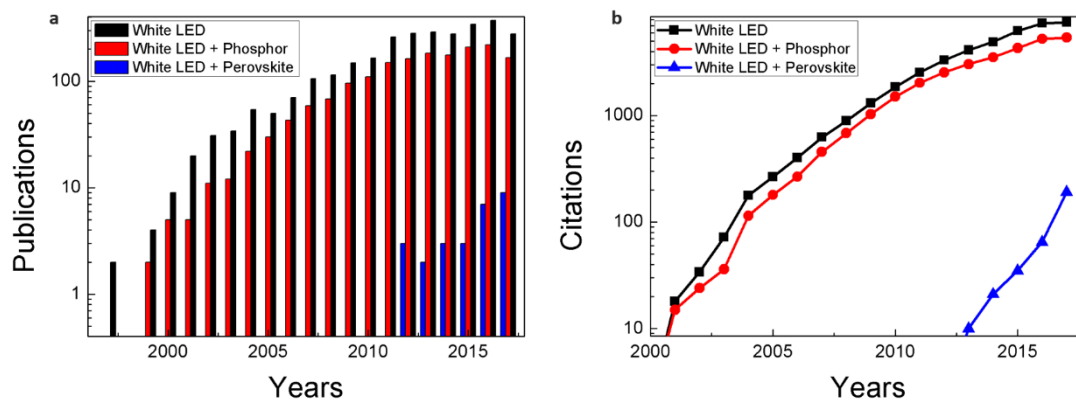


Figure 5.1 Statistical data of **a)** publications, and **b)** citations about the last 20 years.

90% quantum yield in photoluminescence.(Protesescu et al. 2015b, Song, Li, et al. 2015) Moreover, they possess unique properties, such as solution-processability, long carrier lifetimes, ease of fabrication, and wavelength tunability based on anion exchange reactions.(Stoumpos and Kanatzidis 2015) These features make the halide perovskites a strong candidate to be used in optical applications including display technologies, WLEDs, etc.(Bai, Yuan, and Gao 2016, Sutherland and Sargent 2016) Especially in the case of WLED applications, these halide perovskites may i) be used together with YAG phosphor or ii) replace YAG phosphor in YAG-based WLEDs, or iii) be used to obtain three main red-green-blue (RGB) colors separately over UV LED as alternative to UV phosphors. To get further insight in what degree of white LED studies involve phosphor or perovskites, statistical data of total publications and citations released in the last two decades were collected from Web of Science. This data is based on the publications and citations related to keywords White LED, White LED + Phosphor, and White LED + Perovskite, and the statistical results are presented in **Figure 5.1**. It is obvious that white LED publications and citations have grown together with the phosphor publications and citations, and follow closely each other since the beginning of 2000s. However, the publications and citations involving white LED and phosphors started to become stabilized in recent years. This loose of interest in white LED studies may be the result of saturating phosphor studies most probably due to reaching sufficiency in terms of materials discovery and their optimization. On the other hand, perovskite related white LED publications and citations just initialized and grows rapidly since 2012. It will not be surprise if this new era will pass the phosphor related studies in a short time and then will lead to rapid growth for white LED publications and citations.

5.2. Preparation of Halide Perovskite Materials

Metal halide perovskites, in general, contain $[\text{PbX}_6]$ octahedra that are connected in three dimensions. Cations, either organic or inorganic, are located between the large spaces of anionic octahedra sites. Polymorphs of this crystal structure; cubic, tetragonal, and orthorhombic lattice in the bulk form (Kovalenko, Protesescu, and Bodnarchuk 2017) or unequivocally orthorhombic in the case of QDs (Cottingham and Brutchey 2016). (He, Qiu, and Yang 2017) Depending on the type of cation, the band gap of related perovskite crystals varies. For instance, MAPbI_3 has $E_g \sim 1.50 - 1.61 \text{ eV}$, FAPbI_3 has $E_g \sim 1.47 - 1.55 \text{ eV}$, and $\text{CsPbI}_3 \sim 1.67 - 1.73 \text{ eV}$. (Ono, Juarez-Perez, and Qi 2017) It is expected to obtain higher PCE for FAPbI_3 -based solar cells; however, MAPbI_3 -based solar cells reached 18-20% (Son et al. 2016) while FAPbI_3 based ones depicted 13.5 – 18%, (Yang et al. 2015, Lee et al. 2014, Zhou, Yang, et al. 2016) and CsPbI_3 showed PCE only about < 2.9% (Choi et al. 2014, Eperon et al. 2015). In all cases, long-term stability is still a challenge for this technology to become commercialized.

5.2.1 Organometallic Halide Perovskites

Various preparation methods have been developed as targeting novel potential applications particularly to enhance the efficiency of solar cells. Early use of these materials was based on the formation of MAPbX_3 in the presence of mesoporous metal oxides, where the porosity allows the formation of perovskite crystals. (Burschka et al. 2013, Cai et al. 2013, Etgar et al. 2012, Lee et al. 2012, Kojima et al. 2009, Noh et al. 2013) Moreover, the synthesis of these materials can be performed in solution to obtain bulk (Tsai et al. 2016, Liu et al. 2015, Shi et al. 2015) or nano-structured (Schmidt et al. 2014, Vybornyi, Yakunin, and Kovalenko 2016, Protesescu et al. 2016) organometallic perovskites. Solution-based NC synthesis of these materials can be divided into two strategies; i) ligand-assisted re-precipitation; highly polar solvent, such as DMF, is used to dissolve both alkylammonium halide and the lead halide source, then the resulting solution is injected into a poor solvent to trigger NC crystallization. For instance, Zhang et al. (Zhang, Zhong, et al. 2015) dissolved PbBr_2 , MABr , *n*-octylamine, and oleic acid in DMF and then dropped this solution with fixed amount into toluene. With this method, the authors claimed to obtain MAPbBr_3 quantum dots with 3.3 nm size having 50-70% absolute quantum yields. ii) ionic methathesis approach, which involves no polar solvent but various sources of cation including alkyl-amines (similar to using Cs-oleate as Cs^+

source in the case of synthesizing all-inorganic perovskites). As an example, *Vybornyi et al.* (Vybornyi, Yakunin, and Kovalenko 2016) used oleic acid (OA) containing methylamine solution in tetrahydrofuran (THF) to inject into the solution of PbX_2 containing oleylamine (OAm) – OA – ODE mixture. Resulting solution shows fast crystallization occurring in seconds. Following this method, the authors successfully obtained MAPbX_3 ($\text{X} = \text{Br}$ and I) nanocrystals with various morphologies; cube, wire, and platelet.

5.2.2 All-Inorganic Halide Perovskites

Similar to the fabrication of organometallic halide perovskite NCs, all-inorganic perovskite synthesis includes two main methods: hot injection and room-temperature recrystallization. (Li et al. 2017) In the former (**Figure 5.2 (a)**), preheated Cs-oleate was injected as Cs^+ source into solution mixture containing PbX_2 and OA, OAm, and ODE at temperatures varying from 60° to 250° . (Protesescu et al. 2015b, Swarnkar et al. 2016, Zhang, Eaton, et al. 2015) Solution turns into greenish color rapidly (due to bright green emission of forming NCs under daylight), which can be then collected via centrifugation. This method allows controlling the size of the resulting NC via adjusting reaction time, temperature, and precursor concentrations. (Bekenstein et al. 2015) A typical sample having nanocube shape is illustrated by the inset. In the case of room temperature recrystallization (**Figure 5.2(b)**), similar to the organometallic halide synthesis i), CsX and PbX_2 ($\text{X} = \text{Br}^-$, Cl^- , I^-) were dissolved together in a good solvent, DMF can be used as a good solvent in this case too, in the presence of OA and OAm. Then, an aliquot of this solution is dropped into a poor solvent such as toluene, causes a supersaturation leading to fast crystallization due to solubility difference between DMF and toluene. (Li, Wang, et al. 2016, Li, Wu, et al. 2016) Notice that ligands OA and OAm are used during the synthesis of both organometallic and all-inorganic halide perovskites. These ligands can balance the charge between cations and anions, therefore, by varying the chemical properties of these ligands or the ratio of OA/OAm, one can tune the morphology of resulting NCs. (Liang, Zhao, et al. 2016, Hassan et al. 2016, Pan et al. 2016, Shamsi et al. 2016, Li et al. 2017)

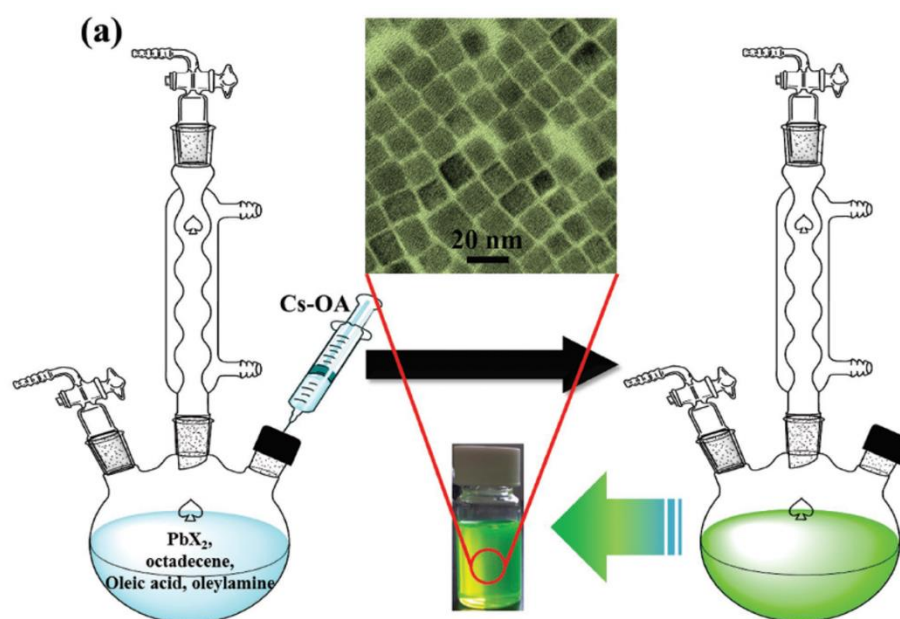


Figure 5.2 Schematic representation of the hot injection method. TEM image of a typical sample is given at inset. Reproduced with permission. Copyright 2017, Wiley-VCH.(Source: Li et al. 2017) **b)** Schematic representation of room-temperature recrystallization. Reproduced with permission. Copyright 2016, Wiley-VCH.(Source: Li, Wu, et al. 2016)

5.3 Optical Characteristics of Halide Perovskite Materials

One of the exceptional features of the halide perovskites is the wavelength tunability, which can be achieved simply via anion-exchange reactions, chemical composition (mixing different cations), and through quantum confinement by adjusting the NC size.

A number of studies have been reported in literature showing the control over spectral features in between 390-1050 nm.(Protesescu et al. 2015b, Zhang, Zhong, et al. 2015, Eperon et al. 2014, Noh et al. 2013, Pellet et al. 2014, Stoumpos, Malliakas, and Kanatzidis 2013, Sadhanala et al. 2014, Hao et al. 2014, Nedelcu et al. 2015, Akkerman et al. 2015) Anion-exchange reactions depend on the halide ions of X (X: Br⁻, Cl⁻, I⁻) that are used in the ABX₃ structure, and show blue shift when Cl⁻ ions were employed where I⁻ shifts the resulting emission toward red. Furthermore, halide perovskite crystals can also be prepared with using more than a single anion, i.e. AB(Cl_xBr_yI_{1-x-y})₃ where the total ratio of these halide anions equals to unity (0 ≤ x, y ≤ 1). Simply by adjusting the ratio of halide anions, full spectrum can be covered from UV to infrared.(Li et al. 2017, Adjokatse, Fang, and Loi 2017, Nedelcu et al. 2015, Proteescu et al. 2015b) **Figure 5.3 (a)** shows the emission of samples with various halide ions (or halide ion ratios) under UV light. Their registered PL and absorption-emission spectra are given in **Figure 5.3 (b-c)**, which obviously verifies the tunability of wavelength depending on the halide ions from UV to infrared. On the other hand, quantum confinement effect, which tells about the effect of particle size on its emission, can be related with

$$E = \frac{\hbar^2 \pi^2}{2r^2 m^*} + (E_g - R_y) \quad (4.1)$$

where r is the radius of the particle, m^* is the reduced carrier mass, E_g is ground state

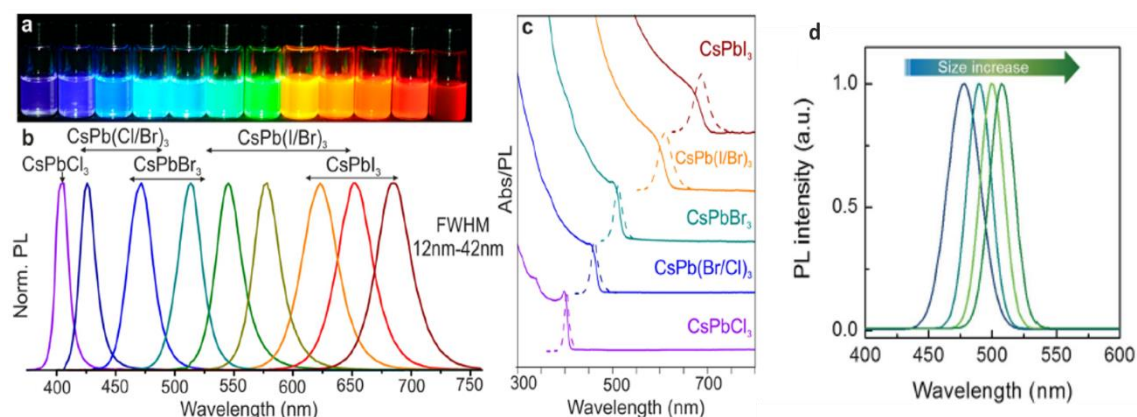


Figure 5.3 **a)** Halide perovskites with various anions (or anion ratio) under UV illumination, **b-c)** collected PL and abs/PL spectra of related samples, respectively. Reproduced with permission. Copyright 2015, American Chemical Society.(Source: Proteescu et al. 2015b) **d)** demonstrates the size effect of perovskite NCs on the wavelength tunability. Reproduced with permission. Copyright 2015, Wiley-VCH.(Source: Song, Li, et al. 2015)

energy, and $R_y = m^*e^4/2\epsilon^2\hbar^2$ is the exciton energy including ϵ as the dielectric constant, can be used for both band-gap engineering and quantum yield improvement. In general, a critical parameter known as Bohr's radius $a = \hbar^2\epsilon^{eff}/m^*e^2$ that is defined through the Eqn. (4.1) is used to understand the degree of confinement for a given particle size. In the case of having particles much larger than a , first term in Eqn. (1) drops and excited state of the particle becomes lower than the ground state (no confinement). However, the confinement appears when the particle size gets smaller than a since E reaches to larger values compared to E_g . In such a case, the system starts to behave like a quantum well that shows sharp distinction between excited states leading to increase for the energy of excited states. This size effect is illustrated in **Figure 5.3(d)**. As the size of perovskite NCs increases, a red shift takes place in the wavelength of almost 50 nm. Moreover, *Huang et al.* (Huang et al. 2015) reported that during the synthesis of MAPbBr₃ NCs via recrystallization, they achieved to obtain size-tunable band-gap by just adjusting the temperature of the poor solvent. The authors claimed tuning the emissions in the range between 475-520 nm. Moreover, high quantum yields from 74% to 94% were obtained following this method. Size-tunable band-gap can be achieved in the case of all-inorganic halide perovskites. For instance, *Protesescu et al.* (Protesescu et al. 2015b) demonstrated that CsPbBr₃ NCs were synthesized with particle diameters ranging from 4 to 12 nm that able to cover the spectral region of 410 – 700 nm with high quantum yields of 50-90%. The authors calculated the Bohr radius of CsPbX₃ halide perovskites, and found that it is 5 nm for Cl⁻, 7 nm for Br⁻ and, 12 nm for I⁻, which are obviously comparable in size with

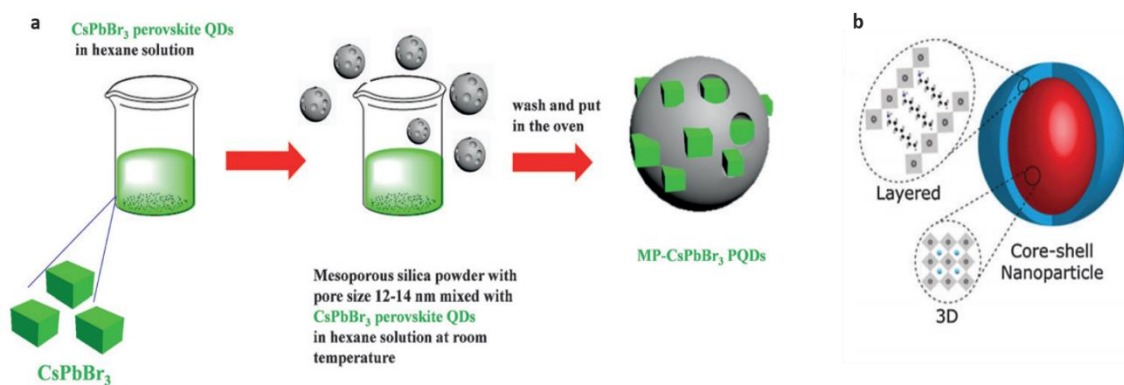


Figure 5.4 Different halide perovskite stabilization methods; **a)** mixing with mesoporous silica (Source: Wang et al. 2016), and **b)** growing shell of wider band-gap over halide perovskite NCs. (Source: Bhaumik et al. 2016)

the perovskite crystals that they had synthesized. Recently, doping in perovskite crystals, particularly with Mn^{2+} ions started to become a new and active research era, which can serve as an alternative strategy for wavelength tuning in halide perovskites. (Guria et al. 2017, Pradhan et al. 2017, Liu et al. 2016, Zhu et al. 2017) In such a case, Pb^{2+} ions are substituted with Mn^{2+} in the octahedron structure of $(\text{PbX}_6)^{4-}$ under certain conditions such as particular temperatures of medium or Mn^{2+} concentrations.

The instability of these halide perovskites (Huang et al. 2017) is a major obstacle needs to be considered overcome because the perovskites readily undergo chemical degradation, accordingly optical loss. Even though all-inorganic halide perovskites show better stability compared to their organic counterparts most probably due to the intrinsic stability of Cs^+ to MA^+ or FA^+ . These perovskite crystals still suffer from the chemical instability against moisture, oxygen, and polar solvents such as water, acetone, and ethanol. Apart from the chemical instability, anion-exchange reactions cause floating PL emission in terms of its color because of the changing wavelength signals when two or more halide perovskites are mixed. It leads to ambiguity in the optical features of WLED. There are various methods developed to improve the stability of halide perovskites. For instance, Wang *et al.* (Wang et al. 2016) mixed mesoporous silica having pore size of 12-15 nm with green CsPbBr_3 halide perovskite in non-polar solvent, and found that this method is able to prevent anion-exchange reactions between green CsPbBr_3 and red $\text{CsPb}(\text{Br}_{0.4}\text{I}_{0.6})_3$ when they mixed in silicone resin (**Figure 5.4 (a)**). As an example, Bhaumik *et al.* (Bhaumik et al. 2016) reported that they obtained stable MAPbBr_3 by growing shell of octyl-ammonium lead bromide, which has a high band-gap over the MAPbBr_3 (**Figure 5.4 (b)**). This method of growing wider band-gap shell over lower band-gap core is also known as core-shell semiconducting nanocrystals. (Shirasaki et al. 2013)

5.4 Use of Halide Perovskites in WLED Applications

In this section, we will summarize the studies employing halide perovskites as color conversion layers in white LED applications.

5.4.1 Blue LED + YAG: Ce^{3+} + Halide Perovskite

In YAG:Ce³⁺ based WLED applications, generated white light, in general, exhibits lower CRI since the resulting spectrum lacks of the red component. To improve CRI, red phosphors, particularly the ones having narrow FWHM can be integrated into the system.(Lin, Meijerink, and Liu 2016a) In this sense, red halide perovskite crystals can

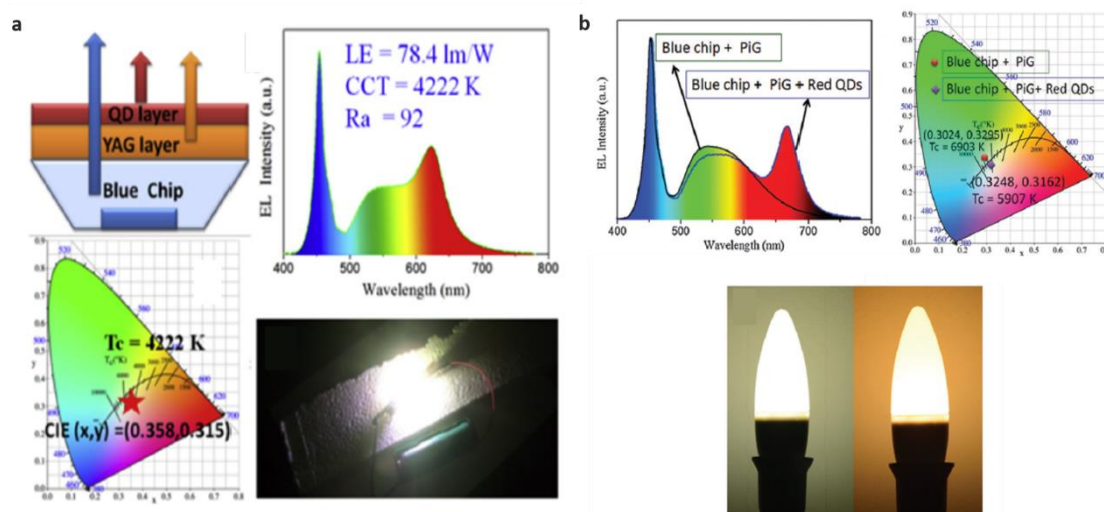


Figure 5.5 WLED applications of red halide perovskites integrated into the blue LED excited YAG:Ce³⁺ phosphor, which are **a)** directly coated on blue LED(Source: Zhou et al. 2017) or **b)** prepared in the form of PiG, (Source: Zhou, Huang, et al. 2016) systems.

be used to improve CRI and reduce CCT by integrating them into traditional phosphor converted WLED applications. Following this strategy, *Zhou et al.*(Zhou et al. 2017) fabricated red-emitting perovskites NCs by alloying CsPbI₃ with Br⁻ (leading to CsPbBr_{1.2}I_{1.8}) having better stability against moisture, compared to CsPbI₃. Using this alloyed red-emitting perovskite QDs in PMMA/chloroform solution, the authors covered the upper surface of a YAG-based WLED device using spin coating method (**Figure 5.5 (a)**). As a result, this WLED system showed CRI of 92, CCT of 4222 K, and LE of 78.41 lm/W, which is superior to bare YAG-based WLED system (with CRI of 74, and CCT of 6713K). Similarly, *Zhou et al.*(Zhou, Huang, et al. 2016) also reported a promising red CsPbBr_{3-x}I_x halide perovskite QDs used in a YAG:Ce³⁺ based WLED system. The optical properties of this red halide perovskite was examined to find optimum value of *x* reported as 2, showing both high quantum yield and intensive luminescence. Then, the authors were embedded the optimized halide perovskite (CsPbBrI₂) into PMMA and then deposited it on the upper surface of YAG:Ce³⁺ based phosphor-in-glass (PiG) disk by

using spin coating (**Figure 5.5 (b)**). It was found that placing this color conversion layer over blue LED in a remote system resulted in CRI of 90, CCT of 5907 K, and LE of 58 lm/W, which are quite satisfactory suggesting that halide perovskites are promising materials for future WLED applications. On the other hand, *Song et al.* (Song et al. 2017) argued that PMMA can cause degradation for these perovskites, and the authors offered ethyl cellulose as alternative to PMMA. Two red-emitting CsPb(Br_{0.4}I_{0.6})₃ halide perovskite embedded polymeric films were prepared using ethyl cellulose and PMMA as matrix. The quantum yield of halide perovskite in ethyl cellulose was reduced from 34.2% to 19.8% while PMMA-based one reduced from 34.9% to 9.5% after 200 h dipping time of films in water. Stabilization of perovskite materials against water, compared to PMMA-based one, was claimed as it is the result of passivation characteristics of ethyl cellulose. Meanwhile, white color obtained from the ethyl cellulose based halide perovskite QDs integrated YAG:Ce³⁺ - blue LED system showed CRI of 90.3, CCT of 3897.9 K, and LE of 46.45 lm/W under 20 mA forward-bias current. Even though PMMA is able to keep QDs bright luminescence due to its high transparency, it does not show a significant stability improvement against UV exposure, and also against to photo-oxidation since the oxygen diffusion coefficient of PMMA is relatively high. (Hormats and Unterleitner 1965) In this sense, to provide further stability for halide perovskite QDs, *Di et al.* (Di et al. 2017) prepared these QDs coated with mesoporous silica. They showed that all-inorganic perovskites can keep their optical performance for months under air atmosphere. As a WLED application, the authors used two systems with two different chemistries of halide perovskites; CsPbBr₃/silica as green-emitting, and CsPb(Br_{0.4}I_{0.6})₃/silica as red-emitting conversion layers. In the first system, they stacked red-emitting perovskite QDs/silica blended with organic paste film on a PiG plate over a blue LED. In the second, green-emitting and red-emitting perovskite QD/silica powders with blue LED were combined. It is reported that the former strategy exhibits CRI of 92, CCT of 5198 K, LE of 75.2 lm/W while the latter shows CRI of 82, CCT of 5853 K, and LE of 14.1 lm/W. Obviously, the first strategy performs better than the second one. The authors then optimized the white light generation in terms of the concentration of red perovskite, and reach to CRI of 92, CCT of 4718 K, and LE of 56 lm/W under 20 mA driving current for the particular concentration. In another approach, same halide perovskite QDs with various x of CsPbBr_{3-x}I_x were used in the form of liquid-type, which is about keeping the related quantum dot solution in liquid phase while protecting them from drying. For instance, *Sher et al.* (Sher et al. 2016) used a glass material to keep QD

solution in liquid form, and the authors showed that the liquid-type QD structure can stabilize the QDs against environment while providing high and reliable CRI. Moreover, this method was also found to improve the efficiency of QDs and reduce the thermal effects. In the case of halide perovskites, *Bi et al.* (Bi et al. 2017) prepared red CsPb(Br/I)₃ liquid-type QDs and combined them with the traditional yellow phosphor YAG:Ce³⁺ as color conversion layers to fabricate warm WLED pumped with a blue LED. As a result of this combination, luminous efficiency of 84.7 lm/W, CRI of 89, and CCT range between 2853 K – 11.068 K can be achieved depending on the QD concentration while maintaining its initial quantum efficiency.

5.4.2 Blue LED + Halide Perovskite

Apart from integrating red perovskite QDs into the YAG:Ce³⁺ based pc-WLEDs, one can also replace the traditional YAG:Ce³⁺ yellow phosphor with the perovskites such as green-emitting CsPbBr₃. In this context, *Li et al.* (Li, Wu, et al. 2016) used all-inorganic red and green halide perovskite QDs in PMMA matrix, and casted them as separate layers

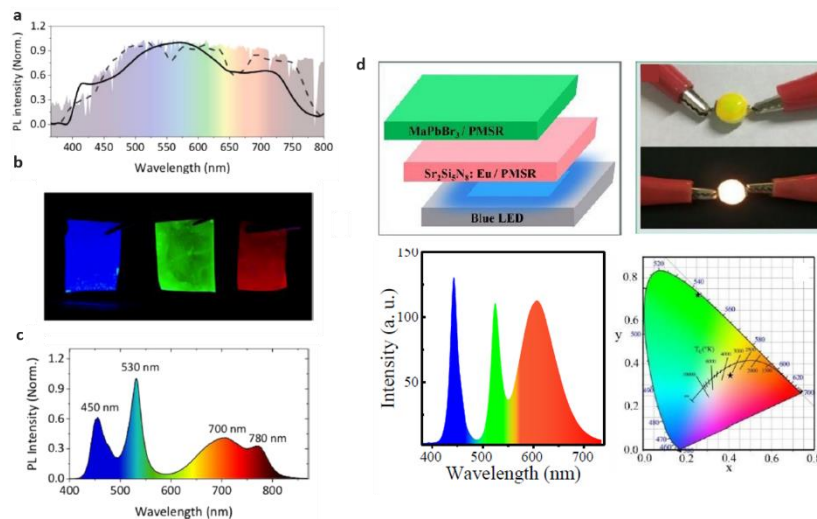


Figure 5.6 **a)** Spectrum of the mixture of blue, green, and red halide perovskites. **b-**
c) present the appearance of blue, green, and red halide perovskites under
 UV illumination, and their related spectrum after stacking them onto the
 blue LED, respectively. Reprinted (adapted) with permission from
 (Source: Pathak et al. 2015). Copyright (2015) American Chemical
 Society. **d)** WLED fabricated via stacking the green emitting halide
 perovskite with a red phosphor over blue LED. (Source: Wang et al. 2017)

over blue LED. Then by simply changing the red and green QD component ratio, CCT was tuned between 2500 K and 11500 K. The resulting CIE color coordinate was optimized to (0.33, 0.30), which is very close to the standard coordinate of (0.33, 0.33) as white color. In another case, *Pathak et al.* (Pathak et al. 2015), first, reported that by varying the ratio of OA and MA in the synthesis of perovskite, the size of the crystals can be controlled down to 5 -10 nm length scale of resulting crystals. By substituting MA with OA, the authors observed that PL quantum yield was enhanced from 20% to 36% (from MA only to 0.6 OA:0.4 MA molar ratio). However, further increase in molar ratio results in a decrease for quantum yield (18% for 0.9 OA:0.1 MA molar ratio). Next, the authors blended PS with the mixture of blue, green, red, and emitting crystals at intermediate regions from 410 to 770 nm (which can be obtained via mixing I⁻/Br⁻ and Br⁻/Cl⁻ halides), and they have found that the mixture can cover visible range (**Figure 5.6 (a)**). Moreover, the authors fabricated PS / perovskite composite films by embedding PbBr₃ emitting at 520 nm, Pb(I_{0.66}Br_{0.34})₃ emitting at 678 nm, and PbI₃ emitting at 775 nm in PS matrix separately, which are presented in **Figure 5.6 (b)** (under UV illumination). By stacking these films over the blue LED chip, the authors generated white light (**Figure 5.6 (c)**) which has optical features of CRI of 86 and CCT of 5229 K. *Meyns et al.* (Meyns et al. 2016) offered that introducing poly(maleic anhydride-alt-1-octadenece) (PMA) during the synthesis of halide perovskites can increase their quantum yield while stabilizing their optical features by protecting their surface and preventing them from aggregation. Two perovskites emitting in green CsPbBr₃-PMA and emitting in red CsPbBr_{1.6}I_{1.4}-PMA were prepared and employed in stacking configuration over blue LED. It was found that CRI of 72.4, and CCT of 3665 K were obtained initially, and then due to degradation of the red component, CRI was reduced to 66.9 and CCT increased to 9300 K after 5 min even in the presence of PMA. *Wei et al.* (Wei et al. 2017) were packed all-inorganic perovskites into cross-linked polystyrene (PS) beads in the form of perovskite QD@PS by using swelling-shrinking strategy. The authors were able to stabilize perovskite QDs against water, acid aqueous solution, alkali aqueous solution, etc. while maintaining their high luminescence and then they have fabricated WLED using blue LED and mix of green CsPbBr₃@PS and red CsPb(Br_{0.4}I_{0.6})₃@PS halide perovskites. The spectrum of the prepared WLED was found to possess three individual emission signals, which indicate that ion-exchange reaction was also achieved to be prevented between green and red halide perovskites. In other words, green and red halide perovskites are able to maintain their corresponding solid state PL spectra even after they

were mixed. With this system, the authors were found that the generated white light has color coordinates of (0.31, 0.30). In the case of organometallic halide perovskites, *Zhang et al.* (Zhang, Zhong, et al. 2015) blended halide perovskite having organic cation MA with PMMA/chloroform solution, and they combined it with a red phosphor KSF dispersed in a silicone gel as separate layers over a blue LED. Resulting WLED was found to possess luminous efficiency of 48 lm/W, and color coordinate of (0.33, 0.27). The authors pointed out that casting the MAPbBr₃/PMMA over a blue LED painted with a KSF silicone gel shows superior performance compared to the CdSe-based LEDs in terms of color rendition. (Jang et al. 2010) Similarly, *Wang et al.* (Wang et al. 2017) used two commercial silicone resins to prepare stable green organometallic halide perovskite MAPbBr₃ nanocomposites (**Figure 5.6 (d)**). Among them, QDs prepared with phenyl methyl silicone resin (PMSR) was found to exhibit better stability against UV, water, and thermal than the one prepared with silicone sealant Dow Corning 937 (SSDC). The authors, then, fabricated a WLED by using green emissive PMSR/QD and red emissive nitride phosphor PMSR/Sr₂Si₅N₈:Eu³⁺ composite films as separate layers over a blue LED. They obtained CCT of 3100 K and color coordinates of (0.402, 0.348), where the highest quantum yield of 62% was also obtained. Another example, *Ma et al.* (Ma et al. 2017) used green emitting CsPbBr₃ halide perovskites that were synthesized *in situ* in the presence of PMMA via a microfluidic-spinning microreactor. This synthesis method of perovskite by *in situ* endowed great PL stability against water moisture and UV radiation while the use of microfluidic-spinning microreactor allowed a scale-up fabrication. For WLED application, the authors embedded the mixture of CsPbBr₃/PMMA and emitting CdSe QD into UV-curable adhesive, and then blue LED was encapsulated with this film to generate white light. They reported that the resulting white light possesses CRI of 89.2 with color coordinates of (0.3413, 0.3329) under 350 mA operation. Apart from polymers, perovskites can be prepared via incorporating them into microcrystals similar to QDs embedded in inorganic salts, which can lead to enhancement for the photo and chemical stabilities. (Otto et al. 2012, Adam et al. 2015, Erdem et al. 2016, Müller et al. 2014) Using this strategy, *Xu et al.* (Xu et al. 2017) incorporated halide perovskites into carboxybenzene (CB) crystals, and they found that mixing halide perovskites with CB enhances the stability of perovskite QDs against moisture and blue light while keeping its PL properties. Furthermore, they have prepared WLED device composing of the mixture of green-emitting CsPbBr₃-CB and red-emitting CsPb(Br_{0.4}I_{0.6})₃-CB, and blue LED. They observed that anion-exchange reactions can be prevented due to the presence

of CB, and obtained color coordinates of (0.41, 0.37), which also shows only a 7% reduction in PL intensity after 30 h continuous illumination.

5.4.3 UV LED + Halide Perovskite

Fabricating WLED using UV LED chip requires three main RGB color to be generated under UV illumination. In this context, halide perovskites are suitable pigments for use as color conversion layers. These materials can be excited by UV and cover the visible spectrum. *Zhang et al.* (Zhang et al. 2017) reported mixing of organic cations MA and FA in particular ratios, 1:1 for blue, and 4:1 for green emissions, respectively. Single cation FA was used to produce red emission. All these materials having blue, green, and red emission were dissolved in PMMA/chloroform solution, and then blended with thermocurable silicone resin. As a WLED application, UV LED chip coated separately with halide perovskite composite films, and CRI of 85, luminous efficiency of 40.2 lm/W were obtained (**Figure 5.7**). Similarly, *Palazon et al.* (Palazon et al. 2016) prepared color conversion layers either involving solely all-inorganic halide perovskites for all colors or

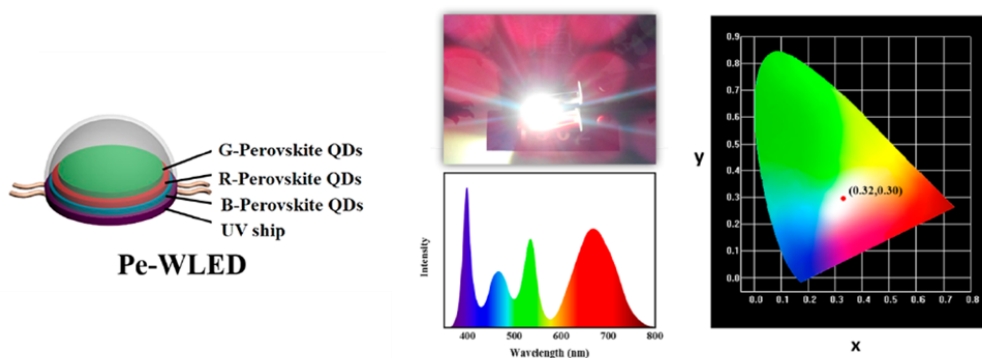


Figure 5.7 **a)** Schematic representation of WLED prepared using halide perovskites over UV LED chip, and **b)** resulting white light generation. Reprinted (adapted) with permission from (Source: Zhang et al. 2017). Copyright (2017) American Chemical Society.

replacing the red color with non-perovskite emitters such as Cu-In-Zn-S (CIZS) (De Trizio et al. 2012) or giant-shell CdSe/CdS nanocrystals (Christodoulou et al. 2014) and place them over a 365 nm UV LED chip. In the case of former, they colloiddally synthesize all colors from two main perovskites CsPbBr_3 and CsPbI_3 but differing in morphology.

The CsPbBr₃ nanocubes and nanoplatelets emit blue and green; CsPbI₃ nanocubes and nanosheets emit red and orange, respectively. Apart from the instability observed for the perovskite mixture due to anion-exchange reactions, CsPbI₃ suffers also from the intrinsic instability that causes serious PL degradation particularly against the irradiation (Palazon et al. 2015). This is the reason of lower overall efficiency observed in the stacking case of perovskites (1.19 Cd at the excitation power of 800 mW). In latter case, the authors mixed blue-green emitting CsPbBr₃ nanocubes-nanoplatelets with CIZS and CdSe/CdS, and obtained $x=0.31467$; $y=0.34251$; CCT=6317 K from CIZS, $x=0.32396$; $y=0.35315$; CCT=5856 K from CdSe/CdS based solution. White light is obtained in all approaches with tunable CCT; among those the hybrid approach involving CdSe/CdS nanocrystals showed very high stability upon continuous illumination at high power.

5.5 Summary

WLED applications demand energy-efficient devices satisfying high CRI, tunable CCT, and high luminous flux along with low cost. Last two decades of WLED related studies indicate that phosphor studies started to level off most probably due to reaching saturation in terms of new phosphor discoveries or their optimization. In recent years, halide perovskites attract great attention since they are able to provide the desired optical features with high quantum yields. However, instability against environmental conditions such as humidity and polar solvents still remains an issue. The optical features of these materials (i.e. their high quantum yield) have to be maintained or at least the optical loss has to be minimized after integrating with polymers such as silicone resin because of the quenching effect of macromolecules through surface interactions and/or aggregation of the molecules. Nevertheless, halide perovskites are new, hot-debate, and promising materials for the WLED applications. They appear a strong alternative to phosphors and will lead to a significant rise in the number of WLED related studies.

CHAPTER 6

CONCLUSION

Since lighting is responsible for nearly 20% of electricity consumption worldwide (Waide and Tanishima 2006), the invention of light-emitting diodes (LED) has been deemed a breakthrough in minimizing global energy consumption. (Shinde and Dhoble 2014) LED lighting has also prompted the production of a wide range of lighting applications, including in white light, as a promising alternative to incandescent and fluorescent lamps. (Ye et al. 2010, Tan et al. 2012) Phosphor-converted white LEDs (George, Denault, and Seshadri 2013, Lin and Liu 2011, Ye et al. 2010, Allen and Steckl 2008, McKittrick and Shea- Rohwer 2014) (pc-wLEDs) are widely used to produce white light of varying color quality and indispensable to the lighting industry because of their low energy consumption. In blue LEDs with a yellow phosphor (Shinde and Dhoble 2014, Ye et al. 2010, Lin and Liu 2011, George, Denault, and Seshadri 2013), blue light excites the phosphor particles to produce yellow light, which then combines with blue light to generate white light.

Flexible polymer–phosphor composite films have been used with blue LEDs in the form of direct coatings or remote phosphors (Allen and Steckl 2008, Narendran et al. 2005, Tran, You, and Shi 2009b, Acuña et al. 2014). Studies on various polymer–phosphor composites for use in solid-state lighting have been reported in the literature; (Narendran et al. 2005, Allen and Steckl 2008, Song, Han, et al. 2015) these composites include $\text{CeF}_3:(\text{Tb}^{3+}, \text{Dy}^{3+}, \text{Eu}^{3+})$ (Sayed et al. 2011), $\text{YVO}_4:(\text{Eu}^{3+})$ (Hreniak et al. 2011), GYAG (Bera et al. 2010), $\text{YAG}:(\text{Ce}^{3+}, \text{Gd}^{3+})$ (Tucureanu et al. 2015), $\text{YAG}:(\text{Ce}^{3+})$ (Allen and Steckl 2008, Saladino et al. 2010, Saladino et al. 2014, Oliva et al. 2014), $\text{Zn}_2\text{SiO}_4:(\text{Mn}^{2+}, \text{Eu}^{3+})$, (Đaćanin et al. 2012) $\text{BaIn}_6\text{Y}_2\text{O}_{13}:(\text{Yb}^{3+}, \text{Tm}^{3+}, \text{Er}^{3+})$ (Zhang, Yang, et al. 2015) particles dispersed in poly(methyl methacrylate), Na_2SO_4 (Zhang et al. 2013), $\text{BaAl}_x\text{O}_y:(\text{Eu}^{2+}, \text{Dy}^{3+})$ (Bem et al. 2011) in low-density polyethylene, $\text{YAG}:\text{Ce}^{3+}$ in polydimethylsiloxane (PDMS) (Esteves, Brokken-Zijp, Laven, and de With 2010, Esteves, Brokken-Zijp, Laven, Huinink, et al. 2010), $\text{YBO}_3:(\text{Eu}^{2+})$ (Bussière et al. 2013)

and YGG:(Tb³⁺)(Potdevin et al. 2012) in a polyvinylpyrrolidone matrix, and YAG:Ce³⁺ mixed with melted polycarbonate(Saladino et al. 2016).

However, the use of phosphors, which contain rare-earth elements, in LED packages may pose significant challenges in terms of cost and raw material availability. Considering current limitations, any material that can improve the performance of phosphors may be of strong demand in the industry(Lai, Li, and Shen 2017). Regarding to this fact, different material composition systems have been investigated throughout this thesis. First, since employing yellow phosphor (YAG:Ce³⁺) produces white light with low CRI, and high CCT, improving these parameters via employing additional red phosphor were studied. Two different methods were compared; stacking layers or mixture in order to determine how one can introduce red phosphors to obtain better white light by spraying over a given substrate. Second, apart from dealing with CRI, and CCT, efficiency of the YAG:Ce³⁺ phosphors were investigated via employing glass beads in order to adjust the scattering level of the prepared PDMS/YAG:Ce³⁺ composites. As a result, by tuning the scattering throughout the composites, we have achieved 33% reduction in the phosphor consumption, which is cost efficient, and more environmental-friendly since less phosphor is required in order to fabricate white light. Third, rapid, and water-based synthesis of red UV phosphors was proposed. Resulting crystal morphology, and corresponding PL were investigated depending on the synthesis time at first, and then these are again explored at different dopant ratios. This method will be used in order to obtain different phosphors in future, and since it can be considered as green chemistry, it can make the production of phosphors more feasible, and environmental-friendly. Fourth, apart from phosphors, we have employed organic dyes, which have absorption range lying in the blue region, into PS fibers, and then their free-standing films were prepared via coating them with PDMS. Using few amount of these dyes can lead to generation of white light with high CRI and low CCT, which are tunable depending on the amount of employed fibers in terms of mass. At last, we have summarized the future prospects, which is based on halide perovskites and their possible use as color conversion layers in white light applications as a promising technology.

We have proposed different processing methods by using purchased materials or new materials to be used as color conversion layers in phosphor-converted white LED systems throughout this thesis. We believe that improving the efficiency of LED-based lighting is crucial to reduce electricity consumption in near future, where energy demand of the

whole world will reach to significant degree in the sense of production-consumption point of view. Therefore, in future, existing LED-based lighting systems should be studied either to improve efficiency of existing LED packages or new materials such as organic dyes, halide perovskites, carbon dots etc., especially the ones that have high quantum yield and stability, and environmental-friendly, should be involved as color conversion layers to make these lighting products more feasible and attractive.

As a result, we have focused on the use of various down-converting materials such as phosphors, organic dyes, halide perovskites, carbon dots, etc. to produce efficient white light together with their integration into polymeric systems effectively throughout this thesis. In the case of using organic dyes as down-converting materials, electrospinning technique was used to prepare polymer/organic dye fibers in order to reduce the organic dye consumption significantly. Moreover, a method involving environmental friendly (water-based) and commercially viable synthesis conditions (<1h reaction time at room temperature) was also proposed to make phosphor fabrication more favorable.

REFERENCES

- Acuña, Paula, Sven Leyre, Jan Audenaert, Youri Meuret, Geert Deconinck, and Peter Hanselaer, Power and photon budget of a remote phosphor LED module, *Optics Express*, 22 (2014), A1079-A1092.
- Adam, Marcus, Zhiyu Wang, Aliaksei Dubavik, Gordon M Stachowski, Christian Meerbach, Zeliha Soran- Erdem, Christin Rengers, Hilmi Volkan Demir, Nikolai Gaponik, and Alexander Eychmüller, Liquid–Liquid Diffusion-Assisted Crystallization: A Fast and Versatile Approach Toward High Quality Mixed Quantum Dot- Salt Crystals, *Advanced Functional Materials*, 25 (2015), 2638-2645.
- Adjokatse, Sampson, Hong-Hua Fang, and Maria Antonietta Loi, Broadly tunable metal halide perovskites for solid-state light-emission applications, *Materials Today*, (2017).
- Akkerman, Quinten A, Valerio D’Innocenzo, Sara Accornero, Alice Scarpellini, Annamaria Petrozza, Mirko Prato, and Liberato Manna, Tuning the optical properties of cesium lead halide perovskite nanocrystals by anion exchange reactions, *Journal of the American Chemical Society*, 137 (2015), 10276-10281.
- Allen, Steven C, and Andrew J Steckl, A nearly ideal phosphor-converted white light-emitting diode, *Applied Physics Letters*, 92 (2008), 143309.
- Bachmann, Volker, Cees Ronda, and Andries Meijerink, Temperature quenching of yellow Ce³⁺ luminescence in YAG: Ce, *Chemistry of Materials*, 21 (2009), 2077-2084.
- Bai, Sai, Zhongcheng Yuan, and Feng Gao, Colloidal metal halide perovskite nanocrystals: synthesis, characterization, and applications, *Journal of Materials Chemistry C*, 4 (2016), 3898-3904.
- Bai, Yunfeng, Yuxiao Wang, Guanya Peng, Kun Yang, Xueru Zhang, and Yinglin Song, Enhance upconversion photoluminescence intensity by doping Li⁺ in Ho³⁺ and Yb³⁺ codoped Y₂O₃ nanocrystals, *Journal of Alloys and Compounds*, 478 (2009), 676-678.
- Bekenstein, Yehonadav, Brent A Koscher, Samuel W Eaton, Peidong Yang, and A Paul Alivisatos, Highly luminescent colloidal nanoplates of perovskite cesium lead halide and their oriented assemblies, *J. Am. Chem. Soc.*, 137 (2015), 16008-16011.

- Bem, Daniel B, Hendrick C Swart, Adriaan S Luyt, and Francis B Dejene, Luminescent properties of long- lasting BaAlxOy: Eu²⁺, Dy³⁺ nanocomposites, *Journal of Applied Polymer Science*, 121 (2011), 243-252.
- Bera, Debasis, Sergey Maslov, Lei Qian, Jae Soo Yoo, and Paul H Holloway, Optimization of the yellow phosphor concentration and layer thickness for down-conversion of blue to white light, *Journal of Display technology*, 6 (2010), 645-651.
- Bhaumik, Saikat, Sjoerd A Veldhuis, Yan Fong Ng, Mingjie Li, Subas Kumar Muduli, Tze Chien Sum, Bahulayan Damodaran, Subodh Mhaisalkar, and Nripan Mathews, Highly stable, luminescent core-shell type methylammonium-octylammonium lead bromide layered perovskite nanoparticles, *Chemical Communications*, 52 (2016), 7118-7121.
- Bi, Ke, Dan Wang, Peng Wang, Bin Duan, Tieqiang Zhang, Yinghui Wang, Hanzhuang Zhang, and Yu Zhang, Cesium lead halide perovskite quantum dot-based warm white light-emitting diodes with high color rendering index, *Journal of Nanoparticle Research*, 19 (2017), 174.
- Buissette, Valérie, Domitille Giaume, Thierry Gacoin, and Jean-Pierre Boilot, Aqueous routes to lanthanide-doped oxide nanophosphors, *Journal of Materials Chemistry*, 16 (2006), 529-539.
- Burschka, Julian, Norman Pellet, Soo-Jin Moon, Robin Humphry-Baker, Peng Gao, Mohammad K Nazeeruddin, and Michael Grätzel, Sequential deposition as a route to high-performance perovskite-sensitized solar cells, *Nature*, 499 (2013), 316-319.
- Bussière, Pierre-Olivier, Jérémy Peyroux, Geneviève Chadeyron, and Sandrine Therias, Influence of functional nanoparticles on the photostability of polymer materials: Recent progress and further applications, *Polymer Degradation and Stability*, 98 (2013), 2411-2418.
- Cai, Bing, Yedi Xing, Zhou Yang, Wen-Hua Zhang, and Jieshan Qiu, High performance hybrid solar cells sensitized by organolead halide perovskites, *Energy & Environmental Science*, 6 (2013), 1480-1485.
- Caruso, F, M Mosca, R Macaluso, E Feltin, and C Calì, Generation of white LED light by frequency downconversion using perylene-based dye, *Electronics letters*, 48 (2012), 1417-1419.

- Chen, Wangqiao, Xuan Yang, Guankui Long, Xiangjian Wan, Yongsheng Chen, and Qichun Zhang, A perylene diimide (PDI)-based small molecule with tetrahedral configuration as a non-fullerene acceptor for organic solar cells, *Journal of Materials Chemistry C*, 3 (2015), 4698-4705.
- Cho, Jaehee, Jun Hyuk Park, Jong Kyu Kim, and E Fred Schubert, White light-emitting diodes: History, progress, and future, *Laser & Photonics Reviews*, (2017).
- Choi, Hyosung, Jaeki Jeong, Hak-Beom Kim, Seongbeom Kim, Bright Walker, Gi-Hwan Kim, and Jin Young Kim, Cesium-doped methylammonium lead iodide perovskite light absorber for hybrid solar cells, *Nano Energy*, 7 (2014), 80-85.
- Choi, Ju H, Jae Y Hyun, Ki H Kim, and Jae P Kim. 2013. "Synthesis of core-shell Y 2 O 3 nanoparticles for enhanced luminescence efficiency." *Active Photonic Materials V*.
- Christodoulou, S, G Vaccaro, V Pinchetti, F De Donato, JQ Grim, A Casu, A Genovese, G Vicidomini, A Diaspro, and S Brovelli, Synthesis of highly luminescent wurtzite CdSe/CdS giant-shell nanocrystals using a fast continuous injection route, *Journal of Materials Chemistry C*, 2 (2014), 3439-3447.
- Correa-Baena, Juan-Pablo, Michael Saliba, Tonio Buonassisi, Michael Grätzel, Antonio Abate, Wolfgang Tress, and Anders Hagfeldt, Promises and challenges of perovskite solar cells, *Science*, 358 (2017), 739-744.
- Cottingham, Patrick, and Richard L Brutchey, On the crystal structure of colloiddally prepared CsPbBr 3 quantum dots, *Chemical Communications*, 52 (2016), 5246-5249.
- Đaćanin, Ljubica, Svetlana R Lukić, Dragoslav M Petrović, Željka Antić, Radenka Kršmanović, Milena Marinović-Cincović, and Miroslav D Damićanin, PMMA/Zn₂SiO₄: Eu³⁺ (Mn²⁺) Composites: Preparation, Optical, and Thermal Properties, *Journal of Materials Engineering and Performance*, 21 (2012), 1509-1513.
- Darr, Jawwad A, Jingyi Zhang, Neel M Makwana, and Xiaole Weng, Continuous hydrothermal synthesis of inorganic nanoparticles: applications and future directions, *Chemical Reviews*, 117 (2017), 11125-11238.
- De Trizio, Luca, Mirko Prato, Alessandro Genovese, Alberto Casu, Mauro Povia, Roberto Simonutti, Marcelo JP Alcocer, Cosimo D'Andrea, Francesco Tassone, and Liberato Manna, Strongly Fluorescent Quaternary Cu–In–Zn–S

Nanocrystals Prepared from Cu_{1-x}InS₂ Nanocrystals by Partial Cation Exchange, *Chemistry of Materials*, 24 (2012), 2400-2406.

Demir, Hilmi Volkan, Sedat Nizamoglu, Talha Erdem, Evren Mutlugun, Nikolai Gaponik, and Alexander Eychmüller, Quantum dot integrated LEDs using photonic and excitonic color conversion, *Nano Today*, 6 (2011), 632-647.

Demir, Mustafa M, Patrice Castignolles, Ümit Akbey, and Gerhard Wegner, In-situ bulk polymerization of dilute particle/MMA dispersions, *Macromolecules*, 40 (2007), 4190-4198.

Demir, Mustafa M, Mine Memesa, Patrice Castignolles, and Gerhard Wegner, PMMA/Zinc Oxide Nanocomposites Prepared by In- Situ Bulk Polymerization, *Macromolecular Rapid Communications*, 27 (2006), 763-770.

Demir, Mustafa M, Yusuf Z Menciloglu, and Burak Erman, Effect of filler amount on thermoelastic properties of poly (dimethylsiloxane) networks, *Polymer*, 46 (2005), 4127-4134.

Demir, Mustafa M, and Gerhard Wegner, Challenges in the preparation of optical polymer composites with nanosized pigment particles: a review on recent efforts, *Macromolecular Materials and Engineering*, 297 (2012), 838-863.

Demir, Mustafa Muammer, I Yilgor, EEA Yilgor, and Burak Erman, Electrospinning of polyurethane fibers, *Polymer*, 43 (2002), 3303-3309.

Di, Xiaoxuan, Jutao Jiang, Zemin Hu, Lei Zhou, Pengzhi Li, Sijin Liu, Weidong Xiang, and Xiaojuan Liang, Stable and brightly luminescent all-inorganic cesium lead halide perovskite quantum dots coated with mesoporous silica for warm WLED, *Dyes and Pigments*, 146 (2017), 361-367.

Dubey, Abhishek, Abhishek Kumar Soni, Astha Kumari, Riya Dey, and Vineet Kumar Rai, Enhanced green upconversion emission in NaYF₄: Er³⁺/Yb³⁺/Li⁺ phosphors for optical thermometry, *Journal of Alloys and Compounds*, 693 (2017), 194-200.

Eperon, Giles E, Giuseppe M Paternò, Rebecca J Sutton, Andrea Zampetti, Amir Abbas Haghighirad, Franco Cacialli, and Henry J Snaith, Inorganic caesium lead iodide perovskite solar cells, *Journal of Materials Chemistry A*, 3 (2015), 19688-19695.

Eperon, Giles E, Samuel D Stranks, Christopher Menelaou, Michael B Johnston, Laura M Herz, and Henry J Snaith, Formamidinium lead trihalide: a broadly tunable

perovskite for efficient planar heterojunction solar cells, *Energy & Environmental Science*, 7 (2014), 982-988.

Erdem, Talha, and Hilmi Volkan Demir, Color science of nanocrystal quantum dots for lighting and displays, *Nanophotonics*, 2 (2013), 57-81.

Erdem, Talha, Sedat Nizamoglu, and Hilmi Volkan Demir, Computational study of power conversion and luminous efficiency performance for semiconductor quantum dot nanophosphors on light-emitting diodes, *Optics Express*, 20 (2012), 3275-3295.

Erdem, Talha, Zeliha Soran-Erdem, Yusuf Kelestemur, Nikolai Gaponik, and Hilmi Volkan Demir, Excitonic improvement of colloidal nanocrystals in salt powder matrix for quality lighting and color enrichment, *Optics Express*, 24 (2016), A74-A84.

Esteves, de ACC, J Brokken-Zijp, J Laven, and G de With, Light converter coatings from cross-linked PDMS/particles composite materials, *Progress in Organic Coatings*, 68 (2010), 12-18.

Esteves, de ACC, J Brokken-Zijp, J Laven, HP Huinink, NJW Reuvers, MP Van, and G de With, Garnet particles effect on the cross-linking of PDMS and the network structures formed, *Polymer*, 51 (2010), 136-145.

Etgar, Lioz, Peng Gao, Zhaosheng Xue, Qin Peng, Aravind Kumar Chandiran, Bin Liu, Md K Nazeeruddin, and Michael Grätzel, Mesoscopic CH₃NH₃PbI₃/TiO₂ heterojunction solar cells, *Journal of the American Chemical Society*, 134 (2012), 17396-17399.

Fan, Wei, Ningning Liang, Dong Meng, Jiaping Feng, Yan Li, Jianhui Hou, and Zhaohui Wang, A high performance three-dimensional thiophene-annulated perylene dye as an acceptor for organic solar cells, *Chemical Communications*, 52 (2016), 11500-11503.

George, Nathan C, Kristin A Denault, and Ram Seshadri, Phosphors for solid-state white lighting, *Annual Review of Materials Research*, 43 (2013), 481-501.

Goldschmidt, Victor Moritz, Die gesetze der krystallochemie, *Naturwissenschaften*, 14 (1926), 477-485.

Green, Martin A, Anita Ho-Baillie, and Henry J Snaith, The emergence of perovskite solar cells, *Nature Photonics*, 8 (2014), 506-514.

- Guner, Tugrul, Erkan Aksoy, Mustafa M Demir, and Canan Varlikli, Perylene-embedded electrospun PS fibers for white light generation, *Dyes and Pigments*, 160 (2019), 501-508.
- Guner, Tugrul, and Mustafa M Demir, A Review on Halide Perovskites as Color Conversion Layers in White Light Emitting Diode Applications, *physica status solidi (a)*, (2018), 1800120.
- Guria, Amit K, Sumit K Dutta, Samrat Das Adhikari, and Narayan Pradhan, Doping Mn²⁺ in Lead Halide Perovskite Nanocrystals: Successes and Challenges, *ACS Energy Letters*, 2 (2017), 1014.
- Güner, Tuğrul, Devrim Köseoğlu, and Mustafa M Demir, Multilayer design of hybrid phosphor film for application in LEDs, *Optical Materials*, 60 (2016), 422-430.
- Hao, Feng, Constantinos C Stoumpos, Robert PH Chang, and Mercouri G Kanatzidis, Anomalous band gap behavior in mixed Sn and Pb perovskites enables broadening of absorption spectrum in solar cells, *Journal of the American Chemical Society*, 136 (2014), 8094-8099.
- Hassan, Yasser, Yin Song, Ryan D Pensack, Ahmed I Abdelrahman, Yoichi Kobayashi, Mitchell A Winnik, and Gregory D Scholes, Structure- Tuned Lead Halide Perovskite Nanocrystals, *Advanced Materials*, 28 (2016), 566-573.
- He, Xianghong, Yongcai Qiu, and Shihe Yang, Fully- Inorganic Trihalide Perovskite Nanocrystals: A New Research Frontier of Optoelectronic Materials, *Advanced Materials*, 29 (2017), 1700775.
- Higashi, Keita, Yutaka Watanabe, Yoshiki Iso, and Tetsuhiko Isobe, Synthesis of Y²⁺ O³⁻: Bi³⁺, Yb³⁺ nanosheets from layered yttrium hydroxide precursor and their photoluminescence properties, *RSC Advances*, 7 (2017), 6671-6678.
- Hormats, Ellis I, and Fred C Unterleitner, Measurement of the Diffusion of Oxygen in Polymers by Phosphorescent Quenching¹, *The Journal of Physical Chemistry*, 69 (1965), 3677-3681.
- Hreniak, D, J Doskocz, P GŁuchowski, R Lisiecki, W Stręk, N Vu, DX Loc, TK Anh, M Bettinelli, and A Speghini, Enhancement of luminescence properties of Eu³⁺: YVO₄ in polymeric nanocomposites upon UV excitation, *Journal of Luminescence*, 131 (2011), 473-476.

- Hu, Run, Xiaobing Luo, Han Feng, and Sheng Liu, Effect of phosphor settling on the optical performance of phosphor-converted white light-emitting diode, *Journal of Luminescence*, 132 (2012), 1252-1256.
- Huang, Chun. 2010. "Perylene diimide-based materials for organic electronics and optical limiting applications." Georgia Institute of Technology.
- Huang, He, Maryna I Bodnarchuk, Stephen V Kershaw, Maksym V Kovalenko, and Andrey L Rogach, Lead Halide Perovskite Nanocrystals in the Research Spotlight: Stability and Defect Tolerance, *ACS Energy Letters*, 2 (2017), 2071-2083.
- Huang, He, Andrei S Susa, Stephen V Kershaw, Tak Fu Hung, and Andrey L Rogach, Control of emission color of high quantum yield $\text{CH}_3\text{NH}_3\text{PbBr}_3$ perovskite quantum dots by precipitation temperature, *Advanced Science*, 2 (2015).
- Hunter, John D, Matplotlib: A 2D graphics environment, *Computing in science and engineering*, 9 (2007), 90-95.
- Hussain, Sk Khaja, Goli Nagaraju, E Pavitra, G Seeta Rama Raju, and Jae Su Yu, La (OH) 3: Eu 3+ and La 2 O 3: Eu 3+ nanorod bundles: growth mechanism and luminescence properties, *CrystEngComm*, 17 (2015), 9431-9442.
- Jang, Eunjoo, Shinae Jun, Hyosook Jang, Jungeun Lim, Byungki Kim, and Younghwan Kim, White- light- emitting diodes with quantum dot color converters for display backlights, *Advanced Materials*, 22 (2010), 3076-3080.
- Jayasimhadri, M, BV Ratnam, Kiwan Jang, Ho Sueb Lee, Baojiu Chen, Soung- Soo Yi, Jung- Hyun Jeong, and L Rama Moorthy, Greenish- Yellow Emission from Dy³⁺- Doped Y₂O₃ Nanophosphors, *Journal of the American Ceramic Society*, 93 (2010), 494-499.
- Jiang, Wei, Long Ye, Xiangguang Li, Chengyi Xiao, Fang Tan, Wenchao Zhao, Jianhui Hou, and Zhaohui Wang, Bay-linked perylene bisimides as promising non-fullerene acceptors for organic solar cells, *Chemical Communications*, 50 (2014), 1024-1026.
- Kojima, Akihiro, Kenjiro Teshima, Yasuo Shirai, and Tsutomu Miyasaka, Organometal halide perovskites as visible-light sensitizers for photovoltaic cells, *Journal of the American Chemical Society*, 131 (2009), 6050-6051.

- Kovalenko, Maksym V., Loredana Protesescu, and Maryna I. Bodnarchuk, Properties and potential optoelectronic applications of lead halide perovskite nanocrystals, *Science*, 358 (2017), 745-750.
- Kozma, Erika, Wojciech Mróz, and Francesco Galeotti, A polystyrene bearing perylene diimide pendants with enhanced solid state emission for white hybrid light-emitting diodes, *Dyes and Pigments*, 114 (2015), 138-143.
- Lai, Chun-Feng, Jia-Sian Li, and Chung-Wen Shen, High-Efficiency Robust Free-Standing Compositing Phosphor Films with 2D and 3D Nanostructures for High-Power Remote White LEDs, *ACS Applied Materials & Interfaces*, 9 (2017), 4851-4859.
- Lee, Jin- Wook, Dong- Jin Seol, An- Na Cho, and Nam- Gyu Park, High- Efficiency Perovskite Solar Cells Based on the Black Polymorph of HC (NH₂) 2PbI₃, *Advanced Materials*, 26 (2014), 4991-4998.
- Lee, Michael M, Joël Teuscher, Tsutomu Miyasaka, Takuro N Murakami, and Henry J Snaith, Efficient hybrid solar cells based on meso-superstructured organometal halide perovskites, *Science*, 338 (2012), 643-647.
- Leung, VYF, A Lagendijk, TW Tukker, AP Mosk, WL IJzerman, and WL Vos, Interplay between multiple scattering, emission, and absorption of light in the phosphor of a white light-emitting diode, *Optics Express*, 22 (2014), 8190-8204.
- Li, Chen, and Henrike Wonneberger, Perylene imides for organic photovoltaics: yesterday, today, and tomorrow, *Advanced Materials*, 24 (2012), 613-636.
- Li, Dongyu, Yuxiao Wang, Xueru Zhang, Hongxing Dong, Lu Liu, Guang Shi, and Yinglin Song, Effect of Li⁺ ions on enhancement of near-infrared upconversion emission in Y₂O₃: Tm³⁺/Yb³⁺ nanocrystals, *Journal of Applied Physics*, 112 (2012), 094701.
- Li, Guopeng, Hui Wang, Ting Zhang, Longfei Mi, Yugang Zhang, Zhongping Zhang, Wenjun Zhang, and Yang Jiang, Solvent- Polarity- Engineered Controllable Synthesis of Highly Fluorescent Cesium Lead Halide Perovskite Quantum Dots and Their Use in White Light- Emitting Diodes, *Advanced Functional Materials*, 26 (2016), 8478-8486.
- Li, Nan, and Kazumichi Yanagisawa, Controlling the morphology of yttrium oxide through different precursors synthesized by hydrothermal method, *Journal of Solid State Chemistry*, 181 (2008), 1738-1743.

- Li, Nan, Kazumichi Yanagisawa, and Nobuhiro Kumada, Facile hydrothermal synthesis of yttrium hydroxide nanowires, *Crystal Growth and Design*, 9 (2009), 978-981.
- Li, Shuixing, Wenqing Liu, Chang-Zhi Li, Tsz-Ki Lau, Xinhui Lu, Minmin Shi, and Hongzheng Chen, A non-fullerene acceptor with a fully fused backbone for efficient polymer solar cells with a high open-circuit voltage, *Journal of Materials Chemistry A*, 4 (2016), 14983-14987.
- Li, Xiaoming, Fei Cao, Dejian Yu, Jun Chen, Zhiguo Sun, Yalong Shen, Ying Zhu, Lin Wang, Yi Wei, and Ye Wu, All inorganic halide perovskites nanosystem: synthesis, structural features, optical properties and optoelectronic applications, *Small*, 13 (2017), 1603996.
- Li, Xiaoming, Ye Wu, Shengli Zhang, Bo Cai, Yu Gu, Jizhong Song, and Haibo Zeng, CsPbX₃ Quantum Dots for Lighting and Displays: Room- Temperature Synthesis, Photoluminescence Superiorities, Underlying Origins and White Light- Emitting Diodes, *Advanced Functional Materials*, 26 (2016), 2435-2445.
- Liang, Ningning, Kai Sun, Zhong Zheng, Huifeng Yao, Guangpeng Gao, Xiangyi Meng, Zhaohui Wang, Wei Ma, and Jianhui Hou, Perylene diimide trimers based bulk heterojunction organic solar cells with efficiency over 7%, *Advanced Energy Materials*, 6 (2016), 1600060.
- Liang, Zhiqin, Suling Zhao, Zheng Xu, Bo Qiao, Pengjie Song, Di Gao, and Xurong Xu, Shape-Controlled Synthesis of All-Inorganic CsPbBr₃ Perovskite Nanocrystals with Bright Blue Emission, *ACS Applied Materials & Interfaces*, 8 (2016), 28824-28830.
- Lin, Chun Che, and Ru-Shi Liu, Advances in phosphors for light-emitting diodes, *The Journal of Physical Chemistry Letters*, 2 (2011), 1268-1277.
- Lin, Chun Che, Andries Meijerink, and Ru-Shi Liu, Critical red components for next-generation white LEDs, *The Journal of Physical Chemistry Letters*, 7 (2016a), 495-503.
- Lin, Chun Che, Andries Meijerink, and Ru-Shi Liu, Critical Red Components for Next-Generation White LEDs, *The Journal of Physical Chemistry Letters*, (2016b).
- Lin, Qianqian, Ardalan Armin, Ravi Chandra Raju Nagiri, Paul L Burn, and Paul Meredith, Electro-optics of perovskite solar cells, *Nature Photonics*, 9 (2015), 106-112.

- Liu, Qi, Yong Zhou, Zhongping Tian, Xiaoyu Chen, Jun Gao, and Zhigang Zou, Zn₂GeO₄ crystal splitting toward sheaf-like, hyperbranched nanostructures and photocatalytic reduction of CO₂ into CH₄ under visible light after nitridation, *Journal of Materials Chemistry*, 22 (2012), 2033-2038.
- Liu, Wenyong, Qianglu Lin, Hongbo Li, Kaifeng Wu, István Robel, Jeffrey M Pietryga, and Victor I Klimov, Mn²⁺-Doped lead halide perovskite nanocrystals with dual-color emission controlled by halide content, *J. Am. Chem. Soc.*, 138 (2016), 14954-14961.
- Liu, Xiaofeng, Yunhao Cai, Xuebin Huang, Rubo Zhang, and Xiaobo Sun, A perylene diimide electron acceptor with a triptycene core for organic solar cells, *Journal of Materials Chemistry C*, 5 (2017), 3188-3194.
- Liu, Yucheng, Zhou Yang, Dong Cui, Xiaodong Ren, Jiankun Sun, Xiaojing Liu, Jingru Zhang, Qingbo Wei, Haibo Fan, and Fengyang Yu, Two- Inch- Sized Perovskite CH₃NH₃PbX₃ (X= Cl, Br, I) Crystals: Growth and Characterization, *Advanced Materials*, 27 (2015), 5176-5183.
- Ma, Kangzhe, Xiang-Yun Du, Ya-Wen Zhang, and Su Chen, In situ fabrication of halide perovskite nanocrystals embedded in polymer composites via microfluidic spinning microreactors, *Journal of Materials Chemistry C*, 5 (2017), 9398-9404.
- McKittrick, Joanna, and Lauren E Shea- Rohwer, Review: Down Conversion Materials for Solid- State Lighting, *Journal of the American Ceramic Society*, 97 (2014), 1327-1352.
- Meyns, Michaela, Mariano Perálvarez, Amelie Heuer-Jungemann, Wim Hertog, Maria Ibáñez, Raquel Nafria, Aziz Genç, Jordi Arbiol, Maksym V Kovalenko, and Josep Carreras, Polymer-enhanced stability of inorganic perovskite nanocrystals and their application in color conversion LEDs, *ACS Applied Materials & Interfaces*, 8 (2016), 19579-19586.
- Mitzi, DB, *In Progress in Inorganic Chemistry*; Karlin, KD, Ed. John Wiley & Sons: New York.
- MØLLER, CHR KN, Crystal structure and photoconductivity of caesium plumbahalides, *Nature*, 182 (1958), 1436-1436.
- Mosca, Mauro, Fulvio Caruso, Leandro Zambito, Biagio Seminara, Roberto Macaluso, Claudio Calì, and Eric Feltin. 2013. "Warm white LED light by frequency down-conversion of mixed yellow and Red lumogen." *Integrated Photonics: Materials, Devices, and Applications II*.

- Müller, Marcus, Martin Kaiser, Gordon M Stachowski, Ute Resch-Genger, Nikolai Gaponik, and Alexander Eychmüller, Photoluminescence quantum yield and matrix-induced luminescence enhancement of colloidal quantum dots embedded in ionic crystals, *Chemistry of Materials*, 26 (2014), 3231-3237.
- Narendran, N, Y Gu, JP Freyssonier- Nova, and Y Zhu, Extracting phosphor- scattered photons to improve white LED efficiency, *physica status solidi (a)*, 202 (2005), R60-R62.
- Nedelcu, Georgian, Loredana Protesescu, Sergii Yakunin, Maryna I Bodnarchuk, Matthias J Grotevent, and Maksym V Kovalenko, Fast anion-exchange in highly luminescent nanocrystals of cesium lead halide perovskites (CsPbX₃, X= Cl, Br, I), *Nano Letters*, 15 (2015), 5635-5640.
- Noh, Jun Hong, Sang Hyuk Im, Jin Hyuck Heo, Tarak N Mandal, and Sang Il Seok, Chemical management for colorful, efficient, and stable inorganic–organic hybrid nanostructured solar cells, *Nano letters*, 13 (2013), 1764-1769.
- Ogi, Takashi, Asep Bayu Dani Nandiyanto, Kousuke Okino, Ferry Iskandar, Wei-Ning Wang, Eishi Tanabe, and Kikuo Okuyama, Towards better phosphor design: Effect of SiO₂ nanoparticles on photoluminescence enhancement of YAG: Ce, *ECS Journal of Solid State Science and Technology*, 2 (2013), R91-R95.
- Oliva, Jorge, Elder De la Rosa, Luis Diaz- Torres, and Anvar Zakhidov, White light emission from a blue polymer light emitting diode combined with YAG: Ce³⁺ nanoparticles, *physica status solidi (a)*, 211 (2014), 651-655.
- Oner, Ilker, Canan Varlikli, and Siddik Icli, The use of a perylenediimide derivative as a dopant in hole transport layer of an organic light emitting device, *Applied Surface Science*, 257 (2011), 6089-6094.
- Ono, Luis K, Emilio J Juarez-Perez, and Yabing Qi, Progress on Perovskite Materials and Solar Cells with Mixed Cations and Halide Anions, *ACS Applied Materials & Interfaces*, 9 (2017), 30197-30246.
- Otto, Tobias, Marcus Müller, Paul Mundra, Vladimir Lesnyak, Hilmi Volkan Demir, Nikolai Gaponik, and Alexander Eychmüller, Colloidal nanocrystals embedded in macrocrystals: Robustness, photostability, and color purity, *Nano letters*, 12 (2012), 5348-5354.
- Palazon, Francisco, Quinten A Akkerman, Mirko Prato, and Liberato Manna, X-ray lithography on perovskite nanocrystals films: from patterning with anion-

exchange reactions to enhanced stability in air and water, *ACS Nano*, 10 (2015), 1224-1230.

Palazon, Francisco, Francesco Di Stasio, Quinten A Akkerman, Roman Krahné, Mirko Prato, and Liberato Manna, Polymer-free films of inorganic halide perovskite nanocrystals as UV-to-white color-conversion layers in LEDs, *Chemistry of Materials*, 28 (2016), 2902-2906.

Pan, Aizhao, Bo He, Xiaoyun Fan, Zeke Liu, Jeffrey J Urban, A Paul Alivisatos, Ling He, and Yi Liu, Insight into the Ligand-Mediated Synthesis of Colloidal CsPbBr₃ Perovskite Nanocrystals: The Role of Organic Acid, Base, and Cesium Precursors, *ACS Nano*, 10 (2016), 7943-7954.

Pan, Yuexiao, Mingmei Wu, and Qiang Su, Tailored photoluminescence of YAG: Ce phosphor through various methods, *Journal of Physics and Chemistry of Solids*, 65 (2004), 845-850.

Pathak, Sandeep, Nobuya Sakai, Florencia Wisnivesky Rocca Rivarola, Samuel D Stranks, Jiewei Liu, Giles E Eperon, Caterina Ducati, Konrad Wojciechowski, James T Griffiths, and Amir Abbas Haghighirad, Perovskite crystals for tunable white light emission, *Chemistry of Materials*, 27 (2015), 8066-8075.

Pellet, Norman, Peng Gao, Giuliano Gregori, Tae- Youl Yang, Mohammad K Nazeeruddin, Joachim Maier, and Michael Grätzel, Mixed- organic- cation Perovskite photovoltaics for enhanced solar- light harvesting, *Angewandte Chemie International Edition*, 53 (2014), 3151-3157.

Potdevin, Audrey, Geneviève Chadeyron, Sandrine Thérias, and Rachid Mahiou, Luminescent nanocomposites made of finely dispersed Y₃Ga₅O₁₂: Tb powder in a polymer matrix: promising candidates for optical devices, *Langmuir*, 28 (2012), 13526-13535.

Pradhan, Narayan, Samrat Das Adhikari, Sumit K Dutta, Anirban Dutta, and Amit K Guria, Chemically Tailoring the Dopant Emission in Mn doped CsPbCl₃ Perovskite Nanocrystals, *Angewandte Chemie International Edition*, (2017).

Protesescu, Loredana, Sergii Yakunin, Maryna I Bodnarchuk, Federica Bertolotti, Norberto Masciocchi, Antonietta Guagliardi, and Maksym V Kovalenko, Monodisperse formamidinium lead bromide nanocrystals with bright and stable green photoluminescence, *Journal of the American Chemical Society*, 138 (2016), 14202-14205.

Protesescu, Loredana, Sergii Yakunin, Maryna I Bodnarchuk, Franziska Krieg, Riccarda Caputo, Christopher H Hendon, Ruo Xi Yang, Aron Walsh, and

- Maksym V Kovalenko, Nanocrystals of cesium lead halide perovskites (CsPbX₃, X= Cl, Br, and I): novel optoelectronic materials showing bright emission with wide color gamut, *Nano letters*, 15 (2015a), 3692-3696.
- Protesescu, Loredana, Sergii Yakunin, Maryna I Bodnarchuk, Franziska Krieg, Riccarda Caputo, Christopher H Hendon, Ruo Xi Yang, Aron Walsh, and Maksym V Kovalenko, Nanocrystals of cesium lead halide perovskites (CsPbX₃, X= Cl, Br, and I): novel optoelectronic materials showing bright emission with wide color gamut, *Nano Letters*, 15 (2015b), 3692-3696.
- Rimai, DS, and LP DeMejo, Physical interactions affecting the adhesion of dry particles, *Annual Review of Materials Science*, 26 (1996), 21-41.
- Rimai, DS, LP Demejo, J Chen, RC Bowen, and TH Mourey, Time-dependent adhesion-induced phenomena: Viscoelastic creep of a substrate polymer over rigid particles, *The Journal of Adhesion*, 62 (1997), 151-168.
- Rimai, DS, DM Schaefer, RC Bowen, and DJ Quesnel, The time dependence of particle engulfment, *Langmuir*, 18 (2002), 4592-4597.
- Sadhanala, Aditya, Felix Deschler, Tudor H Thomas, Siân E Dutton, Karl C Goedel, Fabian C Hanusch, May L Lai, Ullrich Steiner, Thomas Bein, and Pablo Docampo, Preparation of single-phase films of CH₃NH₃Pb (I_{1-x} Br_x)₃ with sharp optical band edges, *The Journal of Physical Chemistry Letters*, 5 (2014), 2501-2505.
- Saladino, Maria Luisa, Francesco Armetta, Motshabi A Sibeko, Adriaan S Luyt, Delia F Chillura Martino, and Eugenio Caponetti, Preparation and characterisation of Ce: YAG-polycarbonate composites for white LED, *Journal of Alloys and Compounds*, 664 (2016), 726-731.
- Saladino, Maria Luisa, Delia Chillura Martino, Michele A Floriano, Dariusz Hreniak, Lukasz Marciniak, Wiesław Stręk, and Eugenio Caponetti, Ce: Y₃Al₅O₁₂-poly (methyl methacrylate) composite for white-light-emitting diodes, *The Journal of Physical Chemistry C*, 118 (2014), 9107-9113.
- Saladino, Maria Luisa, Antonio Zanotto, Delia Chillura Martino, Alberto Spinella, Giorgio Nasillo, and Eugenio Caponetti, Ce: YAG nanoparticles embedded in a PMMA matrix: preparation and characterization, *Langmuir*, 26 (2010), 13442-13449.
- Saparov, Bayrammurad, and David B Mitzi, Organic-inorganic perovskites: structural versatility for functional materials design, *Chem. Rev*, 116 (2016), 4558-4596.

- Saravanan, Thulasingham, Srinivasan Gokul Raj, Nagamuthu Raja Krishna Chandar, and Ramasamy Jayavel, Synthesis, optical and electrochemical properties of Y₂O₃ nanoparticles prepared by co-precipitation method, *Journal of Nanoscience and Nanotechnology*, 15 (2015), 4353-4357.
- Sayed, Farheen N, V Grover, KA Dubey, V Sudarsan, and AK Tyagi, Solid state white light emitting systems based on CeF₃: RE³⁺ nanoparticles and their composites with polymers, *Journal of Colloid and Interface Science*, 353 (2011), 445-453.
- Schmidt, Luciana C, Antonio Pertegás, Soranyel González-Carrero, Olga Malinkiewicz, Said Agouram, Guillermo Minguez Espallargas, Henk J Bolink, Raquel E Galian, and Julia Pérez-Prieto, Nontemplate synthesis of CH₃NH₃PbBr₃ perovskite nanoparticles, *Journal of the American Chemical Society*, 136 (2014), 850-853.
- Schneider, Caroline A, Wayne S Rasband, and Kevin W Eliceiri, NIH Image to ImageJ: 25 years of image analysis, *Nat methods*, 9 (2012), 671-675.
- Schubert, E Fred, and Jong Kyu Kim, Solid-state light sources getting smart, *Science*, 308 (2005), 1274-1278.
- Schubert, E Fred, Jong Kyu Kim, Hong Luo, and JQ Xi, Solid-state lighting—a benevolent technology, *Reports on Progress in Physics*, 69 (2006), 3069.
- Shamsi, Javad, Zhiya Dang, Paolo Bianchini, Claudio Canale, Francesco Di Stasio, Rosaria Brescia, Mirko Prato, and Liberato Manna, Colloidal synthesis of quantum confined single crystal CsPbBr₃ nanosheets with lateral size control up to the micrometer range, *Journal of the American Chemical Society*, 138 (2016), 7240-7243.
- Shen, Xia, Ding-Fei Zhang, Xiao-Wei Fan, Guang-Shan Hu, Xian-Bin Bian, and Liu Yang, Fabrication and characterization of YAG: Ce phosphor films for white LED applications, *Journal of Materials Science: Materials in Electronics*, 27 (2016), 976-981.
- Sher, Chin-Wei, Chin-Hao Lin, Huang-Yu Lin, Chien-Chung Lin, Che-Hsuan Huang, Kuo-Ju Chen, Jie-Ru Li, Kuan-Yu Wang, Hsien-Hao Tu, and Chien-Chung Fu, A high quality liquid-type quantum dot white light-emitting diode, *Nanoscale*, 8 (2016), 1117-1122.
- Shi, Dong, Valerio Adinolfi, Riccardo Comin, Mingjian Yuan, Erkki Alarousu, Andrei Buin, Yin Chen, Sjoerd Hoogland, Alexander Rothenberger, and Khabiboulakh

- Katsiev, Low trap-state density and long carrier diffusion in organolead trihalide perovskite single crystals, *Science*, 347 (2015), 519-522.
- Shiba, Fumiya, Tosuke Tamagawa, Takashi Kojima, and Yusuke Okawa, Hydrothermal synthesis of one-dimensional yttrium hydroxide particles by a two-step alkali-addition method, *CrystEngComm*, 15 (2013), 1061-1067.
- Shinde, KN, and SJ Dhoble, Europium-activated orthophosphate phosphors for energy-efficient solid-state lighting: a review, *Critical Reviews in Solid State and Materials Sciences*, 39 (2014), 459-479.
- Shirasaki, Yasuhiro, Geoffrey J Supran, Mounqi G Bawendi, and Vladimir Bulović, Emergence of colloidal quantum-dot light-emitting technologies, *Nature Photonics*, 7 (2013), 13-23.
- Shuai, Yun, Nguyen T Tran, Jiun Pyng You, and Frank G Shi. 2012a. "Phosphor size dependence of lumen efficiency and spatial CCT uniformity for typical white LED emitters." 2012 IEEE 62nd Electronic Components and Technology Conference.
- Shuai, Yun, Nguyen T Tran, Jiun Pyng You, and Frank G Shi. 2012b. "Phosphor size dependence of lumen efficiency and spatial CCT uniformity for typical white LED emitters." *Electronic Components and Technology Conference (ECTC)*, 2012 IEEE 62nd.
- Shur, Michael S, and R Zbuzauskas, Solid-state lighting: toward superior illumination, *Proceedings of the IEEE*, 93 (2005), 1691-1703.
- Smet, Philippe F, Anthony B Parmentier, and Dirk Poelman, Selecting conversion phosphors for white light-emitting diodes, *Journal of the Electrochemical Society*, 158 (2011), R37-R54.
- Snaith, Henry J, Perovskites: the emergence of a new era for low-cost, high-efficiency solar cells, *The Journal of Physical Chemistry Letters*, 4 (2013), 3623-3630.
- Sommer, Christian, Frank Reil, Joachim R Krenn, Paul Hartmann, Peter Pachler, Stefan Tasch, and Franz P Wenzl, The impact of inhomogeneities in the phosphor distribution on the device performance of phosphor-converted high-power white LED light sources, *Journal of Lightwave Technology*, 28 (2010), 3226-3232.
- Son, Dae-Yong, Jin-Wook Lee, Yung Ji Choi, In-Hyuk Jang, Seonhee Lee, Pil J Yoo, Hyunjung Shin, Namyong Ahn, Mansoo Choi, and Dongho Kim, Self-formed

grain boundary healing layer for highly efficient CH₃NH₃PbI₃ perovskite solar cells, *Nature Energy*, 1 (2016), 16081.

Song, Jizhong, Jianhai Li, Xiaoming Li, Leimeng Xu, Yuhui Dong, and Haibo Zeng, Quantum Dot Light- Emitting Diodes Based on Inorganic Perovskite Cesium Lead Halides (CsPbX₃), *Advanced Materials*, 27 (2015), 7162-7167.

Song, Young Hyun, Seung Hee Choi, Jin Sun Yoo, Bong Kyun Kang, Eun Kyung Ji, Hyun Suk Jung, and Dae Ho Yoon, Design of long-term stable red-emitting CsPb (Br 0.4, I 0.6) ₃ perovskite quantum dot film for generation of warm white light, *Chemical Engineering Journal*, 313 (2017), 461-465.

Song, Young Hyun, Gill Sang Han, Eun Kyung Ji, Min-Ji Lee, Ye Lim Song, Mong Kwon Jung, Byung Woo Jeong, Hyun Suk Jung, and Dae-Ho Yoon, The novel design of a remote phosphor ceramic plate for white light generation in high power LEDs, *Journal of Materials Chemistry C*, 3 (2015), 6148-6152.

Sotiriou, Georgios A, Melanie Schneider, and Sotiris E Pratsinis, Color-tunable nanophosphors by codoping flame-made Y₂O₃ with Tb and Eu, *The Journal of Physical Chemistry C*, 115 (2010), 1084-1089.

Stoumpos, Constantinos C, and Mercouri G Kanatzidis, The renaissance of halide perovskites and their evolution as emerging semiconductors, *Accounts of Chemical Research*, 48 (2015), 2791-2802.

Stoumpos, Constantinos C, Christos D Malliakas, and Mercouri G Kanatzidis, Semiconducting tin and lead iodide perovskites with organic cations: phase transitions, high mobilities, and near-infrared photoluminescent properties, *Inorganic Chemistry*, 52 (2013), 9019-9038.

Sutherland, Brandon R, and Edward H Sargent, Perovskite photonic sources, *Nature Photonics*, 10 (2016), 295-302.

Swarnkar, Abhishek, Ashley R Marshall, Erin M Sanhira, Boris D Chernomordik, David T Moore, Jeffrey A Christians, Tamoghna Chakrabarti, and Joseph M Luther, Quantum dot-induced phase stabilization of α -CsPbI₃ perovskite for high-efficiency photovoltaics, *Science*, 354 (2016), 92-95.

Tan, ST, XW Sun, HV Demir, and SP DenBaars, Advances in the LED materials and architectures for energy-saving solid-state lighting toward “lighting revolution”, *Photonics Journal, IEEE*, 4 (2012), 613-619.

- Toshima, Takeshi, Hiroyuki Ishikawa, Satoshi Tanda, and Tomohiro Akiyama, Multipod crystals of perovskite SrTiO₃, *Crystal Growth and Design*, 8 (2008), 2066-2069.
- Towata, Atsuya, Manickam Sivakumar, Kyuichi Yasui, Toru Tuziuti, Teruyuki Kozuka, and Yasuo Iida, Synthesis of europium-doped yttrium hydroxide and yttrium oxide nanosheets, *Journal of Materials Science*, 43 (2008), 1214-1219.
- Tran, Nguyen The, Jiun Pyng You, and Frank G Shi, Effect of phosphor particle size on luminous efficacy of phosphor-converted white LED, *Lightwave Technology, Journal of*, 27 (2009a), 5145-5150.
- Tran, Nguyen The, Jiun Pyng You, and Frank G Shi, Effect of phosphor particle size on luminous efficacy of phosphor-converted white LED, *Journal of Lightwave Technology*, 27 (2009b), 5145-5150.
- Tsai, Chun-Chin, Cheng-Feng Yue, Wei-Chih Cheng, Shi-Sheng Hu, Yi-Cheng Hsu, Jyun-Sian Liao, and Wood-Hi Cheng. 2013. "Performance enhancement of high-temperature glass-based phosphor-converted white light-emitting diodes employing SiO₂." *SPIE OPTO*.
- Tsai, Hsinhan, Wanyi Nie, Jean-Christophe Blancon, Constantinos C Stoumpos, Reza Asadpour, Boris Harutyunyan, Amanda J Neukirch, Rafael Verduzco, Jared J Crochet, and Sergei Tretiak, High-efficiency two-dimensional Ruddlesden–Popper perovskite solar cells, *Nature*, 536 (2016), 312-316.
- Tucureanu, Vasilica, Alina Matei, Iuliana Mihalache, Mihai Danila, Marian Popescu, and Bogdan Bitu, Synthesis and characterization of YAG: Ce, Gd and YAG: Ce, Gd/PMMA nanocomposites for optoelectronic applications, *Journal of Materials Science*, 50 (2015), 1883-1890.
- Tunusoğlu, Özge, Rafael Muñoz-Espí, Ümit Akbey, and Mustafa M Demir, Surfactant-assisted formation of organophilic CeO₂ nanoparticles, *Colloids and Surfaces A: Physicochemical and Engineering Aspects*, 395 (2012), 10-17.
- Vos, Willem L, Teus W Tukker, Allard P Mosk, Ad Legendijk, and Wilbert L IJzerman, Broadband mean free path of diffuse light in polydisperse ensembles of scatterers for white light-emitting diode lighting, *Applied Optics*, 52 (2013), 2602-2609.
- Vybornyi, Oleh, Sergii Yakunin, and Maksym V Kovalenko, Polar-solvent-free colloidal synthesis of highly luminescent alkylammonium lead halide perovskite nanocrystals, *Nanoscale*, 8 (2016), 6278-6283.

- Waide, Paul, and Satoshi Tanishima. 2006. *Light's Labour's Lost: Policies for Energy-efficient Lighting*: OECD Publishing.
- Wang, Guofeng, Qing Peng, and Yadong Li, Lanthanide-doped nanocrystals: synthesis, optical-magnetic properties, and applications, *Accounts of Chemical Research*, 44 (2011), 322-332.
- Wang, Hai, Hechun Lin, Xianqing Piao, Pei Tian, Minjie Fang, An Xue'e, Chunhua Luo, Ruijuan Qi, Ye Chen, and Hui Peng, Organometal Halide Perovskite Nanocrystals Embedded in Silicone Resin with Bright Luminescence and Ultrastability, *Journal of Materials Chemistry C*, (2017).
- Wang, Hung- Chia, Shin- Ying Lin, An- Cih Tang, Bheeshma Pratap Singh, Hung- Chun Tong, Ching- Yi Chen, Yu- Chun Lee, Tzong- Liang Tsai, and Ru- Shi Liu, Mesoporous Silica Particles Integrated with All- Inorganic CsPbBr₃ Perovskite Quantum- Dot Nanocomposites (MP- PQDs) with High Stability and Wide Color Gamut Used for Backlight Display, *Angewandte Chemie International Edition*, 55 (2016), 7924-7929.
- Weber, Dieter, CH₃NH₃PbX₃, ein Pb (II)-system mit kubischer perowskitstruktur/CH₃NH₃PbX₃, a Pb (II)-system with cubic perovskite structure, *Zeitschrift für Naturforschung B*, 33 (1978), 1443-1445.
- Wei, Yi, Xiaoran Deng, Zhongxi Xie, Xuechao Cai, Sisi Liang, Ping'an Ma, Zhiyao Hou, Ziyong Cheng, and Jun Lin, Enhancing the Stability of Perovskite Quantum Dots by Encapsulation in Crosslinked Polystyrene Beads via a Swelling–Shrinking Strategy toward Superior Water Resistance, *Advanced Functional Materials*, (2017).
- Wells, Horace Lemuel, Über die Cäsium- und Kalium- Bleihalogenide, *Zeitschrift für anorganische und allgemeine Chemie*, 3 (1893), 195-210.
- Wood, Vanessa, and Vladimir Bulović, Colloidal quantum dot light-emitting devices, *Nano reviews*, 1 (2010), 5202.
- Xia, Zhiguo, Zihan Xu, Mingyue Chen, and Quanlin Liu, Recent developments in the new inorganic solid-state LED phosphors, *Dalton Transactions*, 45 (2016), 11214-11232.
- Xu, Wei, Zhixiong Cai, Feiming Li, Jing Dong, Yiru Wang, Yaqi Jiang, and Xi Chen, Embedding lead halide perovskite quantum dots in carboxybenzene microcrystals improves stability, *Nano Research*, 10 (2017), 2692-2698.

- Yang, Woon Seok, Jun Hong Noh, Nam Joong Jeon, Young Chan Kim, Seungchan Ryu, Jangwon Seo, and Sang Il Seok, High-performance photovoltaic perovskite layers fabricated through intramolecular exchange, *Science*, 348 (2015), 1234-1237.
- Yanli, WU, SUN Weili, ZHOU Xuezheng, JIAO Xiaoyan, DING Jiawen, and LI Yongxiu, Hydrothermal synthesis of Y(OH)₃, Y(OH)₃:Eu³⁺ nanotubes and the photoluminescence of Y(OH)₃:Eu³⁺, Y₂O₃:Eu³⁺, *Journal of Rare Earths*, 27 (2009), 767-772.
- Ye, S, F Xiao, YX Pan, YY Ma, and QY Zhang, Phosphors in phosphor-converted white light-emitting diodes: Recent advances in materials, techniques and properties, *Materials Science and Engineering: R: Reports*, 71 (2010), 1-34.
- Zafer, Ceylan, Canan Karapire, N Serdar Sariciftci, and Siddik Icli, Characterization of N, N'-bis-2-(1-hydroxy-4-methylpentyl)-3, 4, 9, 10-perylene bis (dicarboximide) sensitized nanocrystalline TiO₂ solar cells with polythiophene hole conductors, *Solar Energy Materials and Solar Cells*, 88 (2005), 11-21.
- Zhang, Dandan, Samuel W Eaton, Yi Yu, Letian Dou, and Peidong Yang, Solution-phase synthesis of cesium lead halide perovskite nanowires, *Journal of the American Chemical Society*, 137 (2015), 9230-9233.
- Zhang, Feng, Haizheng Zhong, Cheng Chen, Xian-gang Wu, Xiangmin Hu, Hailong Huang, Junbo Han, Bingsuo Zou, and Yuping Dong, Brightly luminescent and color-tunable colloidal CH₃NH₃PbX₃ (X= Br, I, Cl) quantum dots: potential alternatives for display technology, *ACS Nano*, 9 (2015), 4533-4542.
- Zhang, Jiao, Yanmin Yang, Chao Mi, Yanzhou Liu, Fang Yu, Xiaohong Li, and Yaohua Mai, White up-conversion luminescence power and efficiency in Yb³⁺, Er³⁺- and Tm³⁺-doped BaIn₆Y₂O₁₃, *Dalton Transactions*, 44 (2015), 1093-1101.
- Zhang, Jing, Abu Zayed Mohammad Saliqueer Rahman, Yuxiao Li, Jing Yang, Bozhen Zhao, Eryang Lu, Peng Zhang, Xingzhong Cao, Runsheng Yu, and Baoyi Wang, Synthesis and luminescence properties of Sm-doped LDPE–Na₂SO₄ composite material, *Optical Materials*, 36 (2013), 471-475.
- Zhang, Ning, Xiaohe Liu, Ran Yi, Rongrong Shi, Guanhua Gao, and Guanzhou Qiu, Selective and controlled synthesis of single-crystalline yttrium hydroxide/oxide nanosheets and nanotubes, *The Journal of Physical Chemistry C*, 112 (2008), 17788-17795.

- Zhang, Ya-Wen, Guan Wu, Hui Dang, Kangzhe Ma, and Su Chen, Multicolored Mixed-Organic-Cation Perovskite Quantum Dots (FA x MA_{1-x} PbX₃, X= Br and I) for White Light-Emitting Diodes, *Industrial & Engineering Chemistry Research*, 56 (2017), 10053-10059.
- Zhao, Chengzhou, Xianggui Kong, Xiaomin Liu, Langping Tu, Fei Wu, Youlin Zhang, Kai Liu, Qinghui Zeng, and Hong Zhang, Li⁺ ion doping: an approach for improving the crystallinity and upconversion emissions of NaYF₄: Yb³⁺, Tm³⁺ nanoparticles, *Nanoscale*, 5 (2013), 8084-8089.
- Zhou, Jiangcong, Zhibiao Hu, Lizong Zhang, and Yu Zhu, Perovskite CsPbBr_{1.2}I_{1.8} quantum dot alloying for application in white light-emitting diodes with excellent color rendering index, *Journal of Alloys and Compounds*, 708 (2017), 517-523.
- Zhou, Jiangcong, Feng Huang, Hang Lin, Zebin Lin, Ju Xu, and Yuansheng Wang, Inorganic halide perovskite quantum dot modified YAG-based white LEDs with superior performance, *Journal of Materials Chemistry C*, 4 (2016), 7601-7606.
- Zhou, Yuanyuan, Mengjin Yang, Shuping Pang, Kai Zhu, and Nitin P Padture, Exceptional Morphology-Preserving Evolution of Formamidinium Lead Triiodide Perovskite Thin Films via Organic-Cation Displacement, *Journal of the American Chemical Society*, 138 (2016), 5535-5538.
- Zhu, Jingrun, Xiaoling Yang, Yihua Zhu, Yuanwei Wang, Jin Cai, Jianhua Shen, Luyi Sun, and Chunzhong Li, Room-Temperature Synthesis of Mn-Doped Cesium Lead Halide Quantum Dots with High Mn Substitution Ratio, *The Journal of Physical Chemistry Letters*, 8 (2017), 4167-4171.
- Zhu, Yiting, and Nadarajah Narendran, Investigation of remote-phosphor white light-emitting diodes with multi-phosphor layers, *Japanese Journal of Applied Physics*, 49 (2010), 100203.
- Zumdahl, Steven, and Susan Zumdahl, *Chemistry*, 9th AP Edition, Belmont, CA: Brooks/Cole, 374.

APPENDIX A

PYTHON CODES OF THE SIMULATION

Main Code

```
from math import *
import matplotlib.pyplot as plt
from pylab import *
import random as rd
from simullfonk1 import fonk1
from simullfonk2 import fonk2
Itamplitude=884      #transmission peak intensity
Ieamplitude=373     #yellow emission peak intensity
Iramplitude=355     #red emission peak intensity
lambdatrans=478     #transmission peak intensity wavelength
lambdaemisy=550     #yellow emission peak intensity wavelength
lambdaemisr=620     #red emission peak intensity wavelength
lambdarange=range(400,750) #spectrum range
FWHMT=30            #transmission FWHM
FWHME=129           #yellow emission FWHM
FWHMR=82            ##red emission FWHM
toplamsnucstack=0
toplamsnucmixt=0
dalgaboyu=[]
boyut=0
specintensityst=[]
specintensitymx=[]
mcarlorange=range(0,3000) #monte carlo process time
ortalama=[]
for lambdad in lambdarange:
    for ray in mcarlorange:
        tey=Itamplitude*exp(-4*log(2)*((lambdad-
lambdatrans)**2)/(FWHMT**2))+Ieamplitude*exp(-
4*log(2)*((lambdad-lambdaemisy)**2)/(FWHME**2))
        ter=Itamplitude*exp(-4*log(2)*((lambdad-
lambdatrans)**2)/(FWHMT**2))+Iramplitude*exp(-
4*log(2)*((lambdad-lambdaemisr)**2)/(FWHMR**2))
        bey=Itamplitude*100*exp(-4*log(2)*((lambdad-
lambdatrans)**2)/(FWHMT**2))/tey
```



```

ber=Itamplitude*100*exp(-4*log(2)*((lambdad-
lambdatrans)**2)/(FWHMT**2))/ter
yep=Ieamplitude*100*exp(-4*log(2)*((lambdad-
lambdaemisy)**2)/(FWHME**2))/tey
rep=Irampplitude*100*exp(-4*log(2)*((lambdad-
lambdaemisr)**2)/(FWHMR**2))/ter
deger=fonk1(lambdad,tey,ter,bey,ber,yep,rep) #stacking
function
deger2=fonk2(lambdad,tey,ter,bey,ber,yep,rep) #mixture
function
toplamsnucstack=toplamsnucstack+deger
toplamsnucmixt=toplamsnucmixt+deger2
boyut=boyut+1
ortalamadegerst=toplamsnucstack/boyut
ortalamadegermx=toplamsnucmixt/boyut
specintensityst.append(ortalamadegerst)
specintensitymx.append(ortalamadegermx)
dalgaboyu.append(lambdad)
toplamsnucstack=0
toplamsnucmixt=0
boyut=0
plt.plot(dalgaboyu,specintensityst,'-
bo',dalgaboyu,specintensitymx,'-r*')
plt.show()

```

Stacking Function

```

from math import *
import random as rd
def
fonk1(lambdad,totaleventyel,totaleventred,bluemisspyel,bluemissp
red,yellowemissp,redemissp):
    Itamplitude=884
    Ieamplitude=373
    Irampitude=355
    lambdatrans=478
    lambdaemisy=550
    lambdaemisr=620
    FWHMT=30
    FWHME=129
    FWHMR=82
    kirmiziolas=rd.randint(0,100)
    if kirmiziolas<=27: #27% probability condition for red phosphor
interaction
        yuvar1=floor(100)
        redolasilik=rd.randint(0,yuvar1)
        if bluemisspred<redemissp:

```

```

if redolasilik<redemissp:
    intensityred=Iramplitude*exp(-4*log(2)*((lambdad-
lambdaemisr)**2)/(FWHMr**2))
    return intensityred
if redolasilik>=redemissp:
    yuvar2=floor(100)
    yelolasilik=rd.randint(0,yuvar2)
    if bluemispyel<yellowemissp:
        if yelolasilik<yellowemissp:
            intensity2=Ieamplitude*exp(-4*log(2)*((lambdad-
lambdaemisy)**2)/(FWHMe**2))
            return intensity2
        if yelolasilik>=yellowemissp:
            intensity3=Itamplitude*exp(-4*log(2)*((lambdad-
lambdatrans)**2)/(FWHMt**2))
            return intensity3
    if bluemispyel>=yellowemissp:
        if yelolasilik<bluemispyel:
            intensity4=Itamplitude*exp(-4*log(2)*((lambdad-
lambdatrans)**2)/(FWHMt**2))
            return intensity4
        if yelolasilik>=bluemispyel:
            intensity5=Ieamplitude*exp(-4*log(2)*((lambdad-
lambdaemisy)**2)/(FWHMe**2))
            return intensity5
if redemissp<=bluemisspred:
    if redolasilik<bluemisspred:
        yuvar3=floor(100)
        yelolasilik2=rd.randint(0,yuvar3)
        if bluemispyel<yellowemissp:
            if yelolasilik2<yellowemissp:
                intensity6=Ieamplitude*exp(-4*log(2)*((lambdad-
lambdaemisy)**2)/(FWHMe**2))
                return intensity6
            if yelolasilik2>=yellowemissp:
                intensity7=Itamplitude*exp(-4*log(2)*((lambdad-
lambdatrans)**2)/(FWHMt**2))
                return intensity7
        if bluemispyel>=yellowemissp:
            if yelolasilik2<bluemispyel:
                intensity8=Itamplitude*exp(-4*log(2)*((lambdad-
lambdatrans)**2)/(FWHMt**2))
                return intensity8
            if yelolasilik2>bluemispyel:
                intensity9=Ieamplitude*exp(-4*log(2)*((lambdad-
lambdaemisy)**2)/(FWHMe**2))
                return intensity9
    if redolasilik>=bluemisspred:

```

```

        intensityred2=Iramplitude*exp(-4*log(2)*((lambdad-
lambdaemisr)**2)/(FWHMr**2))
        return intensityred2
    if kirmiziolas>27:
        yuvar4=floor(100)
        yelolasilik3=rd.randint(0,yuvar4)
        if bluemispyel<yellowemissp:
            if yelolasilik3<yellowemissp:
                intensity10=Ieamplitude*exp(-4*log(2)*((lambdad-
lambdaemisy)**2)/(FWHMe**2))
                return intensity10
            if yelolasilik3>=yellowemissp:
                intensity11=Itamplitude*exp(-4*log(2)*((lambdad-
lambdatrans)**2)/(FWHMt**2))
                return intensity11
            if bluemispyel>=yellowemissp:
                if yelolasilik3<bluemispyel:
                    intensity12=Itamplitude*exp(-4*log(2)*((lambdad-
lambdatrans)**2)/(FWHMt**2))
                    return intensity12
                if yelolasilik3>=bluemispyel:
                    intensity13=Ieamplitude*exp(-4*log(2)*((lambdad-
lambdaemisy)**2)/(FWHMe**2))
                    return intensity13

```

Mixture Function

```

from math import *
import random as rd
def
fonk2(lambdad,totaleventyel,totaleventred,bluemispyel,bluemispp
red,yellowemissp,redemissp):
    Iamplitude=884
    Ieamplitude=373
    Iramplitude=355
    lambdatrans=478
    lambdaemisy=550
    lambdaemisr=620
    FWHMt=30
    FWHMe=129
    FWHMr=82
    interactionprob=rd.randint(0,100)
    if interactionprob<=40: #Empty space condition embedded as
probability
        intensity1=Itamplitude*exp(-4*log(2)*((lambdad-
lambdatrans)**2)/(FWHMt**2))
        return intensity1

```

```

if interactionprob>40:
    interactionprob2=rd.randint(0,100)
    if interactionprob2<=22:
        redolasilik=rd.randint(0,100)
        if bluemissspred<redemissp:
            if redolasilik<redemissp:
                intensityred=Iramplitude*exp(-4*log(2)*((lambdad-
lambdaemisr)**2)/(FWHMr**2))
                return intensityred
            if redolasilik>=redemissp:
                intensity2=Itamplitude*exp(-4*log(2)*((lambdad-
lambdatrans)**2)/(FWHMt**2))
                return intensity2
        if bluemissspred>=redemissp:
            if redolasilik<bluemissspred:
                intensity3=Itamplitude*exp(-4*log(2)*((lambdad-
lambdatrans)**2)/(FWHMt**2))
                return intensity3
            if redolasilik>=bluemissspred:
                intensityred2=Iramplitude*exp(-4*log(2)*((lambdad-
lambdaemisr)**2)/(FWHMr**2))
                return intensityred2
    if interactionprob2>22:
        yelolasilik=rd.randint(0,100)
        if bluemissspyel<yellowemissp:
            if yelolasilik<yellowemissp:
                intensityyellow=Ieamplitude*exp(-4*log(2)*((lambdad-
lambdaemisy)**2)/(FWHMe**2))
                return intensityyellow
            if yelolasilik>=yellowemissp:
                intensity4=Itamplitude*exp(-4*log(2)*((lambdad-
lambdatrans)**2)/(FWHMt**2))
                return intensity4
        if yellowemissp<bluemissspyel:
            if yelolasilik<bluemissspyel:
                intensity5=Itamplitude*exp(-4*log(2)*((lambdad-
lambdatrans)**2)/(FWHMt**2))
                return intensity5
            if yelolasilik>=bluemissspyel:
                intensityyellow2=Ieamplitude*exp(-4*log(2)*((lambdad-
lambdaemisy)**2)/(FWHMe**2))
                return intensityyellow2

```

VITA

PERSONAL INFORMATION

Surname, Name: Güner Tuğrul
Nationality: Turkish (TC)
Date and Place of Birth: 30.03.1988, Aliğa/İzmir
E-mail: tugrulgunr@gmail.com



EDUCATION

Degree, Institution, Year of Graduation
MSc, Izmir Institute of Technology, 2015
BSc, Bilkent University, 2011

WORK EXPERIENCE

Year, Place, Enrollment
2017-2018, Izmir Institute of Technology, Research Assistant

AWARDS

Gold Medal Certificate in recognition of excellent and creative efforts to invent White LED Package with Phosphor Placement, 3rd Istanbul International Inventions Fair, ISIF18.

PUBLICATIONS

11. Guner, T., Aksoy, E., Varlikli, C., and Demir, M. M. (2019). Dyes and Pigments, 160, 501.
10. Guner, T., Akbali, B., Ozcan, M., Topcu, G., Demir, M. M., and Sahin, H. (2018). The Journal of Physical Chemistry C, 122, 11543.
9. Guner, T., Demir, M. M. (2018). Physica Status Solidi A: Applications and Materials Science, 215, 1800120.
8. Akbali, B., Topcu, G., Guner, T., Ozcan, M., Demir, M. M., Sahin, H. (2018). Physical Review Materials, 2, 034601.
7. Guner, T., Topcu, G., Savaci, U., Genc, A., Turan, S., Sari, E., Demir, M. M. (2018). Nanotechnology, 29, 135202.
6. Topcu, G., Guner, T., Demir, M.M. (2018). Photonics and Nanostructures - Fundamentals and Applications, 29, 22-29.
5. Emrullahoglu, M., Sayar, M., Karakus, E., Guner, T., Yildiz, B., & Yildiz, U. H. (2018). Chemistry: A European Journal, 24, 3136.
4. Demir, D. A., Guner, T. (2017). Annals of Physics, 386, 291.
3. Guner, T., Senturk, U., & Demir, M. M. (2017). Optical Materials, 72, 769-774.
2. Guner, T., Koseoglu, D., & Demir, M. M. (2016). Optical Materials, 60, 422-430.
1. Incel, A., Guner, T., Parlak, O., & Demir, M. M. (2015). ACS applied materials & interfaces, 7(49), 27539-27546.